ABSTRACT

Title of Document: MICROSCALE HEAT TRANSFER MEASUREMENTS DURING SUBCOOLED POOL BOILING OF PENTANE: EFFECT OF FLUID PROPERTIES AND BUBBLE DYNAMICS

Payam Delgoshaei, Ph.D., 2009

Directed By: Professor, Jungho Kim, Department of Mechanical Engineering

Pool boiling heat transfer measurements were made in earth gravity using a 2.7 × 2.7 mm^2 microheater array during subcooled pool boiling of pentane. The microheater array consists of 96 independent heater elements that were maintained at an isothermal boundary condition using control circuitry. Experiments were made to investigate the dominant heat transfer mechanisms and to study the effect of fluid properties and bubble dynamics.

The semitransparent nature of the heater allowed the high speed images of the bubbles, and thus the bubble contact area, to be taken from underneath. The contact area movement on the heater was then correlated to heat transfer variation on the heater and provided a basis to investigate heat transfer mechanisms (e.g. microlayer evaporation and transient conduction).

Heat transfer related to single bubbles was studied primarily. Boiling at atmospheric pressure resulted in short and moderate bubble growth times. Boiling at higher pressures (1.34 atm and 1.5 atm) generally resulted in larger bubble growth times.

Single phase heat transfer mechanisms (transient conduction and/or microconvection) were found to be dominant for bubbles with shorter growth time; two phase heat transfer mechanisms (contact line evaporation and/or microlayer evaporation) were found to be dominant heat transfer mechanisms for bubbles with longer growth time.

The proposed hypothesis is that when the bubble grows rapidly, the majority of the required heat for bubble growth originates from the superheated liquid layer and not from instantaneous heat from the wall. For bubbles that grow more slowly, however, the bubble growth is limited by the wall heat transfer--the energy stored in the superheated liquid layer has been depleted (perhaps by previously departing bubbles) leaving the wall as the only source of energy. This energy must be transferred through the microlayer evaporation or contact line heat transfer.

Finally, the heat transfer characteristics related to a more complicated case i.e. lateral merger of two bubbles on the heater was investigated. The heat transfer variation was found to be closely related to the change in the contact area and the contact line movement on the heater.

MICROSCALE HEAT TRANSFER MEASUREMENTS DURING SUBCOOLED POOL BOILING OF PENTANE: EFFECT OF FLUID PROPERTIES AND BUBBLE DYNAMICS

By

Payam Delgoshaei

Dissertation submitted to the Faculty of the Graduate School of the
University of Maryland, College Park, in partial fulfillment
of the requirements for the degree of
Doctor of Philosophy
2009

Advisory Committee:
Professor Jungho Kim, Chair
Professor Avram Bar-Cohen
Professor James Duncan
Associate Professor Kenneth Kiger
Associate Professor Gary Pertmer

To my sister, Parastoo

Acknowledgements

First and foremost, I would like to acknowledge my advisor, Professor Jungho Kim, for all his invaluable support and guidance in this work. Without his helpful suggestions, I would not have been able to finish this work. This work is built on the solid foundation created by Dr. Kim and previous researchers including Fatih Demiray. I also appreciate the guidance of my advisory committee: Dr. Avram Bar-Cohen, Dr. James Duncan, Dr. Kenneth Kiger, and Dr. Gary Pertmer. I would like to specially acknowledge Dr. Bar-Cohen for all his guidance.

I have been very fortunate to work side by side with a number of distinguished former and current students of the Phase Change Heat Transfer Laboratory (Chris Henry, Jack Coursey, Greg Anderson, Kevin Moores, Rishi Raj, Bahman Abbasi, Michael Siemann, Thierry Some, Steven Fuqua, Eckhard Lehmann, and Alexander Walzenbach) who are wonderful friends and invaluable colleagues. I also appreciate all the invaluable training that I received from my former colleague, Dr. Hitoshi Sakamato, during the early stages of this work. I would like to specially acknowledge Rishi, Michael, Bahman, and Greg for their suggestions regarding the writing of my thesis.

I would have not been in the position to finish this dissertation without the support of my family. I am forever grateful to my parents, brother and sister for all their support and encouragement. I also appreciate all the sacrifices that my sister made such as preparing my lunch and washing my dishes so that I can focus on my dissertation.

TABLE OF CONTENTS

LIST OF FIGURES

LIST OF TABLES

Nomenclature

A_h	area of heater
A_{pixel}	area of pixel
C_2	constant in $\delta_0 = C_2\sqrt{\nu t_g}$
c_p	specific heat
d	bubble diameter
g	gravitational acceleration
h_{lv}	heat of vaporization
k	thermal conductivity
L_b	capillary length
ME	microlayer evaporation heat transfer
P	pressure
P_r	reduced pressure (p/p_c)
$\dot{q}$	power
$\dot{q}''$	heat flux
$\dot{q}_{baseline}$	baseline heat transfer
$\dot{q}_{bubble}$	bubble heat transfer
$\dot{q}_{raw}$	raw heat transfer
$\dot{q}_{raw,i}$	i th heater raw heat transfer
T_{bulk}	bulk temperature
T_l	liquid temperature in the model
T_w	wall temperature
T_{sat}	saturation temperature

TC	transient conduction heat transfer
R_{th}	thermal resistance
R_i	i th heater resistance
$R_{ref,i}$	reference heater resistance at reference temperature
r	bubble radius
t	time
t_g	growth time
$u_{R_{ref,i}}$	reference heater resistance uncertainty
u_α	temperature coefficient of resistance uncertainty
$u_{\Delta T}$	temperature difference uncertainty
u_{V_i}	voltage uncertainty
u_{R_i}	resistance uncertainty
$u_{\dot{q}_{raw,i}}$	raw heat transfer uncertainty
V	volume
$x_{L,1}$	liquid mole fraction of the more volatile component
x	x direction
y	y direction
z	z direction

Greek symbols

α	temperature coefficient of resistance
α_l	thermal diffusivity

δ_0	initial thickness of microlayer
δ	microlayer thickness
ρ	density
σ	surface tension
θ	contact angle
ν	kinematic viscosity of liquid

Subscripts

eq	equivalent
h	heater
in	inner
l	liquid
me	microlayer evaporation
out	outer
sat	saturation
tc	transient conduction
v	vapor

CHAPTER 1: INTRODUCTION

1.1. Motivation

Boiling has been used in variety of applications ranging from large-scale heat transfer equipment to small-scale heat sinks. Some of the applications that take advantage of boiling heat transfer include: Power cycles, refrigeration cycles, and metallurgical quenching.

Thermal resistance, defined in Eq. 1.1, is one of the key parameters in a thermal design. High heat removal rates during boiling occur over relatively low temperature differences; this results in low thermal resistances.

$$R_{th} = \frac{\Delta T}{\dot{q}} \qquad (1.1)$$

Thermal resistance for boiling is compared with thermal resistance associated with natural and forced convection in Fig 1.1.

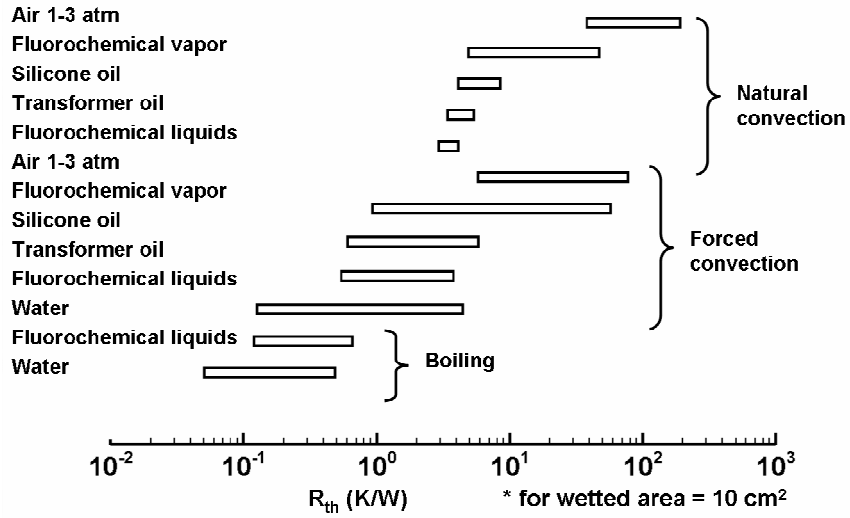

Figure 1.1. Thermal resistance comparison (Courtesy of Avram Bar-Cohen).

Low thermal resistances associated with boiling can become very useful in the thermal management of high performance electronics. With decreasing package size, heat generation from high performance electronic devices results in heat fluxes on the order of 100 W/cm^2. The operating temperature for these devices should not generally exceed a desired value (typically, 85 °C); boiling heat transfer can mitigate some of the resulting challenges.

1.2. Background

Boiling at the surface of a heated body immersed in an extensive pool of liquid without bulk motion is generally referred to as pool boiling. The regimes of pool boiling can be easily shown on a so-called boiling curve: A plot of wall heat flux $\dot{q}''$ versus wall superheat $T_w - T_{sat}$. Boiling curve for a wetting liquid will be similar to that shown in Fig. 1.2 providing the following conditions are satisfied:

- The surface temperature of the heated wall is independently controlled and slowly increased.
- The dimensions of the body are large compared to bubble or capillary length scale L_b defined as

$$L_b = \sqrt{\frac{\sigma}{g(\rho_l - \rho_v)}} \tag{1.1}$$

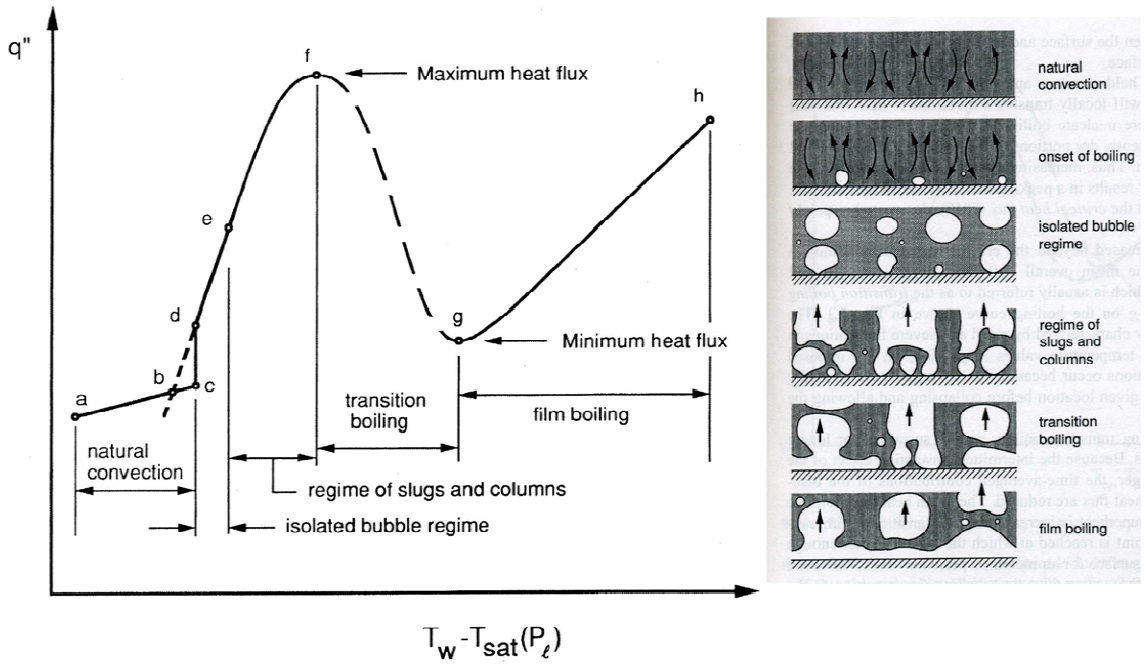

Figure 1.2. Typical boiling curve and associated boiling regimes.
(Courtesy of Van Carey, 2008)

As shown in Fig. 1.2, the boiling curve can generally be divided into five regimes: 1) natural convection regime, 2) isolated bubble regime, 3) regime of slugs and columns, 4) transition boiling regime, and 5) film boiling regime. A brief summary of the characteristics of each regime are provided here. The reader is referred to Carey, 2008 for a more detailed discussion.

At low superheats natural convection is the dominant heat transfer mechanism. The onset of nucleate boiling occurs at point c in Fig. 1.1. The surface heat flux suddenly increases (from c to d) as a result of this added heat transfer. The next section of the boiling curve consists of the nucleate boiling regime (d-f). The nucleate boiling regime is comprised of two regimes: 1) isolated bubble regime, and 2) regime of slugs and columns. The active nucleation sites are few and widely spaced for the isolated bubble

regime (d-e). As the wall superheat increases, more and more nucleation sites become active and the bubble departure frequency generally increases.

With increasing wall superheat, the nucleation sites are spaced so closely and departure frequency is high enough that bubbles merge in the lateral and vertical direction. This segment of the curve (e-f) is referred to as the regime of slugs and columns. In this regime, the flow rate of the vapor away from the surface increases with an increase in the wall superheat resulting in higher surface heat fluxes.

Eventually, the drag on the liquid rewetting the surface becomes so severe that the liquid is unable to completely rewet the surface (formation of dry portions on the surface). The local heat flux at the dry portions is significantly lower than the wetted portions. This results in a peak value for the heat flux known as critical heat flux (CHF).

The next regime in the boiling curve (f-g) corresponds to the transition boiling in which the mean overall surface heat flux decreases with the wall superheat. This region is typically characterized by severe and rapid fluctuations of the surface heat flux (for a constant surface temperature boundary condition) which results from the rewetting of the surface at a given location after the collapse of dry spots. Eventually, the wall superheat becomes high enough to maintain a stable vapor film that blankets the entire surface. This transition occurs in point g in the boiling curve.

Film boiling regime (g-h) is the final regime in the boiling curve. The heat flux monotonically increases as the wall superheat increases. This trend is a consequence of the increased temperature difference across the vapor film $[T_w - T_{sat}(P_l)]$ which results in higher conduction and/or convection heat transfer. Radiation heat transfer may also become important at higher wall superheats.

The importance of nucleate boiling in many heat transfer applications has provided the incentive for numerous studies of the basic heat transfer mechanisms. Natural or machine-formed pits or any other surface imperfections can trap within themselves some amount of gas/vapor. Hsu (1962) postulated that the bubble nucleates when the superheated liquid layer above the site grows sufficiently thick to cause the vapor/gas trapped within the cavity to overcome the surface tension force. The steady cyclic growth and release of vapor bubbles from a nucleation site is usually termed the ebullition cycle.

The available heat transfer mechanisms by which heat can be transferred from a heated surface are schematically shown in Fig. 1.3 and Fig 1.4 for bubble growth and departure. A brief discussion on each of the mechanisms is provided in this chapter; detailed discussion is provided in the Literature Review chapter.

Figure 1.3 depicts the available heat transfer mechanisms during bubble growth. A rapidly growing bubble can trap beneath itself a thin layer of liquid known as microlayer; the evaporation of this liquid layer can contribute to the bubble's growth. The energy required for this evaporation comes from the energy stored in the superheated wall. The bubble can also grow through evaporation of the superheated liquid layer surrounding the bubble. A three-phase contact line can form on the surface in the event of formation of a dry patch and partial dryout of the microlayer. Bubble growth can also take place through the evaporation at three-phase contact line. The natural convection heat transfer can also be enhanced as a result of liquid motion induced by bubble growth resulting in energy transfer by microconvection.

The available heat transfer mechanisms during bubble departure are depicted in Fig. 1.4. During bubble departure, transient conduction occurs as the dry patch is being rewetted by the advancing liquid front. Microlayer evaporation can still contribute to the total heat transfer providing the liquid layer has not completely dried out. Evaporation from the superheated liquid layer can also take place. Contact line evaporation could also be present but its contribution is expected to be smaller since the advancing contact angle is steeper than the receding contact angle. The departing bubble can also perturb the adjacent liquid resulting in heat transfer due to microconvection. Additional heat transfer could occur as a result of the vortices in the wake of the bubble.

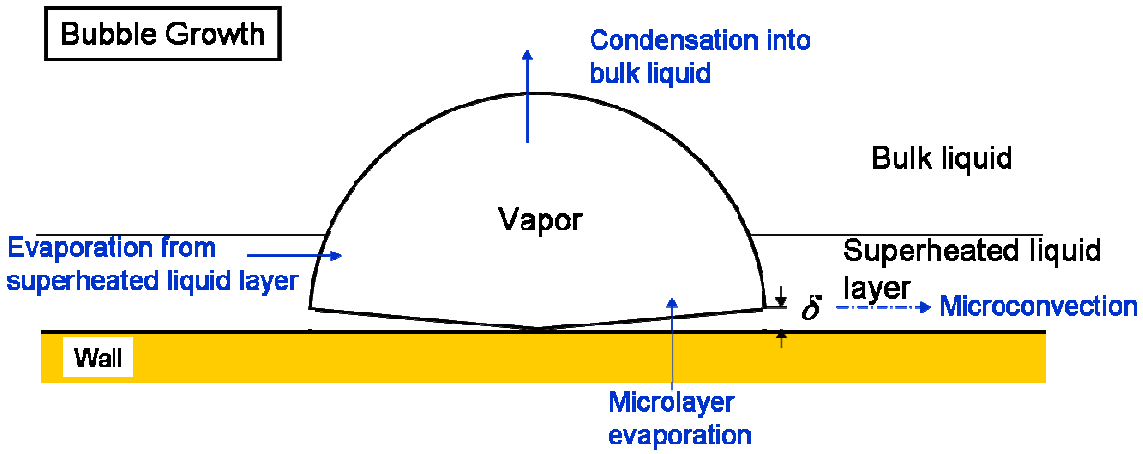

Figure 1.3. Heat transfer mechanisms during bubble growth.

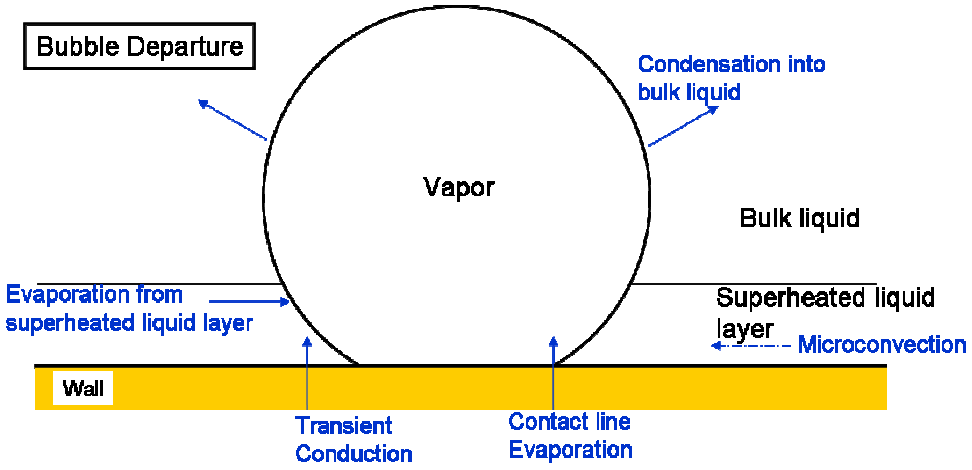

Figure 1.4. Heat transfer mechanisms during bubble departure.

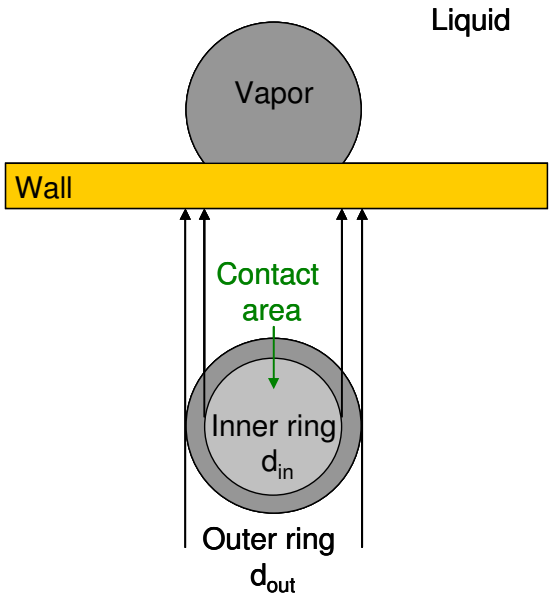

Figure 1.5. Bubble footprint on the heater.

It should be noted that the condition of the bubble footprint (Fig. 1.5) could greatly affect the wall heat transfer. There are three possibilities for the bubble footprint (contact area):

1) The microlayer entirely covers the area.

2) The microlayer partially covers the area.

3) Vapor completely covers the area (dryout).

This thesis investigates the heat transfer characteristics associated with the above cases.

The ratio of sensible heat to latent heat for a fluid is one of the key parameters that could affect the contribution of heat transfer mechanisms in nucleate boiling. This ratio can be quantified by the Jakob number given by (Eq. 1.1):

$$Ja = \frac{\rho_l c_{pl} (T_w - T_{sat})}{\rho_v h_{lv}} \tag{1.1}$$

The value of the Jakob number and the contribution of transient conduction and/or micro convection are directly related. The contribution of single phase heat transfer mechanisms is expected to be lower for lower valued Jakob numbers.

1.3. Research Objectives

Many researchers have developed models to predict the heat transfer rates for many combinations of heated surfaces and working fluids. The main factors that affect such predictions are:

1) The number of active nucleation sites.

2) The bubble dynamics associated with each nucleation site.

3) The heat transfer contribution of individual bubbles.

4) The heat transfer associated with the interaction of multiple bubbles.

This thesis primarily explores the last three factors mentioned above and is designed to shed light on some of the underlying heat transfer mechanisms.

CHAPTER 2: LITERATURE REVIEW

A complete review of the boiling literature is beyond the scope of this thesis. An effort was made to review the most relevant literature to the current work. Both experimental and numerical works were considered. This chapter is divided into two sections: Section 2.1 reviews the literature regarding heat transfer due to single bubbles. Section 2.2 reviews the literature regarding heat transfer due to the merging of two or more bubbles.

2.1. Single Bubble Heat Transfer

Heat transfer characteristics during pool boiling have been studied extensively for more than 50 years. Many mechanisms for bubble heat transfer have been suggested (Carey, 2008) but the most widely cited mechanisms consist of: microlayer evaporation, contact line evaporation, transient conduction and microconvection. Many models, for the simplest case of single bubbles (where bubble interactions are not present), have been proposed based on the above mechanisms. These models can be divided into two categories: (1) models that consider only one of the mechanisms to be dominant, and (2) models where a combination of mechanisms contribute to the total heat transfer (composite models). A review of some of the studies that proposed the above mentioned models follows.

The experimental results of Cooper and Lloyd (1969) supported the hypothesis that a thin layer of liquid (the microlayer) forms beneath a vapor bubble. They also

provided an expression for the thickness of the microlayer. The results of their study were for two different organic working fluids (toluene and isopropyl alcohol) and the only heat transfer mechanism considered was microlayer evaporation. Mikic and Rohsenow (1969) proposed the transient conduction to be the dominant heat transfer mechanism. They assumed that a departing bubble pumps away the hot liquid adjacent to the heated surface from an area twice the bubble diameter. Bubble induced convection (microconvection) was first introduced by Rohsenow (1952). Judd and Hwang (1976) proposed a three component composite model that consisted of microlayer evaporation, transient conduction, and natural convection.

The merits of each of the proposed heat transfer models remain a topic of debate in the literature. Many earlier experimental studies used a single heating element operated at constant heat flux boundary condition, making it difficult to obtain local temperature variation on the surface; other experiments utilized constant surface boundary condition but the local heat flux measurements were not available. The proposed heat transfer models can be evaluated through recent experimental and numerical studies in which local heat transfer data is available. The studies pertaining to single bubble heat transfer is reviewed in the remainder of this section.

2.1.1. Recent Experiments

A summary of recent experimental investigations pertaining to single bubble heat transfer in which local heat transfer measurements during the ebullition cycle were obtained is a follows.

2.1.1.1. Microheater Array Data

Yaddanapuddi and Kim (2001) used a microheater array consisting of 96 independently controlled heaters each nominally 0.27×0.27 mm^2 in size to measure the heat transfer distribution under isolated bubbles during saturated pool boiling of FC-72. The heaters were kept at constant temperature through the use of analog electronic feedback circuits and the power required to do this was measured. More details regarding this microheater array are provided in Chapter 3. The bubble departure diameter was 370 μm (larger than a single heater). Their results indicated that bubble growth occurred primarily due to energy gained from the superheated liquid layer.

Demiray and Kim (2004) performed similar measurements using a microheater array with 100 μm heaters (improvement in spatial resolution) during subcooled pool boiling of FC-72. The test conditions for their work along with the calculated Jakob number are provided in Table 2.1.

Table 2.1. Test conditions associated with Fig. 2.1.

Fluid	FC-72
Pressure (atm)	1
T_w(°C)	76
T_{sat} (°C)	57
T_{bulk} (°C)	52
Superheat (°C)	19
Subcooling (°C)	5
Jakob Number	31.3

They used the instantaneous wall heat transfer data to calculate an equivalent bubble diameter assuming that all the heat transferred from the wall appears as latent heat:

$$\rho_v \frac{\pi d_{eq}^3(t)}{6} h_{lv} = \int_0^t \dot{q}_h''(t) A_h dt \tag{2.1}$$

where t=0 is assumed to be the nucleation time for a single bubble.

Bubble physical diameter is significantly larger than the calculated equivalent diameter during the bubble growth time (Fig. 2.1), indicating that heat transfer from the wall alone can not account for bubble growth. They concluded that the bubble growth was primarily due to energy transfer from the superheated liquid layer; therefore transient conduction and/or microconvection were the dominant heat transfer mechanisms.

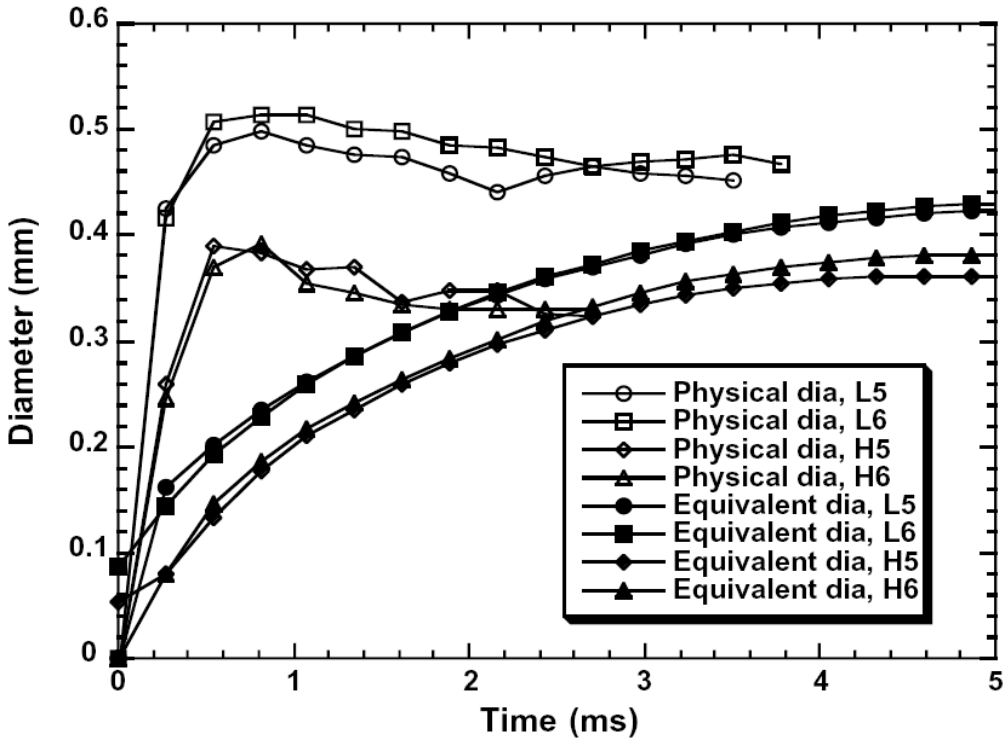

Figure 2.1. Comparison of the physical and equivalent bubble diameter. From Demiray and Kim (2004).

Myers et al. (2005) used a microheater array (100 μm heater size) operated in constant heat flux boundary condition to study the effect of thermal boundary condition on the heat transfer mechanisms during pool boiling of FC-72. Wall temperature distributions were measured throughout the bubble nucleation and departure cycle and the wall-to-fluid heat transfer was obtained by numerically computing the heat lost to the

substrate and subtracting this from the input heat. They concluded that microlayer and contact line evaporation are not major heat transfer mechanisms for bubble growth (for the conditions studied). Transient conduction into the liquid as the liquid rewets the wall during the bubble departure is the dominant heat transfer mechanism.

Lee et al. (2003a) used a microheater array to maintain a constant temperature boundary condition to study saturated boiling of R11. They obtained the geometry of the bubble from side view images and assumed the changes in bubble shape were due to latent heat (Eq. 2.2).

$$\dot{q} = \dot{m}h_{lv} = \rho_v \dot{V} h_{lv} \tag{2.2}$$

where V is the bubble volume and assumed to be a truncated sphere.

A comparison of measured instantaneous wall heat transfer and the required heat for bubble growth (Eq. 2.2) is given in Fig. 2.2. They concluded that measured instantaneous wall heat transfer was not sufficient for bubble growth.

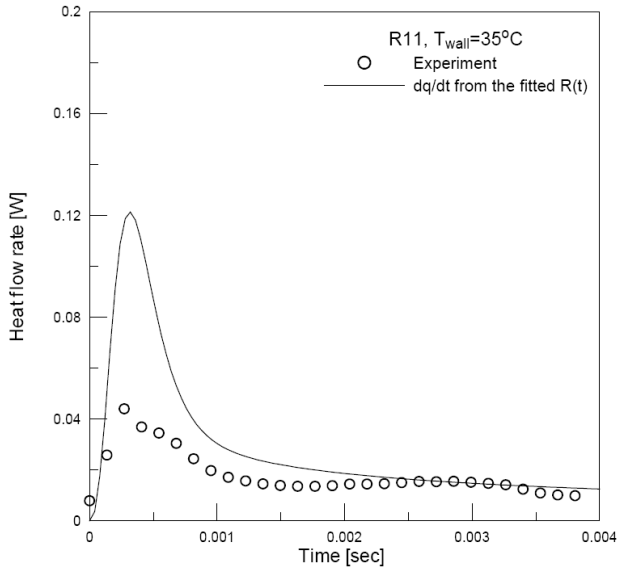

Figure 2.2. Comparison of measured (experiment) and required (fitted) heat transfer. From Lee et al. (2003 a).

In a similar study, Lee et al. (2003 b) investigated the saturated pool boiling of R11 and R113 using a microheater array operated in constant temperature mode. Bubbles assumed to be axi-symmetric about the vertical axis but non-symmetric about the horizontal axis (Fig. 2.3). The equivalent physical bubble radius was calculated from Eq. 2.3.

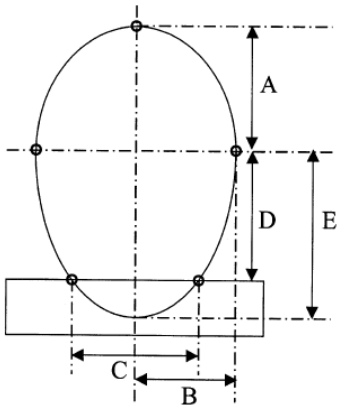

Figure 2.3. Geometry of the spheroid used to determine the bubble volume.

$$R_{eq} = \left(\frac{1}{2} B^2 A + \frac{3}{4} B^2 \left[D - \frac{D^3}{3E^2} \right] \right)^{\frac{1}{3}} \tag{2.3}$$

The required heat from the bubble growth was similarly calculated from Eq. 2.4.

$$\dot{q} = \dot{m} h_{lv} = \rho_v \dot{V} h_{lv} = 4\pi \rho_v h_{lv} R^2 \frac{dR}{dt} \tag{2.4}$$

where R is the equivalent bubble radius.

The ratio of the measured heat from the wall to the required heat is plotted as a function time for R11 in Fig. 2.4. They concluded that the contribution of the instantaneous heat is about 50% of the required heat for bubble growth.

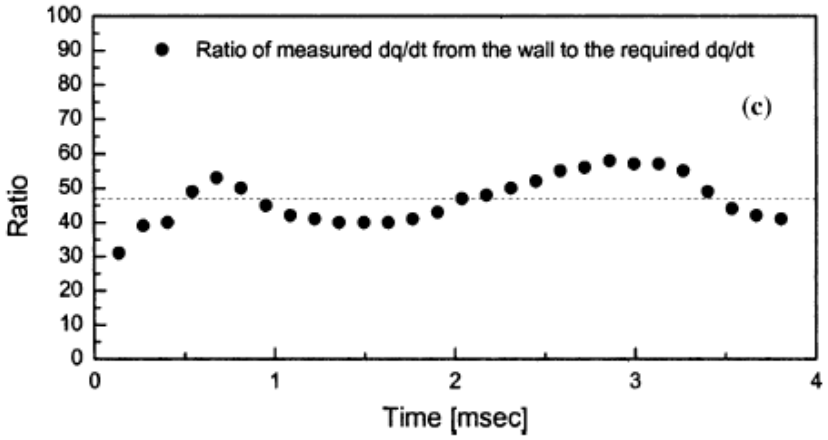

Figure 2.4. Ratio of measured heat from the wall to the required heat (R11).

Kim et al. (2006) used a microheater array maintained at a constant temperature and made additional measurements for R113 ($T_{sat} = 47.6\ ^{\circ}C$) for subcooled, saturated, and superheated pool conditions. The equivalent physical bubble radius was calculated from Eq. 2.3 and the results are plotted in Fig. 2.5 for various bulk temperatures.

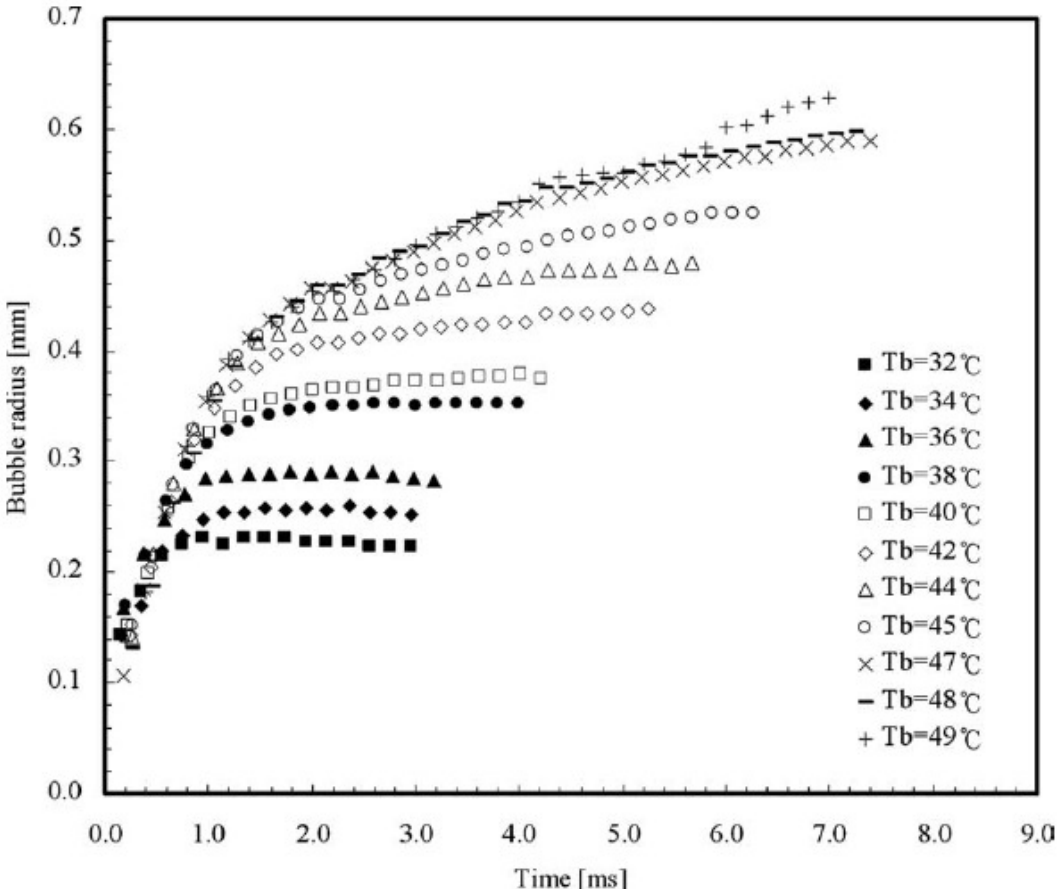

Figure 2.5. Equivalent bubble radius for different pool temperatures.
From Kim et al. (2006).

The ratio of measured heat to the required heat for various bulk temperatures are plotted in Fig. 2.6. This ratio is about 3.6 at a bulk temperature of 32 °C (due to condensation at the bubble cap) and decreased to 0.44 for a bulk temperature of 49 °C. The measured and required heat balanced at a bulk temperature of 40 °C. It should be noted that the results for the saturated pool condition was consistent with the observations of Lee et al. (2003 a,b).

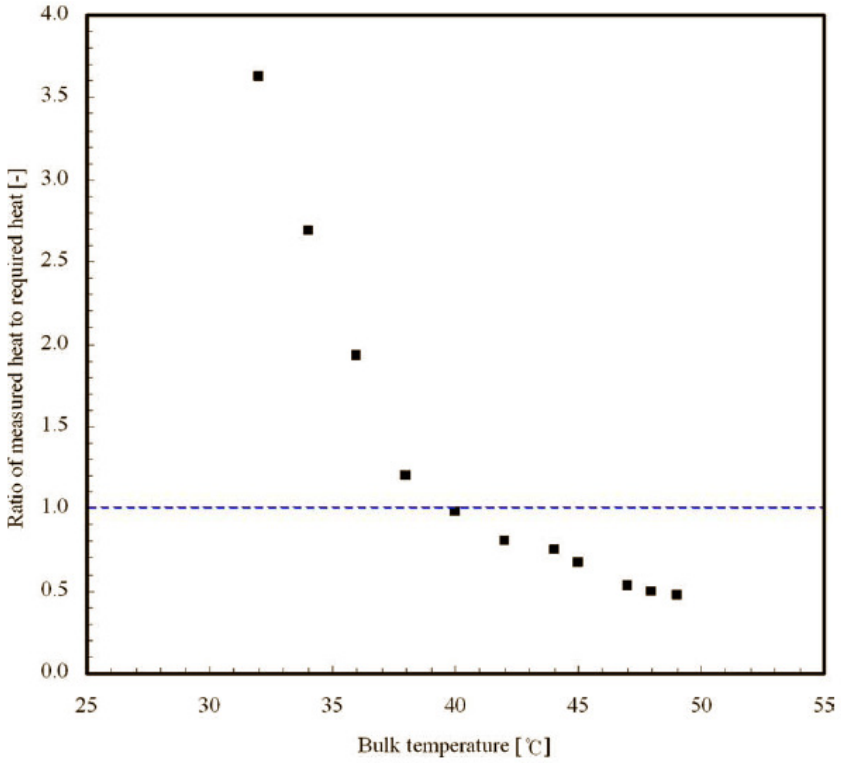

Figure 2.6. Ratio of measured wall heat transfer to heat required to grow bubble to observed size. From Kim et al. (2006).

The equivalent bubble diameter (based on the wall heat transfer) is plotted along with the physical diameter (T_b=42 °C) for the data of Kim et al. (2006) in Fig. 2.7. The corresponding test conditions for this plot are provided in Table 2.1. Physical diameter is considerably larger than the equivalent diameter indicating the contribution of superheated liquid layer is significant.

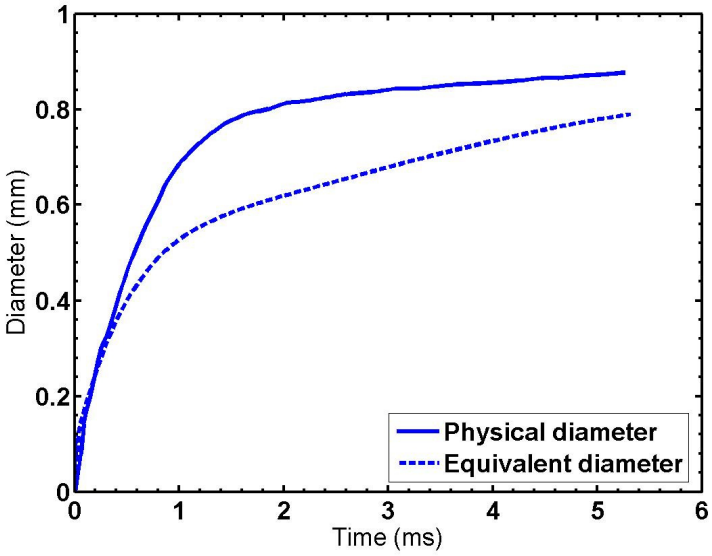

Figure 2.7. Comparison of physical and equivalent bubble diameters for the work of Kim et al. (2006).

Table 2.1. Test conditions associated with Fig. 2.7.

Fluid	R113
Pressure (atm)	1
T_w (℃)	72
T_{sat} (℃)	47.6
T_{bulk} (℃)	42
Superheat (℃)	24.4
Subcooling (℃)	5.6
Jakob Number	32.4

2.1.1.2. Micro Heat Flux Sensor Data

Moghaddam and Kiger (2009) measured the thermal field beneath the nucleating bubbles of FC-72 with a spatial resolution of 22-40 μm through fabrication of a sensor array (resistance temperature detectors) on the boiling surface (Fig. 2.8). They fabricated three cavities at the center of the sensor array to serve as artificial nucleation sites.

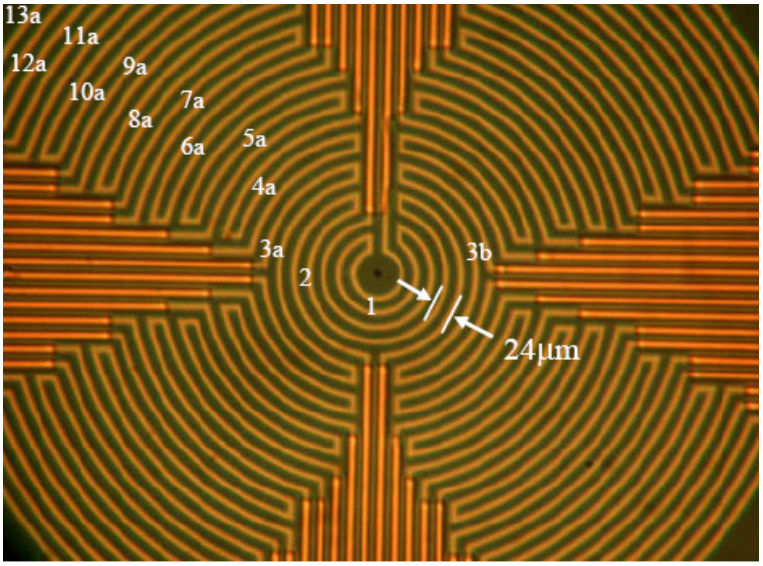

Figure 2.8. Top view of sensor array. From S. Moghaddam (2006).

A schematic of cross section of their device is given in Fig. 2.9. In addition to the sensor array, two single temperature sensors (H1 and H2) were placed within the composite wall. H1 was used to measure the temperature of the BCB/silicon interface. The purpose of H2 was to measure the total heat flux through the entire sensor array. The local heat flux provided to the working fluid was calculated from the temperature readings of H1 and the local temperature measurements from the sensor array.

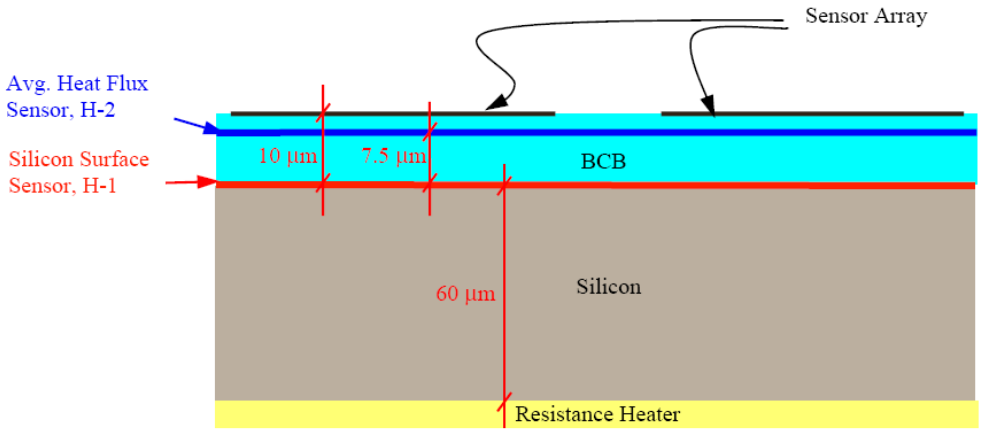

Figure 2.9. Schematic cross section of the device. From S. Moghaddam (2006).

They obtained data for the saturated pool conditions at various wall temperatures (Table 2.2). It should be noted that no waiting was observed between the bubbles with the exception of test No. 5 (lowest temperature) where there was a waiting time of 2.9 ms between the bubbles.

Table 2.2. Surface temperature for the study of Moghaddam and Kiger (2009).

Test No.	T_w (°C)
1	80.5
2	86.4
3	91.4
4	97.2
5	80.2

The readings of temperature sensors were related to the images of the bubble obtained from the side. The surface temperature data along with bubble images are given for Test No. 1 and 5 in Figs. 2.10 and 2.11. The initial formation of the bubble resulted in a sudden temperature drop at the center of the array (i.e. at sensor S-1) which then progressed over the subsequent sensors (i.e. sensors S-2 to S-4). The temperature drop at each sensor was started after the apparent contact line passed over the sensor. Moghaddam and Kiger (2009) concluded that this temperature drop was due to surface cooling associated with the microlayer evaporation. The surface temperature started to increase after the initial temperature drop indicating microlayer was mostly evaporated. A second decline in the temperature was observed after the advancing liquid front rewetted the dried out area. Note that the contact area expansion is significantly faster for the case with the waiting time and the surface experienced greater temperature drop during this time in comparison with the case with no waiting time.

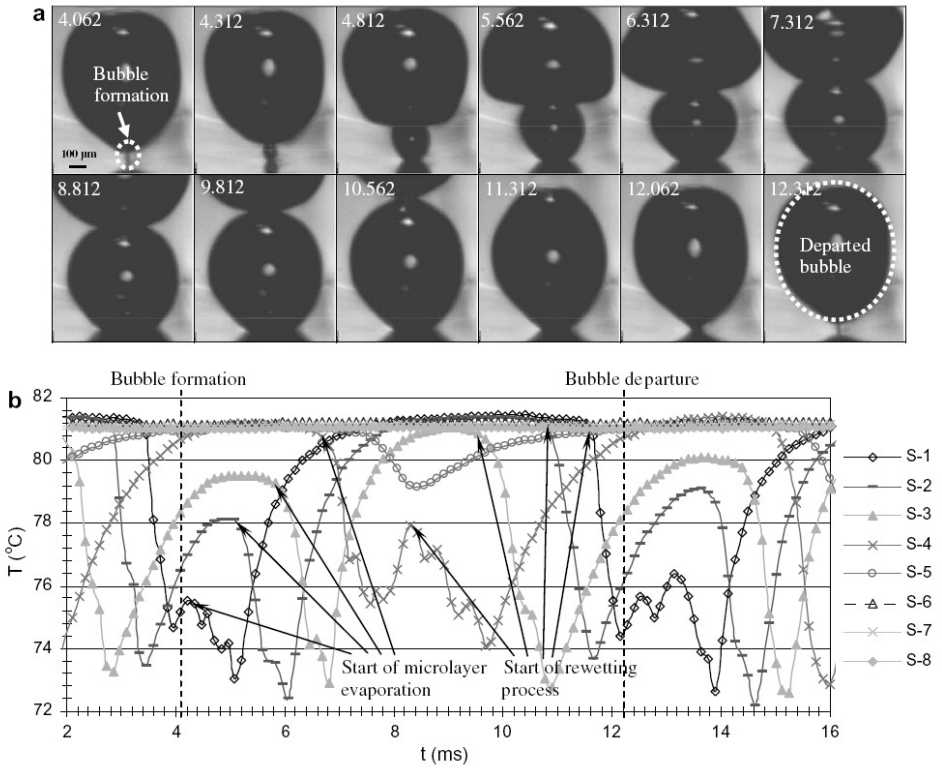

Figure 2.10. Test results at a surface temperature of 80.5 °C (Test No.1).
There is no waiting time between the bubbles. From Moghaddam and Kiger (2009).

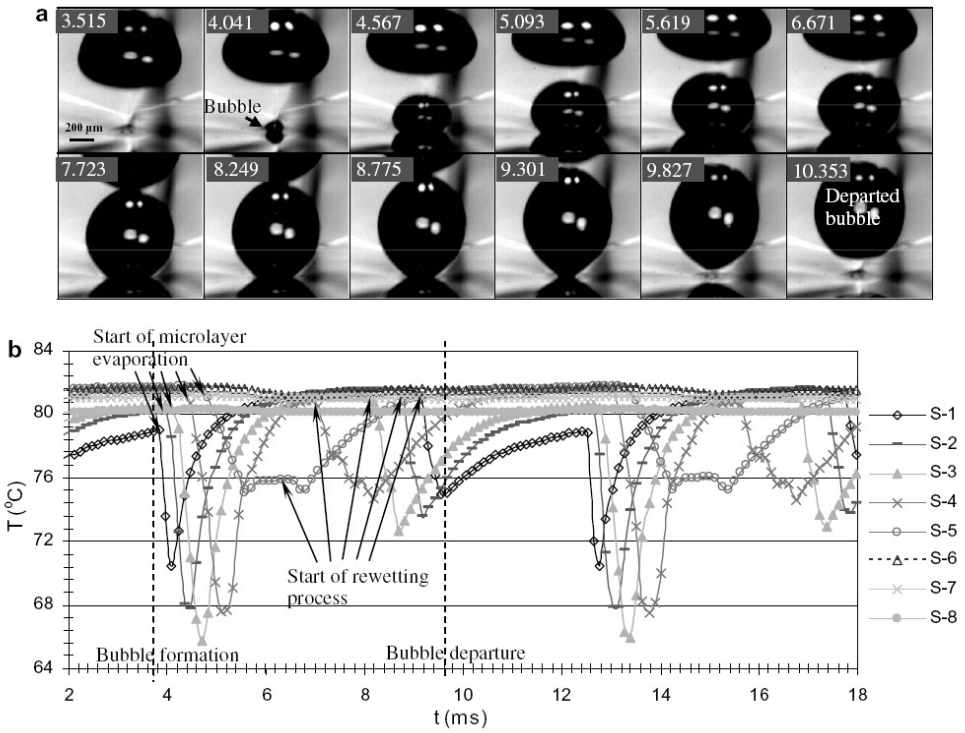

Figure 2.11. Test results at a surface temperature of 80.2 °C (Test No.5).
Waiting time between the bubbles is 2.9 ms. From Moghaddam and Kiger (2009).

Surface heat flux was numerically calculated and results are given in Fig. 2.12. Their work allowed the contribution of transient conduction and microconvection to be distinguished. They also found the contact line evaporation did not have significant contribution to the total heat transfer. The contribution of different heat transfer mechanisms for the cases without waiting time was found to change from: 1) 28.8% to 16.3% for microlayer evaporation, 2) 45.4% to 32.1% for transient conduction, and 3) 25.8 % to 51.6% for microconvection. For the case with waiting time, the contributions of different mechanisms were: 1) 26.5% for microlayer, 2) 32% for transient conduction, and 3) 41.4% for microconvection.

The equivalent bubble diameter (based on the wall heat transfer) is plotted along with the physical diameter for the data of Moghaddam and Kiger (2009) in Fig. 2.13. The corresponding test conditions are provided in Table 2.3. Physical diameter is significantly larger than the equivalent diameter indicating the superheated liquid layer is the main source of energy for the bubble.

Table 2.3. Test conditions associated with Fig. 2.13.

Test No.	1	5
Fluid	FC-72	FC-72
Pressure (atm)	1	1
T_w(°C)	80.5	80.2
T_{sat} (°C)	56.7	56.7
T_{bulk} (°C)	56.7	56.7
Superheat (°C)	23.8	23.5
Subcooling (°C)	0	0
Jakob Number	39.9	39.4

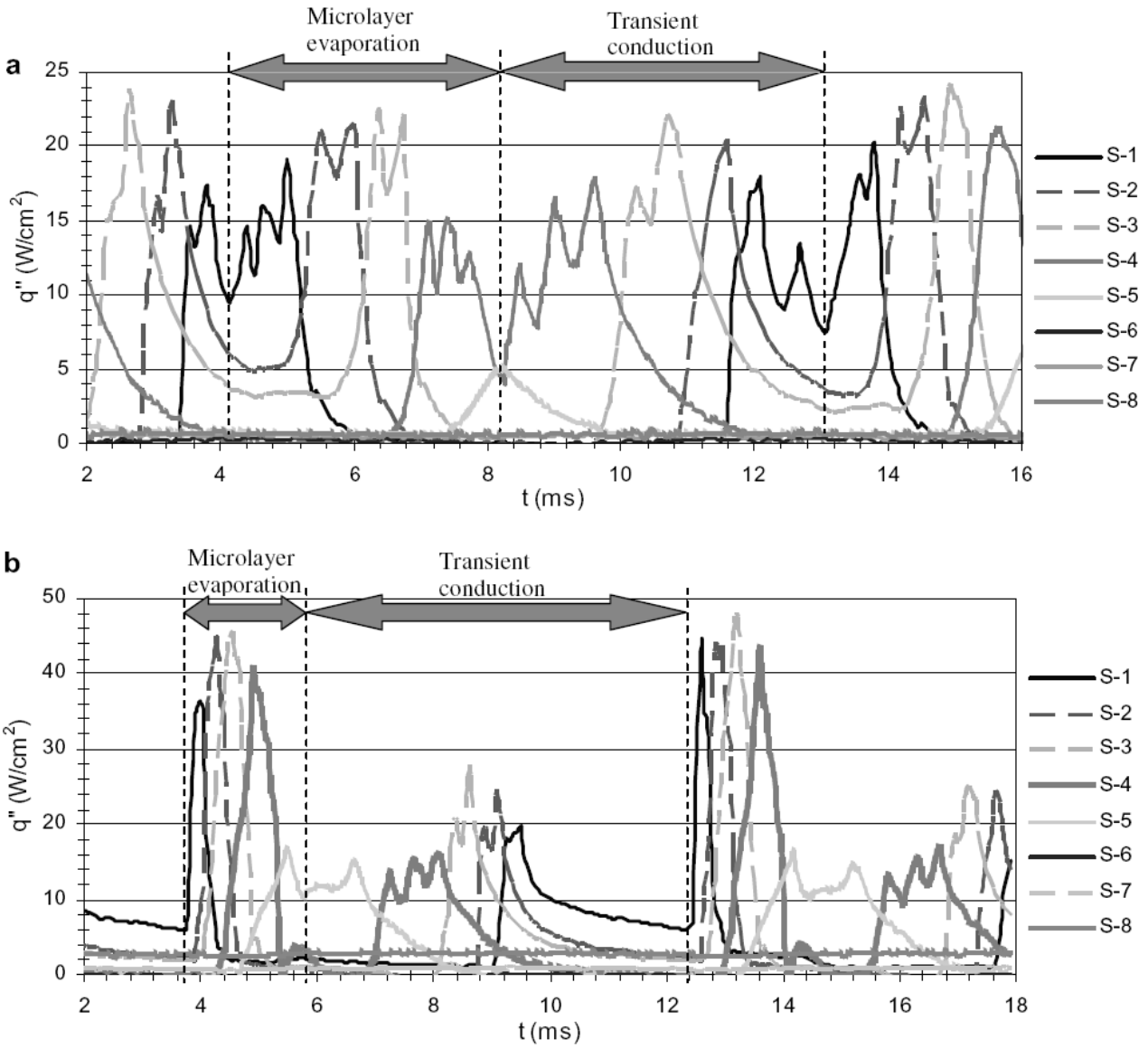

Figure 2.12. Heat flux results. a) Corresponding to Fig. 2.10. b) Corresponding to Fig. 2.11. From Moghaddam and Kiger (2009).

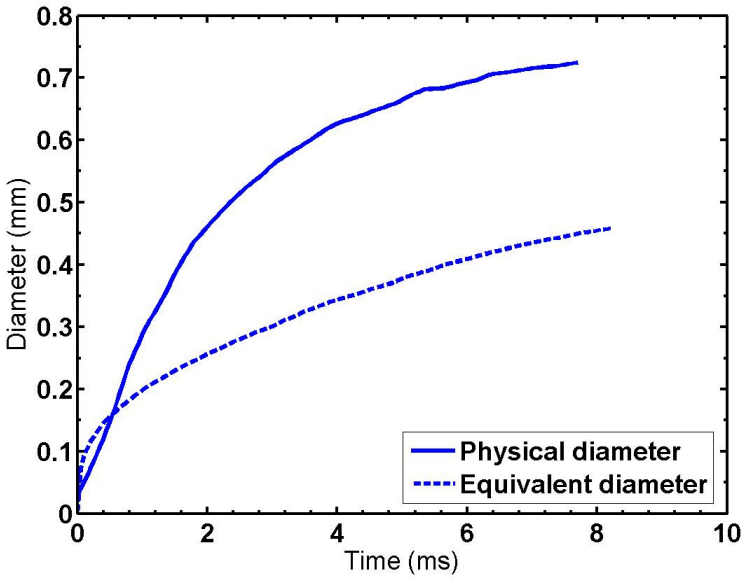

(a) Test No. 1.

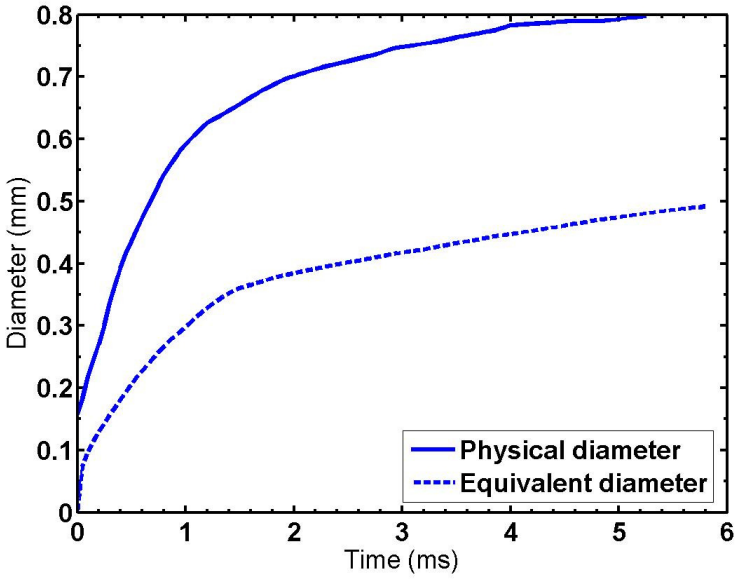

(b) Test No. 5.

Figure 2.13. Comparison of physical and equivalent bubble diameters for the work of Moghaddam and Kiger (2009).

2.1.1.3. Infrared Camera Data

Wagner and Stephan (2009) used an infrared (IR) camera to measure the temperature distribution on a back of 20 μm stainless steel heating foil during pool boiling of FC-84 and FC-3284. Surface heat flux distribution along with bubble images at various times during boiling of FC-3284 at 500 mbar is given in Fig. 2.14, as a representative example. They observed a high heat flux ring close to the contact line and insignificant heat flux within the inner region.

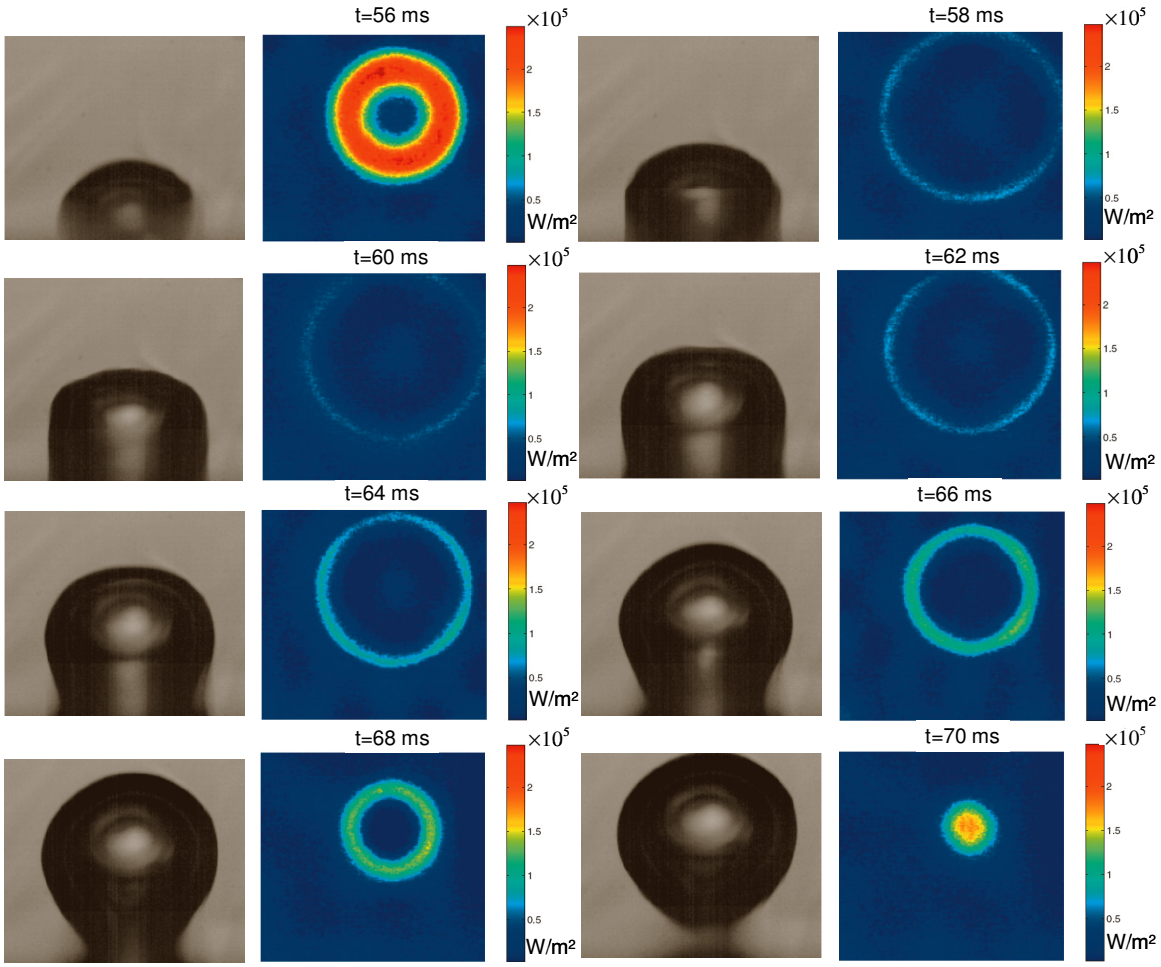

Figure 2.14. Bubble shape and heat flux distribution during boiling of FC-3284 at 500 mbar, q=1.29 W/cm^2. Adopted from Wagner and Stephan (2009).

The heat transfer through the micro-region (Q_mic) was calculated from the heat flux images shown in Fig. 2.14, and could include microlayer evaporation, contact line heat transfer, transient conduction, and microconvection. The total latent heat transfer into the bubble (Q_bub) was computed from changes in the bubble volume between time steps. Both Q_mic and Q_bub are plotted as a function of time in Fig. 2.15; micro-region heat transfer was found to be about 30% of the total bubble latent heat, indicating superheated liquid layer was the main source of energy for the bubble.

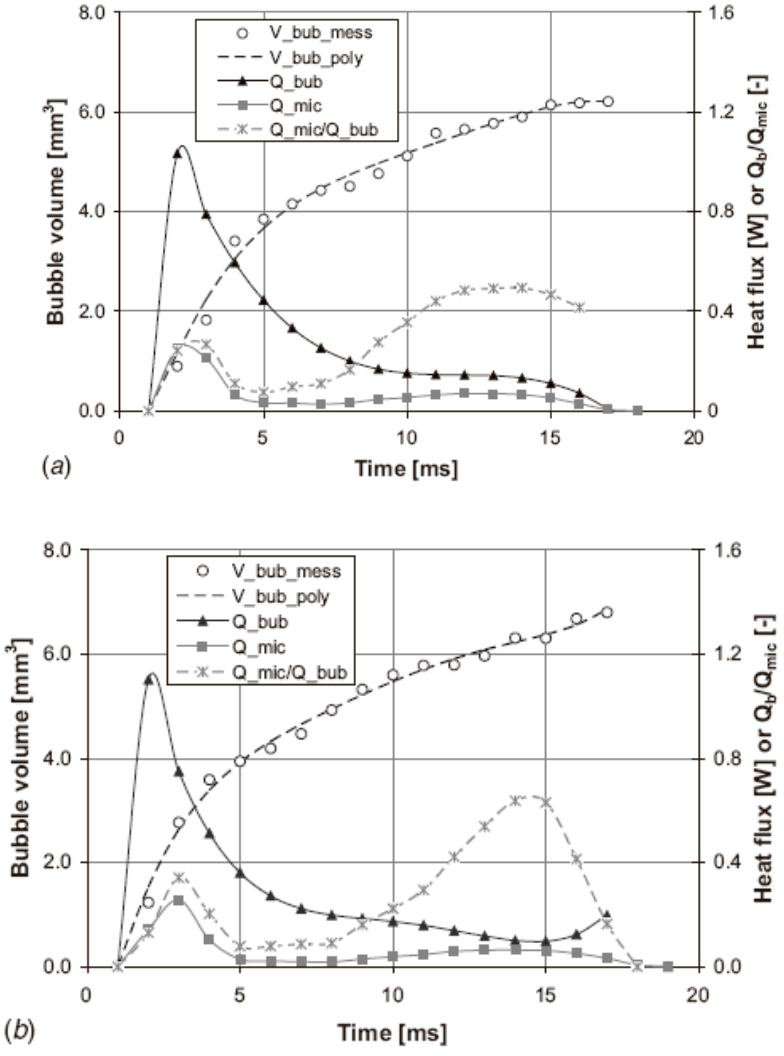

Figure 2.15. Bubble volume and heat transfer vs. time: a) FC-84 at q=1.2 W/cm^2 b) FC-3284 at q=1.29 W/cm^2. From Wagner and Stephan (2009).

The equivalent bubble diameter (based on the wall heat transfer) is plotted along with the physical diameter for the data of Wagner and Stephan (2009) in Fig. 2.16. Physical diameter is significantly larger than the equivalent diameter indicating the superheated liquid layer is the main source of energy for the bubble.

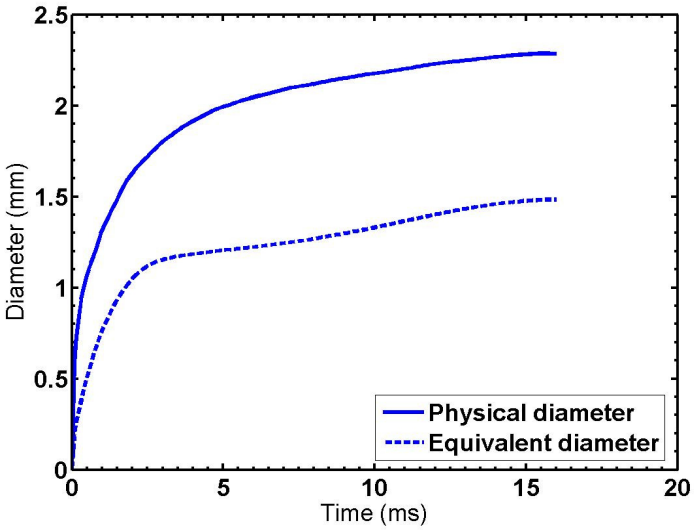

(a) FC-84 at q=1.2 W/cm^2

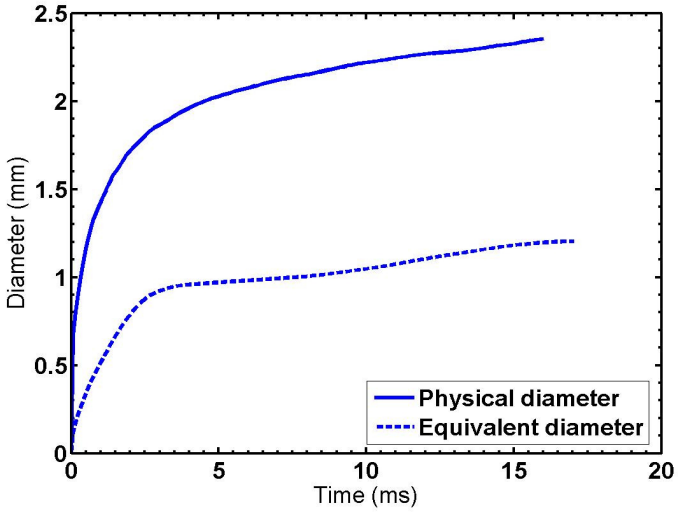

(b) FC-3284 at q=1.29 W/cm^2

Figure 2.16. Comparison of physical and equivalent bubble diameters for the work of Wagner and Stephan (2009).

Gerardi et al. (2009) used a high-speed IR camera to obtain the heater surface temperature distribution during saturated boiling of deionized water (T_{sat}=100 °C, 1 atm). The heater used in their study was a thin film of indium tin oxide (ITO) deposited on a 0.4 mm thick sapphire substrate. The IR camera measured the temperature distribution at solid-liquid interface while a high speed optical camera obtained the bubble images from the bottom. They observed that the physical bubble radius was significantly larger the equivalent bubble radius obtained from the instantaneous wall heat transfer (Fig. 2.17); a significant amount of energy required for bubble growth is provided from superheated liquid layer. The equivalent bubble diameter is plotted along with the physical bubble diameter in Fig. 2.18.

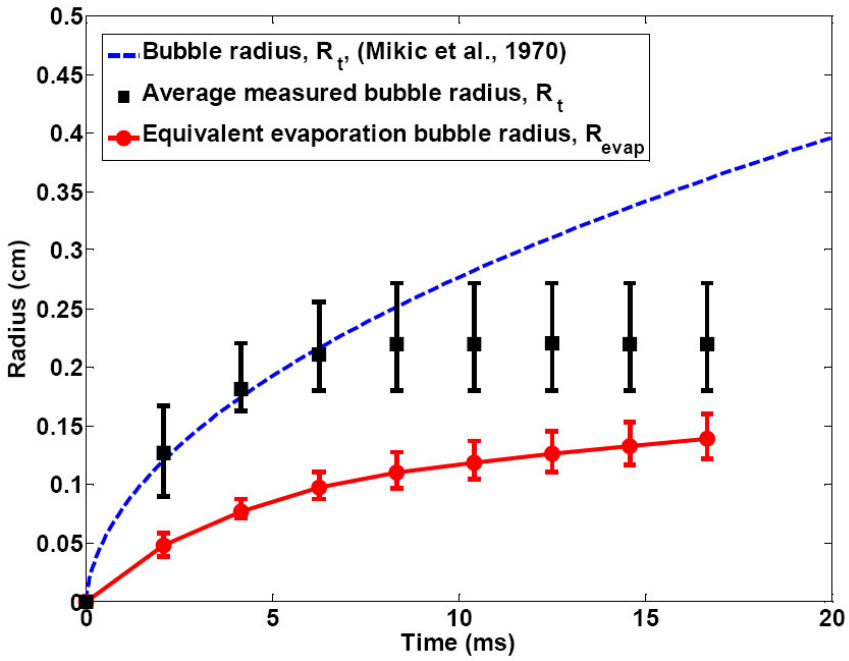

Figure 2.17. Comparison of measured, R_t, and equivalent bubble radius, R_{evap}. From Gerardi et al. (2009).

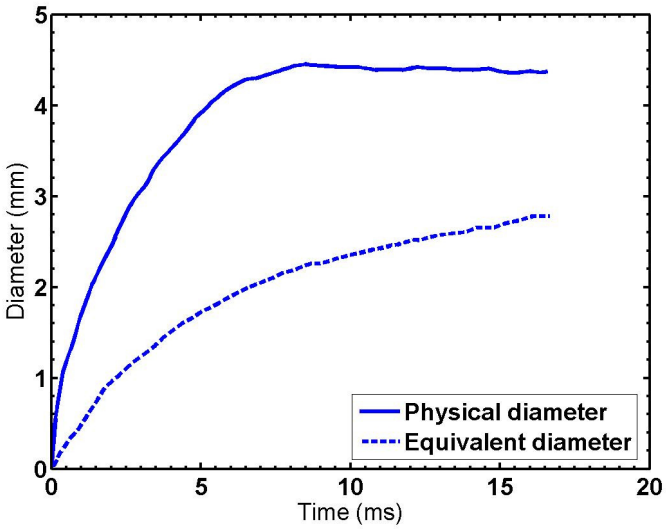

Figure 2.18. Comparison of physical and equivalent bubble diameters for the work of Gerardi et al. (2009).

A summary of experimental work for single bubble heat transfer is presented in Table 2.4.

Table 2.4. Summary of single bubble experimental work.

Study	Conclusion
Rohsenow (1951)	Single-phase convective heat transfer is dominant.
Forster and Greif (1959)	Bubbles act as micropumps that transport superheated liquid into the bulk as they grow and depart from the surface.
Tien (1962)	Wake generated behind a rising bubble responsible for heat removal from the surface.
Cooper and Lloyd (1969)	**Microlayer evaporation** is the dominant heat transfer mechanism.
Mikic and Rohsenow (1969)	**Transient conduction** is the dominant heat transfer mechanism.
Judd and Hwang (1976)	**Microlayer evaporation**, **transient conduction**, and **natural convection** are significant heat transfer mechanisms.
Haider and Webb (1997)	**Transient convection** is the dominant heat transfer mechanism.
Demiray and Kim (2004)	**Transient conduction** and/or **microconvection** is the dominant heat transfer mechanisms.
Myers et al. (2005)	**Superheated liquid layer** is the main source of energy for the bubble.
Kim et al. (2006)	**Superheated liquid layer** is the main source of energy for the bubble during subcooled boiling.
Moghaddam and Kiger (2009)	**Microlayer evaporation**, **transient conduction**, and **microconvection** are contributing mechanisms. **Transient conduction** and **microconvection** are the dominant heat transfer mechanisms.
Wagner and Stephan (2009)	**Superheated liquid layer** is the main source of energy for the bubble.
Gerardi et al. (2009)	**Superheated liquid layer** is the main source of energy for the bubble.

2.1.2. Numerical Simulations

Although many numerical simulations of bubble growth have been performed, the models were often built on an assumed heat transfer mechanism. The main focus of this

section is on reviewing the numerical studies with minimal simplifying assumptions in which the relevant contributions of different heat transfer mechanisms were identified.

Son et al. (1999) performed a complete numerical simulation of a growing and departing bubble on a horizontal surface. A finite difference scheme was used to solve the conservation of mass, momentum, and energy in the vapor-liquid layers. The computational domain was divided into macro and micro region (Fig. 2.19). The micro region contains the thin film that forms beneath the bubble whereas the macro region consists of the bubble and the liquid surrounding liquid. They concluded that the microlayer contributes about 20% to the total heat transfer.

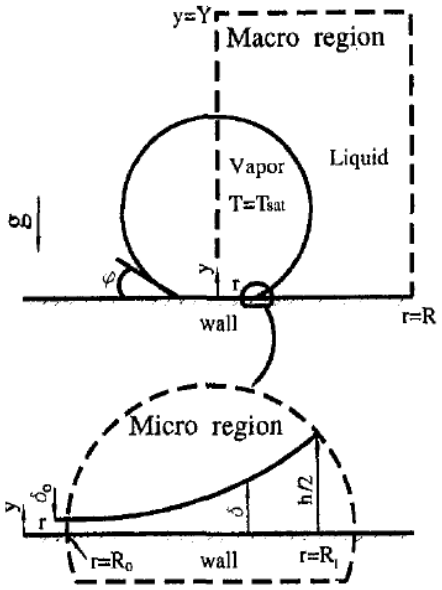

Figure 2.19. Macro and micro regions used in the numerical simulation. From Son et al. (1999).

Fuchs et al. (2006) performed a numerical simulation of growing, detaching and rising bubbles including waiting time between the bubbles. Definition of phases for the initial bubble cycle and subsequent bubble cycles is given in Fig. 2.20. Interfaces in their model are defined as shown in Fig. 2.21.

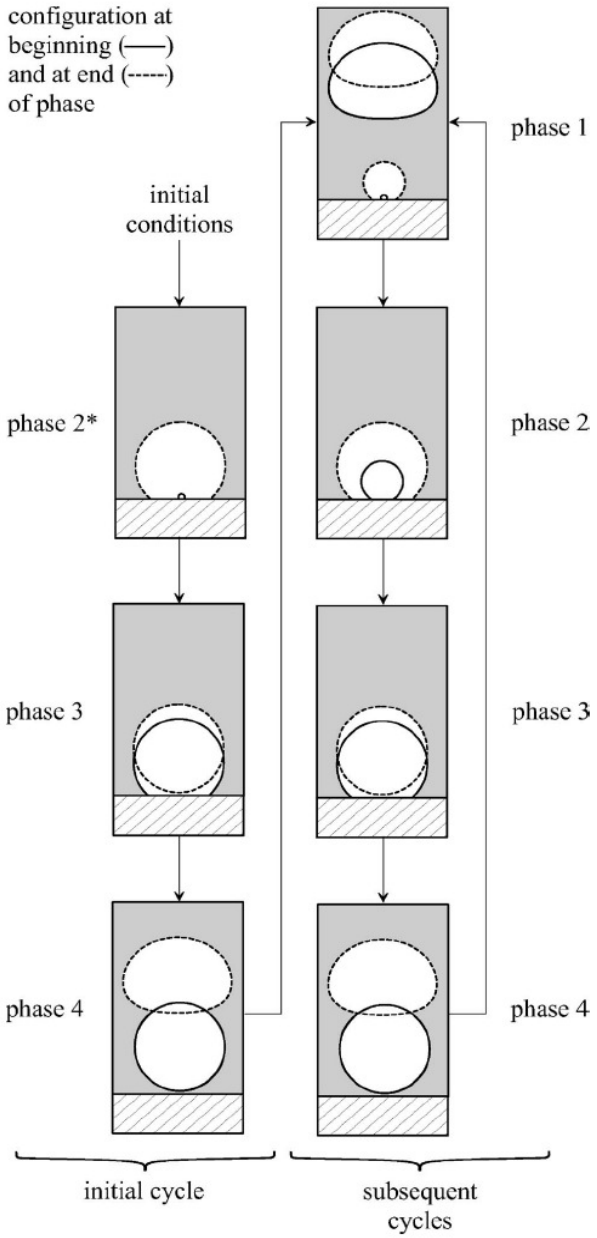

Figure 2.20. Definition of phases for the initial bubble cycle and subsequent bubble cycles. From Fuchs et al. (2006).

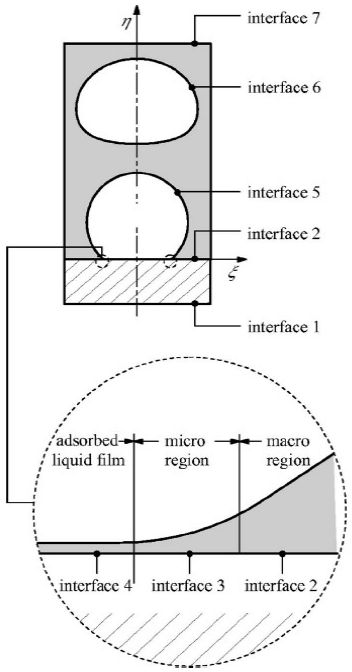

Figure 2.21. Interface definition. From Fuchs et al. (2006).

Time dependent heat transfer profiles through various interfaces is shown in Fig. 2.22. No heat is transferred through the adsorbed liquid film and the contribution of micro region (interface 3) was found to be 32%.

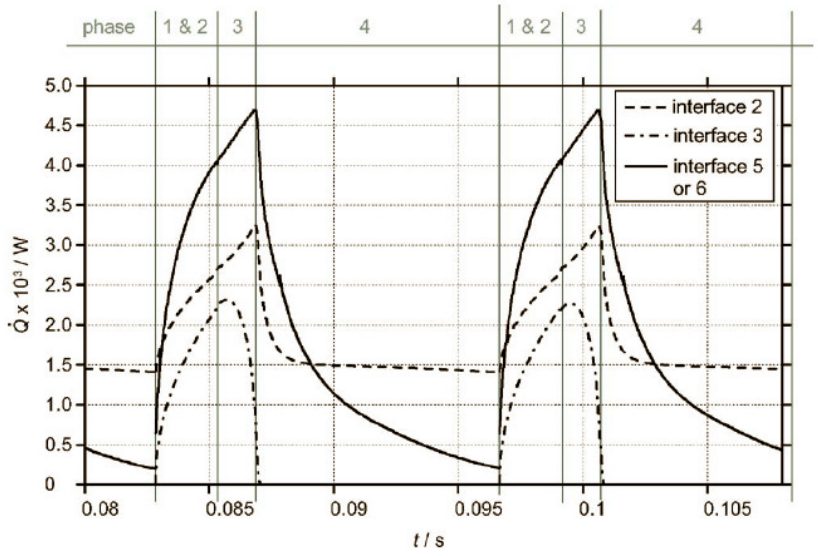

Figure 2.22. Time dependent heat flow through interfaces. (propane/n-butane, p_r=0.2, $T_w - T_{sat}$=8.7 K, $x_{L,1}$=0.245).

2.2. Bubble Merger Heat Transfer

Bubble merger process has been known to result in a heat transfer enhancement in the nucleate pool boiling. The merger could lead to a different contribution of heat transfer mechanisms to the overall heat transfer. Bubble merger (coalescence) could occur both in the vertical and lateral direction (Fig. 2.23). Vertical coalescence occurs when the growth velocity of a bubble is higher than the rising velocity of the previous bubble. This condition results in the formation of a single bubble elongated perpendicular to the heated surface. Lateral merger occurs when adjacent bubbles grow on the heated wall and get in contact to form a single bubble.

2.2.1. Experiments

Chen and Chung (2002) performed experiments using a microheater array to study the lateral merger during subcooled pool boiling of FC-72. They observed two major heat flux spikes for a typical cycle of boiling with coalescence: 1) spike corresponding to bubble coalescence, and 2) spike corresponding to bubble departure. In a similar study, Chen and Chung (2003) investigated the effects of the number of bubbles involved in the process and separation distances between them on the merger heat transfer. Heat fluxes were found to be proportional to the number of bubbles; they also found that heat transfer enhancement increases as the separation distance between the bubbles increases. The heat transfer enhancement was attributed to the rewetting of the dry heater and turbulent mixing effects.

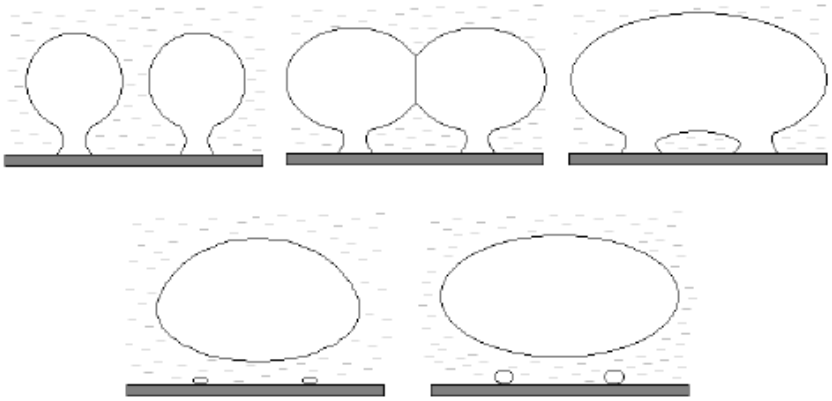

a) Lateral merger.

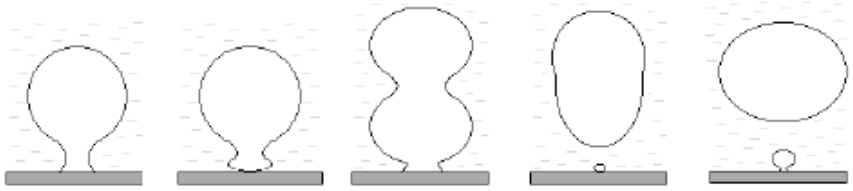

b) Vertical merger.

Figure 2.23. Schematic of lateral and vertical merger. Courtesy of C.R. Williamson and M.S. El-Genk (1991).

2.2.2. Numerical Studies

Son et al. (2002) performed a complete numerical simulation of bubble merger in the vertical direction to quantify the effect of bubble merger on the flow and temperature fields adjacent to the heater surface. The vapor-liquid interface was captured by a level set method. Fig. 2.24 depicts the effect of bubble growth and merger (two and three bubbles) on the Nusselt number based on the area average heat flux at the wall during two consecutive cycles.

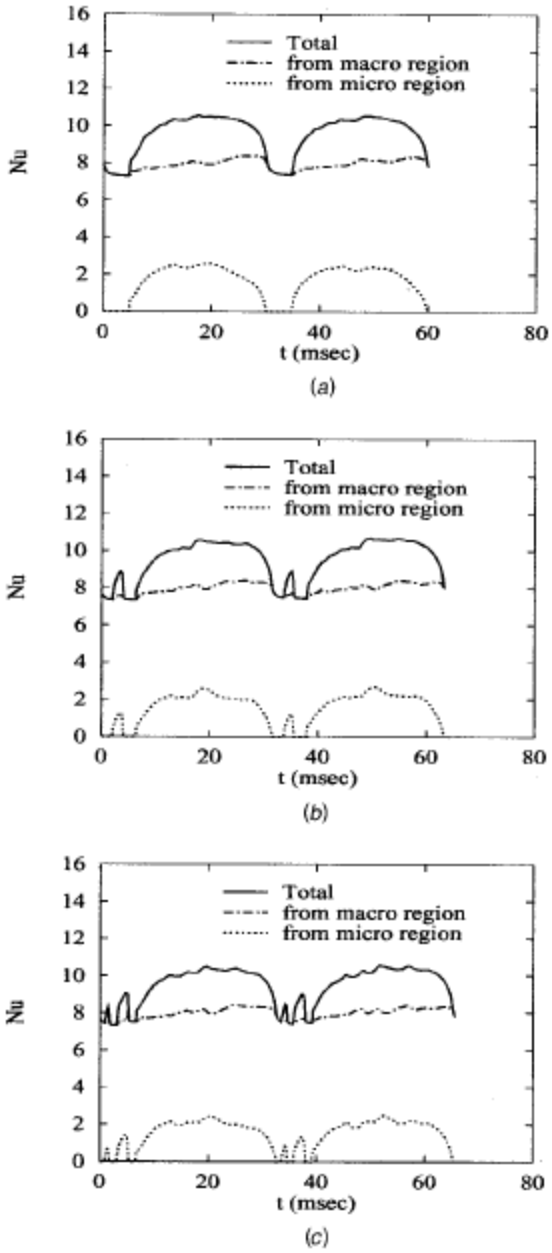

Figure 2.24. Variation in Nusselt number for ΔT=10 K and three waiting periods: a) 4.8 ms, single bubble b) 2.4 ms, vertical merger of two bubbles, and c) 1.28 ms, vertical merger of three bubbles. From Son et al. (2002).

Mukherjee and Dhir (2004) performed a numerical simulation to study lateral merger of vapor bubbles. Their results show the overall wall heat transfer increases significantly due to merger of multiple bubbles. A summary of the relevant merger heat transfer research is presented in Table 2.5.

Table 2.5. Summary of the relevant merger heat transfer research.

Study	Conclusion
Bonjour et al. (2000)	The coalescence of bubbles results in higher heat transfer coefficients than single-site boiling.
Chen and Chung (2002)	Heat transfer is highly enhanced (in comparison with single bubble results) as a result of lateral merger.
Chen and Chung (2003)	Heat transfer enhancement rate becomes higher as the separation distances between the bubbles increases.
Chen and Chung (2003)	Heat transfer enhancement for the coalescence of group of bubbles is proportional to the number of bubbles involved and the separation distances between bubbles.
Mukherjee and Dhir (2004)	Lateral merger of multiple bubbles significantly increases the overall wall heat transfer.

CHAPTER 3: EXPERIMENTAL SETUP AND METHODOLOGY

3.1. Heater Array

An array of 96 platinum resistance heater elements deposited on a quartz wafer provided local surface heat flux and temperature measurements. A photograph of the heater array is shown in Fig. 3.1. Each element in the array was approximately square in shape, nominally 0.27×0.27 mm^2 in size, and consisted of 5 μm wide platinum (Pt) lines spaced 5 μm apart. The nominal resistance and temperature coefficient of resistance (TCR) for each heater element in the array were 1000 Ω and 0.002 $°C^{-1}$. The heater was mounted on a pin grid array (PGA) package using epoxy adhesive, and conventional wire-bonding was used to make the electrical connection between the pads on the PGA package and the heater leads. The completed package (Fig. 3.2) was then mounted on a stack of PGA sockets soldered to a printed circuit board (PCB). Four ribbon cables provided the electrical connection between the heater and feedback circuits (discussed below). Details of the construction of a similar heater array are given in Rule and Kim, 1999.

3.2. Feedback Control Circuit

The temperature for each heater in the array was kept constant by individual feedback circuits similar to those used in hotwire anemometry (see Fig. 3.3 for a schematic). Any imbalance in the Wheatstone bridge was sensed by an amplifier, which

continually varied the power to the heater to bring the bridge back into balance. The temperature of the heater could be changed by changing the control resistor setting (varying the wiper position of the digital potentiometer). The instantaneous voltage required to keep each heater at a constant temperature was measured. The heat dissipated by a given heater was calculated directly from the provided voltage to the heater and the heater resistance. It should be noted that the voltage measured by the data acquisition was half of the provided voltage to the heater due to the use of a voltage divider which ensured that the voltage limits for the data acquisition boards were not exceeded.

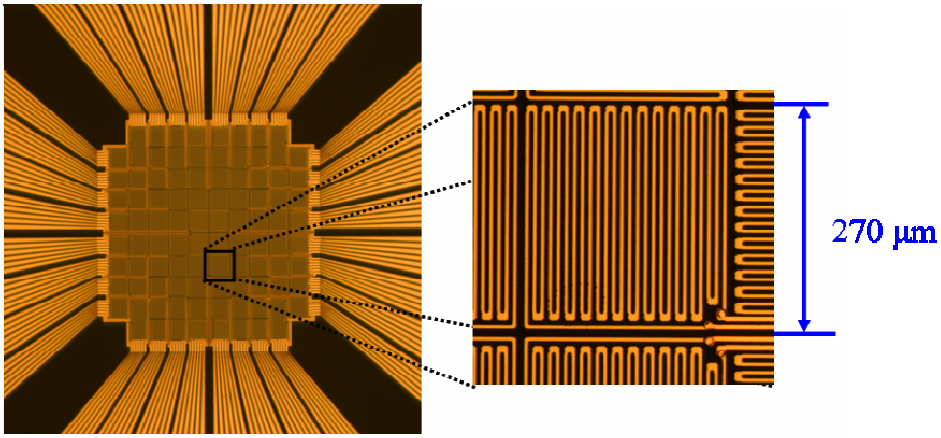

Figure 3.1. Photograph of heater array (Courtesy of J. Kim).

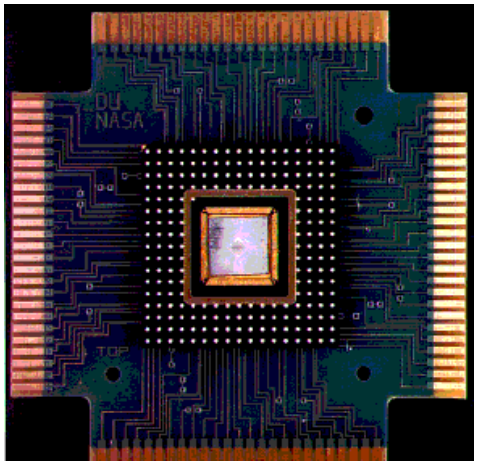

Figure 3.2. Heater array connected to PCB (Courtesy of J. Kim).

The value of R_2 at the top of the bridge was selected to be 200 KΩ to provide a small trickle current through the heater. The trickle current resulted in a voltage drop of about 400 mV across the heater even when the op-amp was not regulating. The induced voltage from the trickle current is required for the proper operation of the op-amp.

The frequency response of the circuit was measured to be 15 kHz (Rule and Kim, 1999) by measuring the response of the circuit to a step change in digital potentiometer position. Additional detail regarding the electronics of similar circuits is given in Bae et al. (1999).

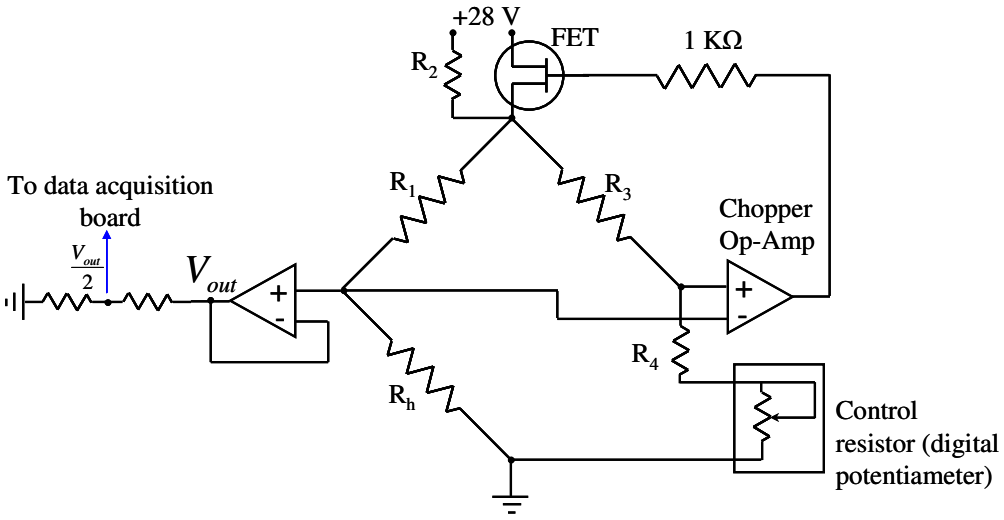

Figure 3.3 Schematic diagram of the feedback control circuit.

3.3. Heater Calibration

The heater array was calibrated by placing it in a constant temperature calibration oven. Images of the calibration setup are provided in Fig. 3.4. The oven temperature was held constant by the use of two temperature controllers, two thermocouples, and two thin film heaters. It should be noted that the heater was allowed to equilibrate within the oven for more than two hours before the calibration program was run (discussed below). A

NIST calibrated thermocouple was attached close (see Fig. 3.4) to the heater PGA package using Kapton high-temperature tape to monitor the heater temperature.

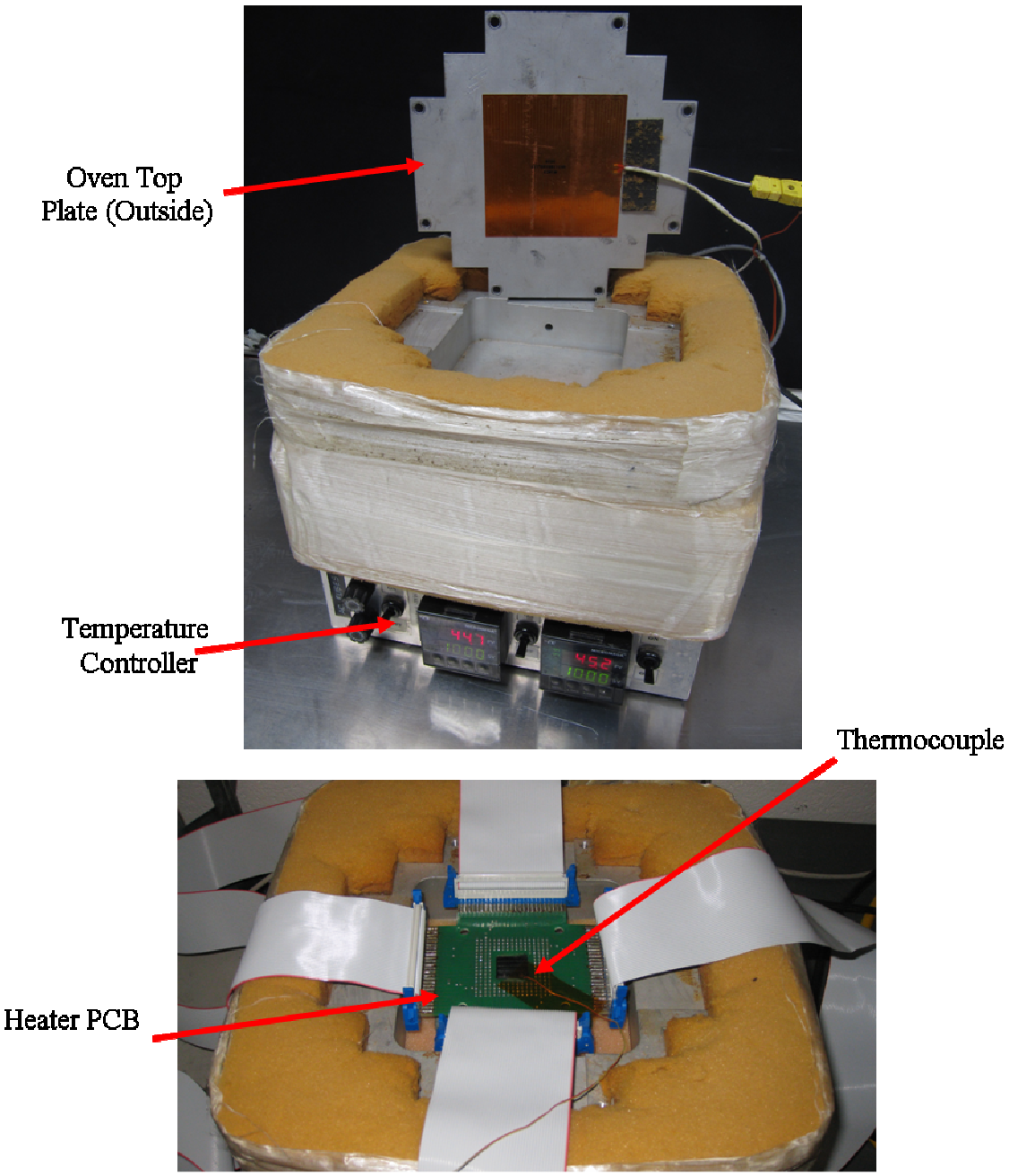

Figure 3.4. Calibration oven (top), top view of PCB inside oven (bottom).

The nominal heater resistance at a given temperature is determined from Eq. 3.1.

$$R_i = R_{ref,i}(1 + \alpha \Delta T) \tag{3.1}$$

where $R_{ref,i}$ is the heater resistance measured at a reference temperature, α is the temperature coefficient of resistance (TCR), and ΔT is the difference between the set temperature and reference temperature.

The temperature coefficient of resistance was calculated (from Eq. 3.1) for a quarter of the heater array by measuring the individual heater resistances at two temperatures. The average value for α was found to be 0.0021 $°C^{-1}$ and used for the purpose of evaluating the individual heater resistances at any given temperature. TCR for individual heaters was sufficiently close to the average value and the standard deviation was found to be 5.95×10^{-5} $°C^{-1}$. A sample plot of Resistance versus temperature (heater 23) is given in Fig. 3.5.

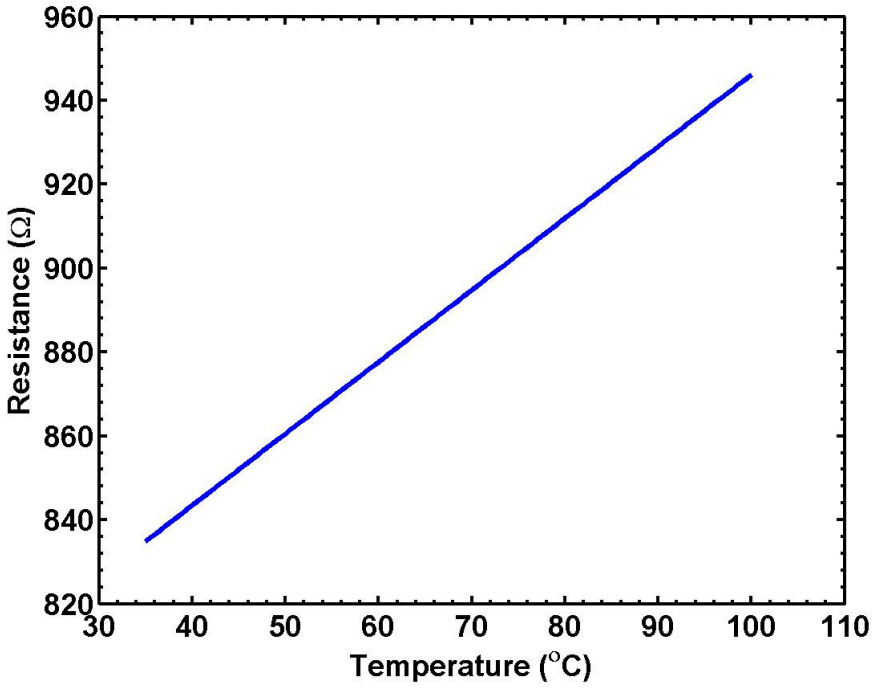

Figure 3.5. Resistance versus temperature for heater 23.

At the steady state temperature, the calibration program determined the digital potentiometer resistance setting, called DQ values, for each circuit. The calibration routine consisted of incrementing the DQ values for each circuit until the Wheatstone bridge was balanced for that specific heater temperature.

These final DQ values were written to a text file (one DQ file for each temperature) for the future use in the experiment. It should be noted that the oven temperature was held constant within 0.1 °C of the set temperature during the calibration of the full array.

A sample plot of the DQ values versus temperature (heater 23) is given in Fig. 3.6. The calibration points are marked by squares in this figure. A MATLAB code was developed to perform a linear interpolation (blue line in Fig. 3.6) to obtain the DQ values for temperatures other than the calibration temperatures; the code created DQ files at increments of 0.5 °C.

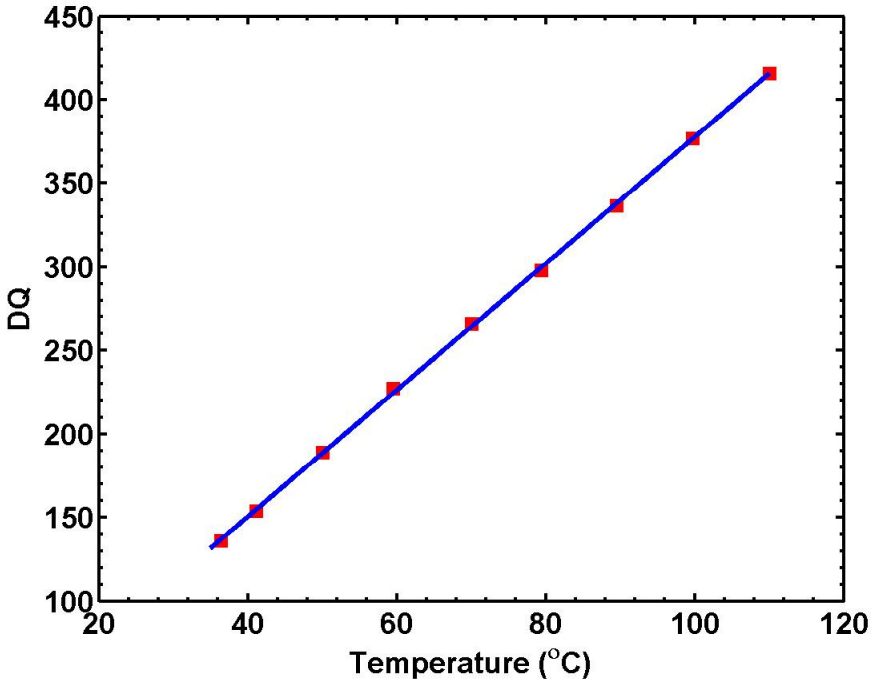

Figure 3.6. DQ versus temperature for heater 23.

The temperature resolution for the digital potentiometer can be calculated as:

$$\frac{(110-35)\,^{\circ}C}{DQ_{110}-DQ_{35}}=\frac{75\,^{\circ}C}{284}=0.26\,^{\circ}C \text{ (per increment)}$$

3.4. Data Acquisition System

Two data acquisition cards made by Measurement Computing (CIO-DAS6402/12), each capable of scanning 64 analog input channels at a maximum speed of 200 kHz, were installed on a PC. The first card sampled the first 62 heaters while the second card sampled the remaining 34 heaters. The system was used to obtain time-resolved voltage data at 3703 Hz from each heater for 2 s. The sampling frequency was chosen based on the maximum available image capturing frequency of the high speed camera as discussed in Section 3.6.

3.5. Boiling Rig

A schematic of the boiling rig used in this study is shown in Fig. 3.7. The test chamber was filled with approximately 3 L of pentane. In order to minimize the effects of dissolved gas, the fluid was degassed by repeatedly pulling a vacuum on the chamber until the pressure within the chamber asymptotically approached the vapor pressure of pentane.

The bellows and the surrounding housing allowed the test section pressure to be changed when needed. Bulk fluid temperature was controlled by the use a temperature controller, a series of Kapton heaters attached to the chamber, and a solid state relay (to control the current flowing through the Kapton heaters).

Three glass windows (two side illuminating windows and a front viewing window) provided optical access to the chamber. In order to prevent individual heaters from shutting off at low heat transfer levels, the heater array was cooled from the bottom using an air jet. The air flow was generated by passing air from a pressurized line at a typical pressure of 40-50 psi through a Vortex tube. The Vortex tube cools the air several degrees, and then the air passes through a nozzle of 3 mm diameter where it exists at a typical temperature of 8 °C.

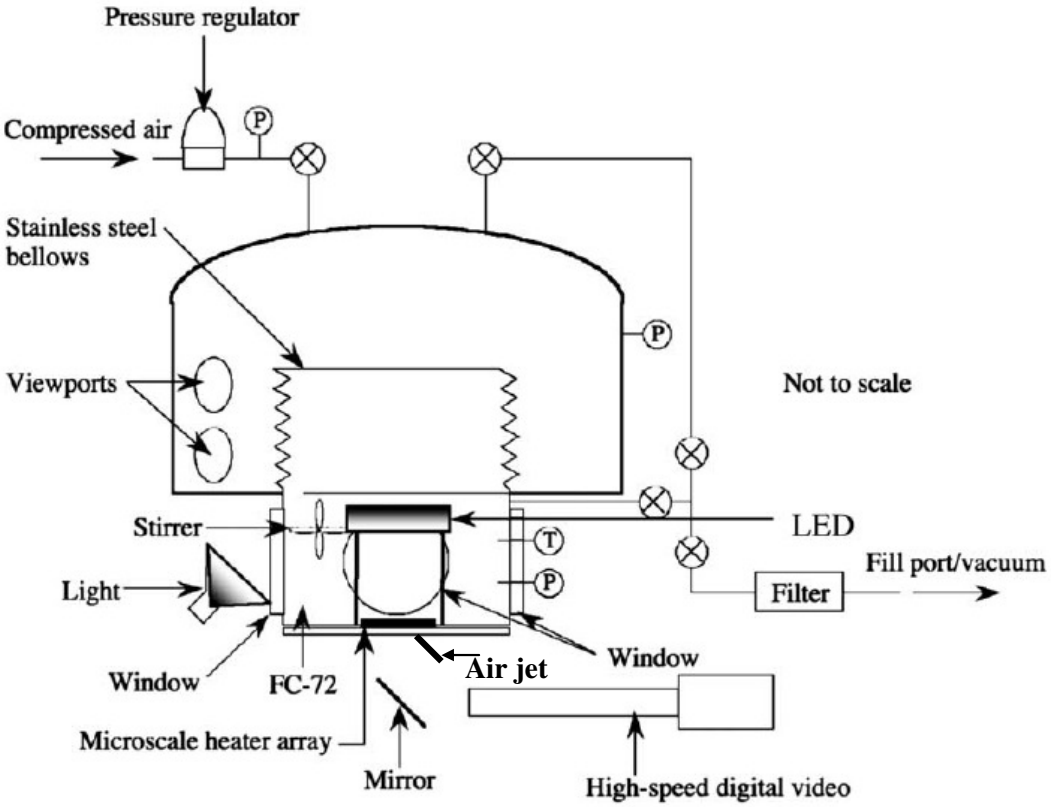

Figure 3.7. Schematic of test apparatus (Courtesy of J. Kim).

3.6. High Speed Video

The semi-transparent nature of the heater array enabled images to be taken from below with a high-speed digital video camera (Vision Research Phantom IV) set to acquire 256 × 256 resolution images at 3703 fps. A second high-speed digital video camera (Vision Research Phantom IV) was used to record side-view images at the same speed and resolution through the front viewing window. Two halogen lamps were aimed to illuminate the boiling chamber through the side illuminating windows. Due to the heat produced by the lamp, the lamp was turned on only during the data acquisition time.

Recording of both cameras was initiated by closing an external trigger switch (Fig. 3.8). Data acquisition boards were triggered from the inverted trigger signal from the cameras, enabling heat transfer measurements and video records to be initiated simultaneously. The assembled test apparatus is shown in Fig. 3.9.

Data at various experimental conditions were obtained to investigate the underlying heat transfer mechanisms associated with different bubble dynamics. In order to investigate the heat transfer mechanisms, heat transfer variation from individual heaters as well as sum of the heat transfer from some selected heaters were calculated. The data reduction methods and experimental results are discussed in the subsequent chapters.

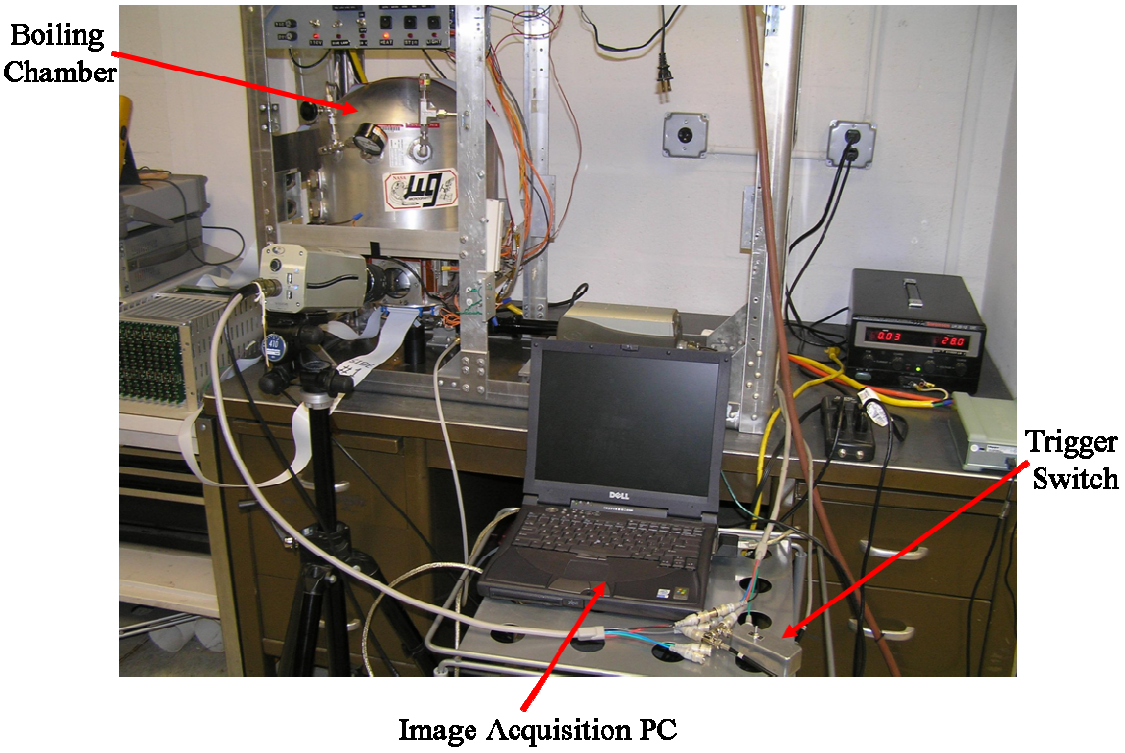

Figure 3.8. Close-up view of the boiling chamber and imaging system.

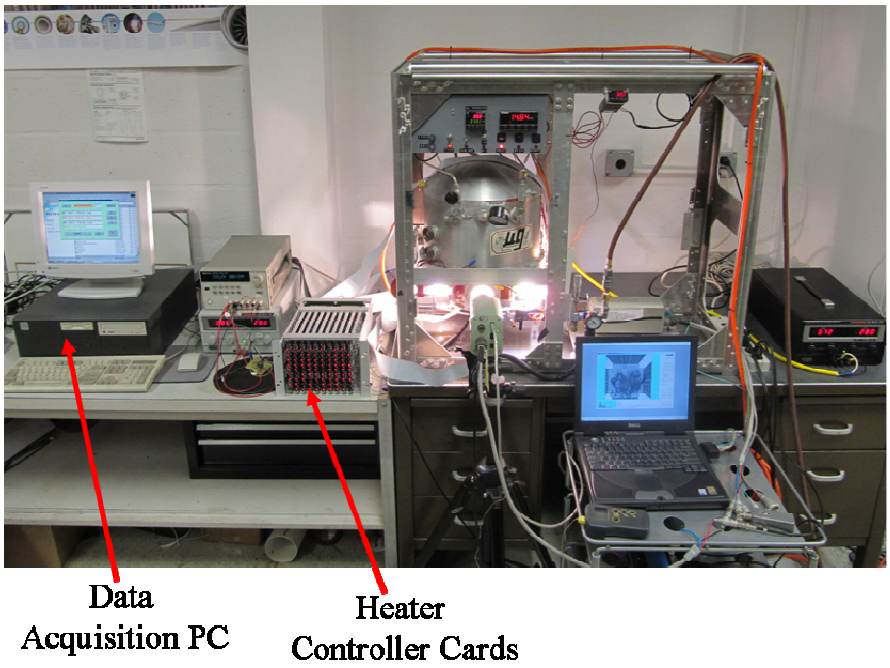

Figure 3.9. Assembled test setup.

CHAPTER 4: DATA REDUCTION AND UNCERTAINTY ANALYSIS

The main objective of the data reduction is to determine the heat transfer from the surface of the microheater array to the boiling fluid. The data reduction procedure along with an uncertainty analysis is provided in this chapter.

4.1. Data Reduction

As was discussed in Chapter 3, the data acquisition unit measures the transient voltage from each heater element. The voltage reading along with corresponding resistance for each heater was used to calculate the raw heat transfer from each heater element ($\dot{q}_{raw,i}$), Eq. 4.1.

$$\dot{q}_{raw,i} = \frac{V_i^2}{R_i} \tag{4.1}$$

As it was discussed in the heater calibration section, heater resistance is a function of temperature. The heater resistances can be calculated from Eq. 4.2:

$$R_i = R_{ref,i}(1 + \alpha \Delta T) \tag{4.2}$$

It should be noted that some of the raw heat transfer is conducted from the heater elements to the quartz substrate (substrate conduction) and can be removed from the back by the air jet or lost by natural convection to the bulk liquid. The heat transfer due to substrate conduction and natural convection is called the baseline heat transfer ($\dot{q}_{baseline}$). In this study, we are interested in the heat transfer induced by bubble action. The heat transfer excursions around a slowly varying baseline were assumed to be due to bubble formation and departure. The baseline of the heat transfer curve exhibited a low frequency oscillation (discussed in the Experimental Results chapter), which is likely due

to natural convection flow over the heater driven by the temperature difference between the bulk liquid and the heater array. To obtain the effect of the bubble only, the baseline heat transfer was subtracted from the total time-resolved heat transfer (Eq. 4.3).

$$\dot{q}_{bubble} = \dot{q}_{raw} - \dot{q}_{baseline} \tag{4.3}$$

The resulting heat transfer curve could exhibit both positive and negative values. Negative values of heat transfer result if liquid dryout during bubble growth above a heater occurred, resulting in lower heat transfer than would have occurred in the case of natural convection in the absence of a bubble. Details of calculation of bubble and baseline heat transfer are discussed for each experiment presented in Chapter 5.

4.2. Uncertainty Analysis

The uncertainties in calculating the heat transfer resistance was calculated using Eq. 4.4.

$$u_{R_i} = \sqrt{\left(\frac{\partial R_i}{\partial R_{ref,i}} u_{R_{ref,i}}\right)^2 + \left(\frac{\partial R_i}{\partial \alpha} u_\alpha\right)^2 + \left(\frac{\partial R_i}{\partial \Delta T} u_{\Delta T}\right)^2} \tag{4.4}$$

where the uncertainties in reference heater resistance (Fluke multimeter error) ($u_{ref,i}$), temperature coefficient of resistance (u_α), and temperature difference ($u_{\Delta T}$), were estimated to be 0.4%, 5%, and 1 °C respectively. The uncertainty in heat transfer resistance was calculated to be 0.5%.

The uncertainty in calculating the raw heat transfer was calculated using Eq. 4.5.

$$u_{\dot{q}_{raw,i}} = \sqrt{\left(\frac{\partial \dot{q}}{\partial V_i} u_{V_i}\right)^2 + \left(\frac{\partial \dot{q}}{\partial R_i} u_{R_i}\right)^2} \tag{4.5}$$

where the uncertainties in voltage (data acquisition board) (u_{V_i}) and heater resistance (u_{R_i}) were estimated to be 25 mV, and 0.5% respectively. The uncertainty in the raw heat transfer was calculated to be 3.4%.

If a functioning heater is next to a nonfunctioning heater (which acts as a local heat sink), the power required to keep it at constant temperature can change depending on the heat loss from the nonfunctioning heater, increasing the uncertainty. The total uncertainty due to uncertainties in substrate conduction, the curve fit, and nonfunctioning heaters is 0.3 mW for a single heater in the array. The uncertainty in the wall temperature is due to the limited resolution of the digital potentiometer, and is taken to correspond to two increments, or less than 1 °C.

Chapter 5: Experimental Results

5.1. Introduction

Pool boiling heat transfer behavior associated with different bubble dynamics are discussed in this chapter. Sections 5.2 through 5.4 of this chapter address single bubble dynamics for different bubble growth and waiting times. Dominant heat transfer mechanisms related to these three cases are discussed. Section 5.5 concludes the experimental results pertaining to the single bubble heat transfer. Section 5.6 addresses the heat transfer behavior during lateral bubble merger processes.

5.2. Sequence of Single Bubbles with Minimal Waiting Time

The objective of this experiment was to study the heat transfer behavior related to single bubbles departing sequentially from the heater. Despite many attempts, this was not achieved when the temperature distribution on the heater was uniform. The numbering for the heater elements is given in Fig. 5.1. These numbers serve as ID numbers for the individual heaters. In order to obtain the single bubble data, the temperature distribution on the heater was varied (i.e. the middle heaters were set to higher temperatures as indicated in Fig. 5.2.) until single bubbles were observed.

A sequence of bubbles formed on a subset of the heater array called the “selected region”. The heater numbers for the 28 heaters in the selected region as well as the array temperature distribution are given in Fig. 5.2. Note that the bottom two rows of the heaters were turned off to avoid lateral merges between the bubbles, and that two of the

heaters (56 and 71) are nonfunctional. The test conditions for the experiment are provided in Table 5.1. In order to initiate boiling, the heater temperature was set to higher temperatures (about 90 °C) originally and then reduced to the desired set temperature.

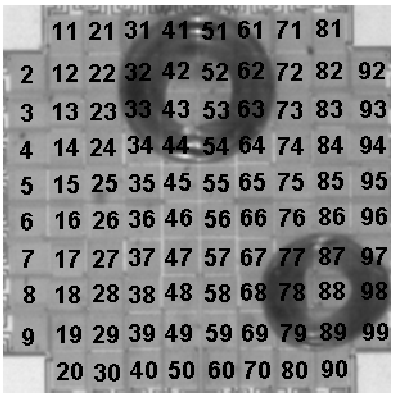

Figure 5.1. Numbering of the heaters.

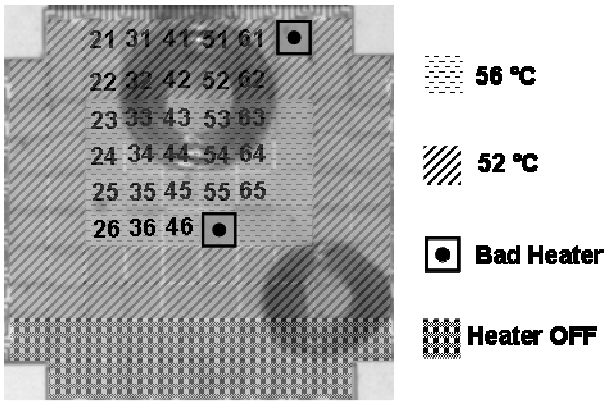

Figure 5.2. Heater temperature distribution and the selected region.

Table 5.1. Test conditions for sequence of bubbles with minimal waiting time.

Pressure (atm)	1
T_w (°C)	52-56
T_{sat} (°C)	35.8
T_{bulk} (°C)	31.6
Superheat (°C)	16.2-20.2
Subcooling (°C)	4.2
Jakob Number	21.9-27.3
Air jet	ON

Note: The heater was set to higher temperatures (about 90 °C) to initiate boiling.

5.2.1. Total and Bubble Heat Transfer

The total heat transfer for the selected region of the heater array was found by summing the instantaneous heat transfer of these elements at each time step. Heat transfer excursions from the baseline due to nucleating bubbles on the selected region are shown in Fig. 5.3. The baseline heat transfer corresponding to the natural convection and substrate conduction was calculated by averaging the heat transfer for some selected points before and after the sequence of bubbles. The pre-sequence baseline was sufficiently close to the post-sequence baseline (1.7 mW difference). Bubble heat transfer was calculated by subtracting the pre-sequence baseline from the total heat transfer.

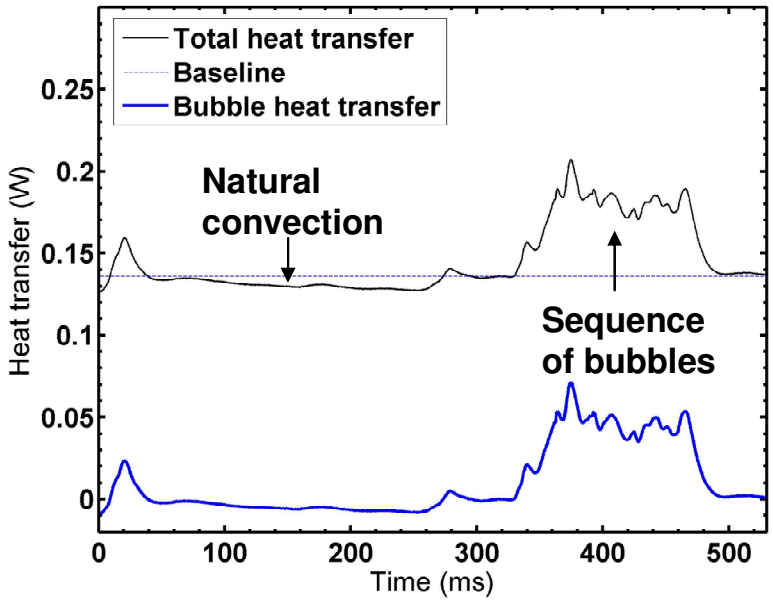

Figure 5.3. Bubble heat transfer calculation.

A close-up view of Fig. 5.3 indicating the sequence of bubbles and corresponding nucleation and departure times for each bubble are given in Fig. 5.4 and Table 5.2 respectively.

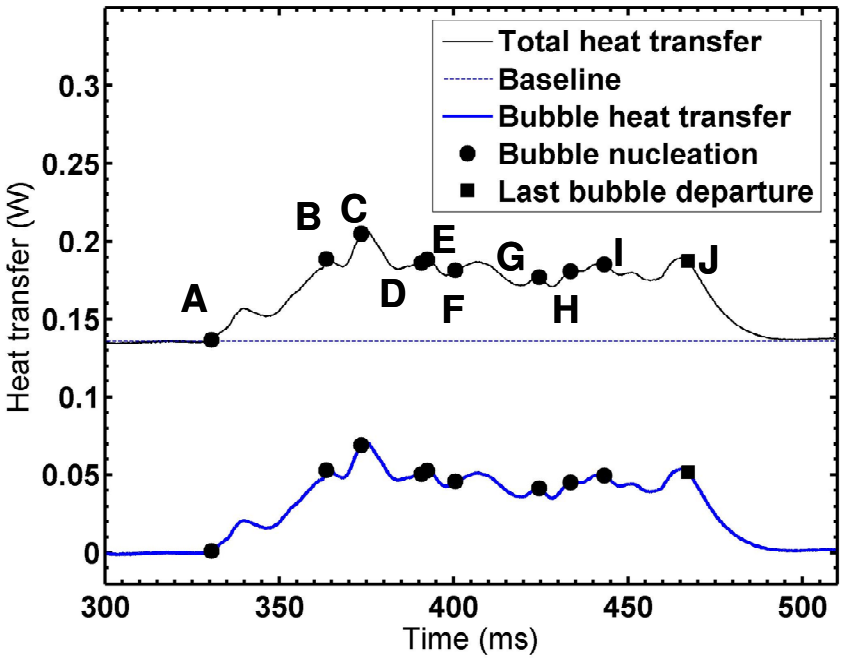

Figure 5.4. Heat transfer associated with the sequence of bubbles.

Table 5.2. Nucleation and departure times for the sequence of bubbles.

Region	Description	Nucleation time (ms)	Departure time (ms)	Waiting time (ms)
A-B	BM (merging event)	330.54	363.76	NA
B-C	Bubble 1	363.49	373.75	NA
C-D	Bubble 2	373.48	390.76	NA
D-E	Bubble 3	390.76	391.57	0
E-F	Bubble 4	392.38	400.22	0.81
F-G	Bubble 5	400.49	423.98	0.27
G-H	Bubble 6	424.52	432.35	0.54
H-I	Bubble 7	433.43	442.34	1.08
I-J	Bubble 8	443.15	467.19	0.81

The formation of the first bubble on the selected region occurs at 330.54 ms (point A in Fig. 5.4). This bubble then merges laterally with another bubble creating a bubble merger (BM). This merged bubble is then fed occasionally by smaller bubbles as it slides on the heater and departs from the surface at 363.76 ms. Points B through I

shown in Fig. 5.4. correspond to the nucleation of eight consecutive bubbles (B1 through B8). The main difference between B1 through B4 and B5 through B8 is related to vertical merger between bubbles. While no vertical merges observed between B5 through B8 (with the exception of 432.6 ms and 432.9 ms where B6 is being fed by another bubble during departure), there are three vertical mergers for B1 through B4. As it can be observed from Table 5.2, the maximum waiting time between the bubbles is 1.08 ms; the waiting time is not sufficient enough for the heat transfer to decay to the baseline. The heat transfer decays to the baseline after the last bubble departure (point J in Fig. 5.4).

The bubble heat transfer along with the images of each individual bubble for B5-B8 (last four bubbles with no vertical merges), are plotted in Figure 5.5 through 5.8. It should be noted that the time for each bubble was shifted so that t = 0 corresponds to the time of bubble nucleation for that bubble. Note that the bubble growth time for these bubbles (B5-B8) is approximately between 8 and 24 ms.

Starting from B5, an increase in the heat transfer is observed after nucleation as the contact area grows (0 ms to 5.94 ms); this increase is consistent with microlayer evaporation. The heat transfer then starts to decrease as the microlayer dries out and contact area increases (5.94 ms to 16 ms). From 16 ms to 23.49 ms (departure), the contact area shrinks and liquid rewets the heater surface, resulting in an increase in the heat transfer mostly due to transient conduction.

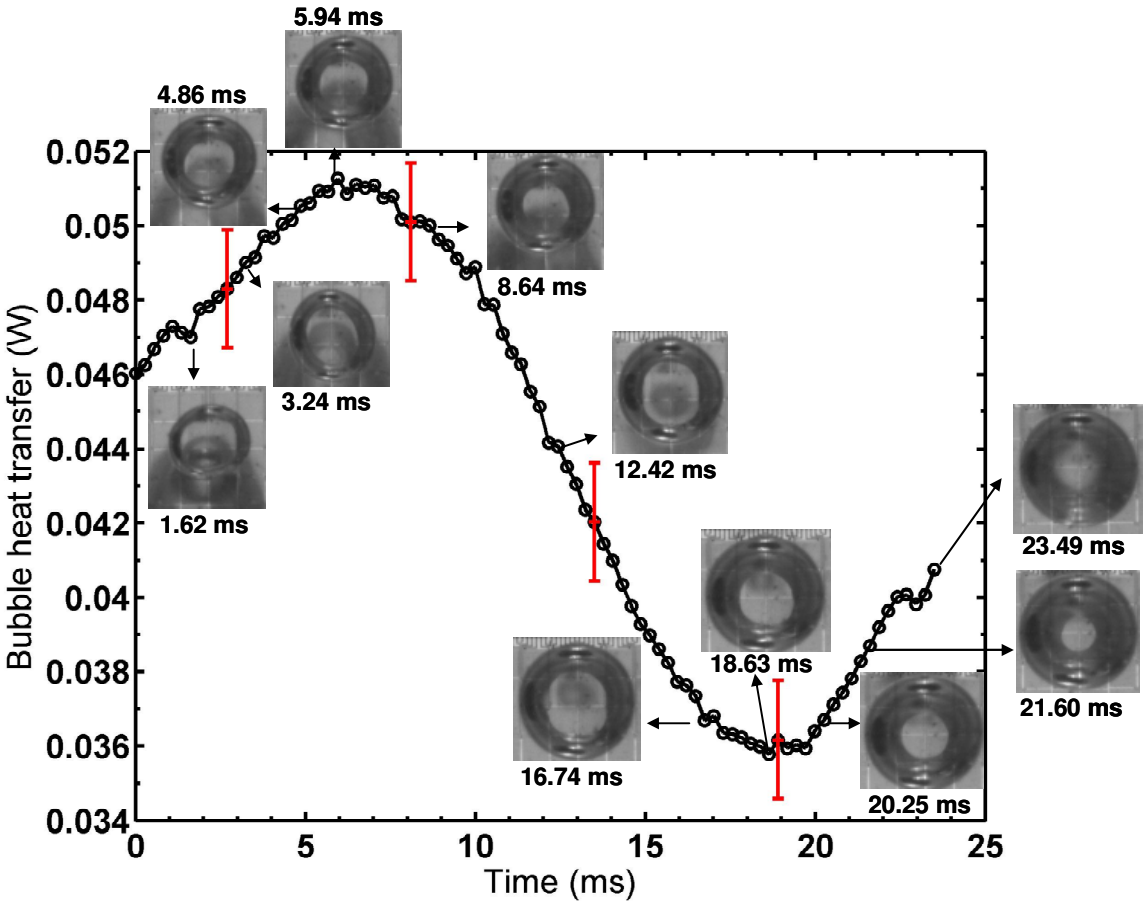

Figure 5.5. Bubble heat transfer for B5.

Heat transfer decreases during the initial growth of B6 (0<t<3.24 ms). This decrease in the heat transfer could be due to two possible reasons: (1) the microlayer has dried out; or (2) the heat transfer increase due to microlayer evaporation is not sufficient enough to dominate the heat transfer decay after the departure of B5. From 3.24 ms to 7.83 ms (departure), the contact area of B6 shrinks which again results in the heat transfer increase due to liquid rewetting.

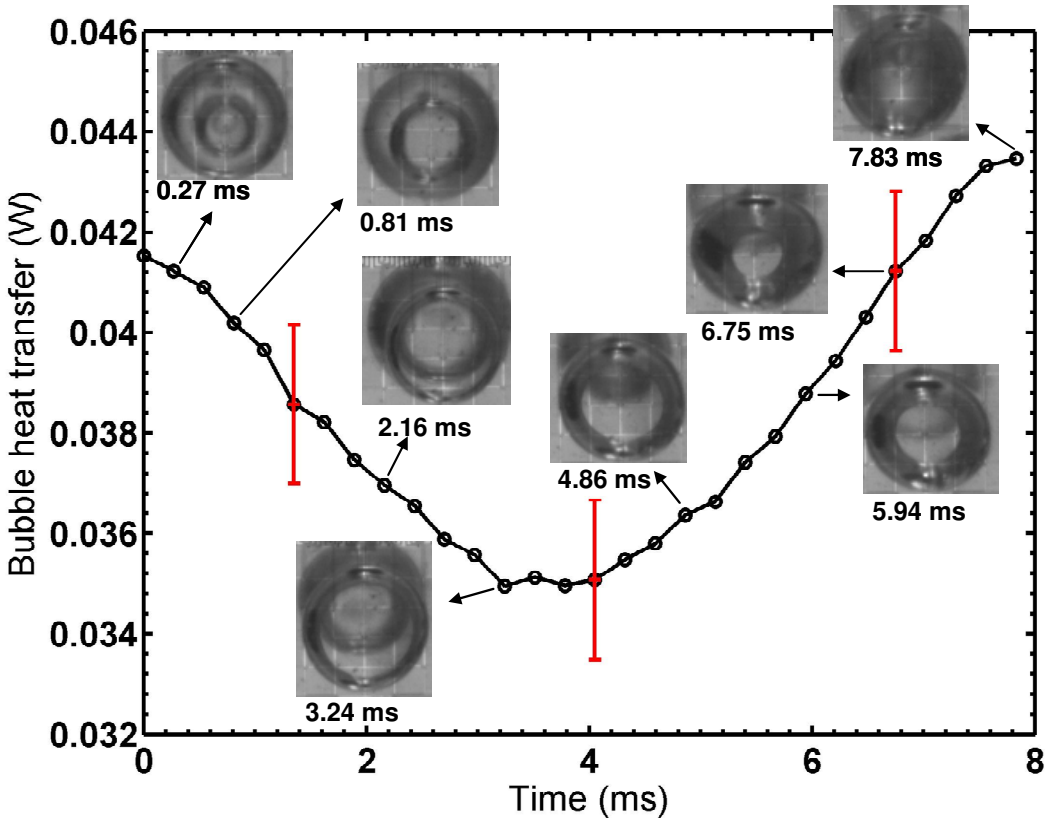

Figure 5.6. Bubble heat transfer for B6.

Heat transfer during the growth of B7 (between 0 ms<t<3.51 ms) seems to be constant. One possible explanation for this behavior is that the heat transfer decay due to transient conduction is being cancelled by the heat transfer increase due to microlayer evaporation. As the contact area decreases from 3.51 ms to 7.83 ms, heat transfer increases due to liquid rewetting.

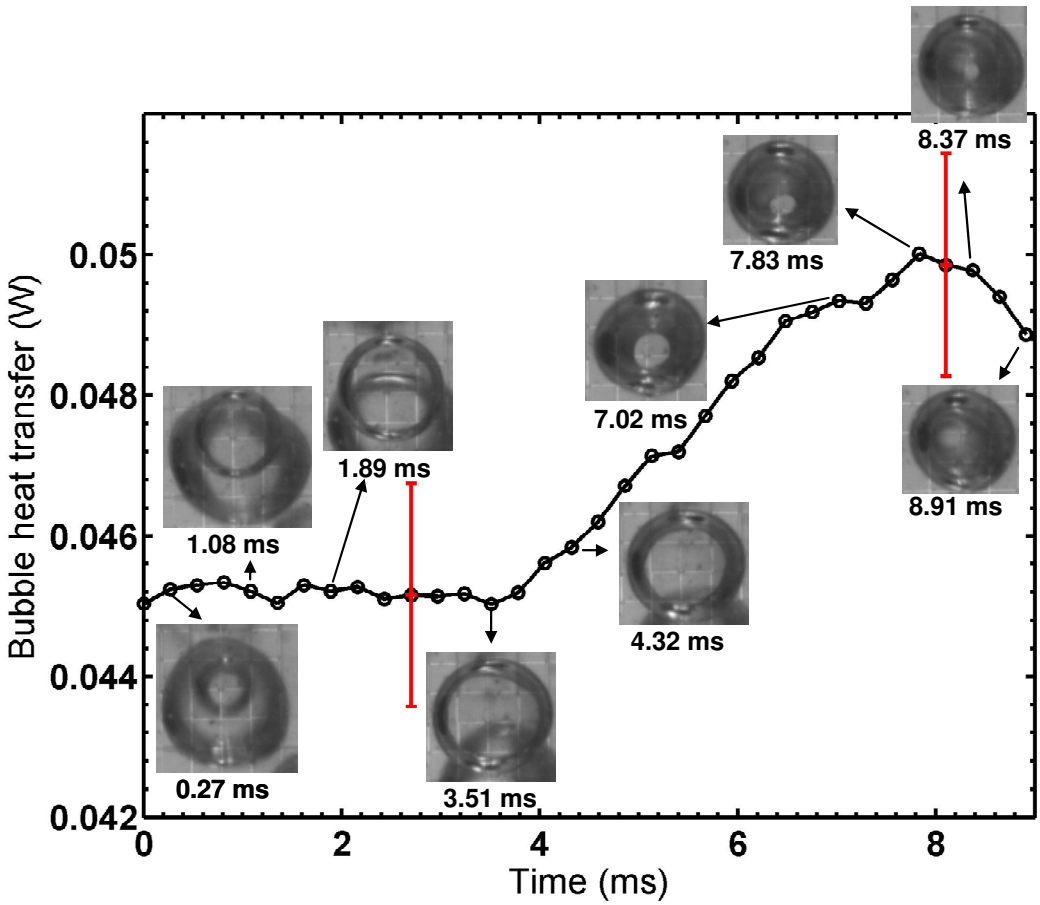

Figure 5.7. Bubble heat transfer for B7.

Heat transfer initially decreases during the growth of B8. This decrease in the heat transfer could again be due to two possible reasons: (1) the microlayer has dried out; or (2) the heat transfer increase due to microlayer evaporation is not sufficient enough to dominate the heat transfer decay after the departure of B7. Heat transfer increases from 4.05 ms to 8.10 ms as the contact area is shrinking (liquid rewetting). Heat transfer again decreases from 8.10 ms to 13.23 ms as the contact area is growing (microlayer dryout). As the contact area decreases from 13.23 ms to 22.14 ms, heat transfer increases again due to liquid rewetting. As it was mentioned above B8 is the last bubble on the surface; heat transfer decays to the baseline after B8 departs (24.03 ms).

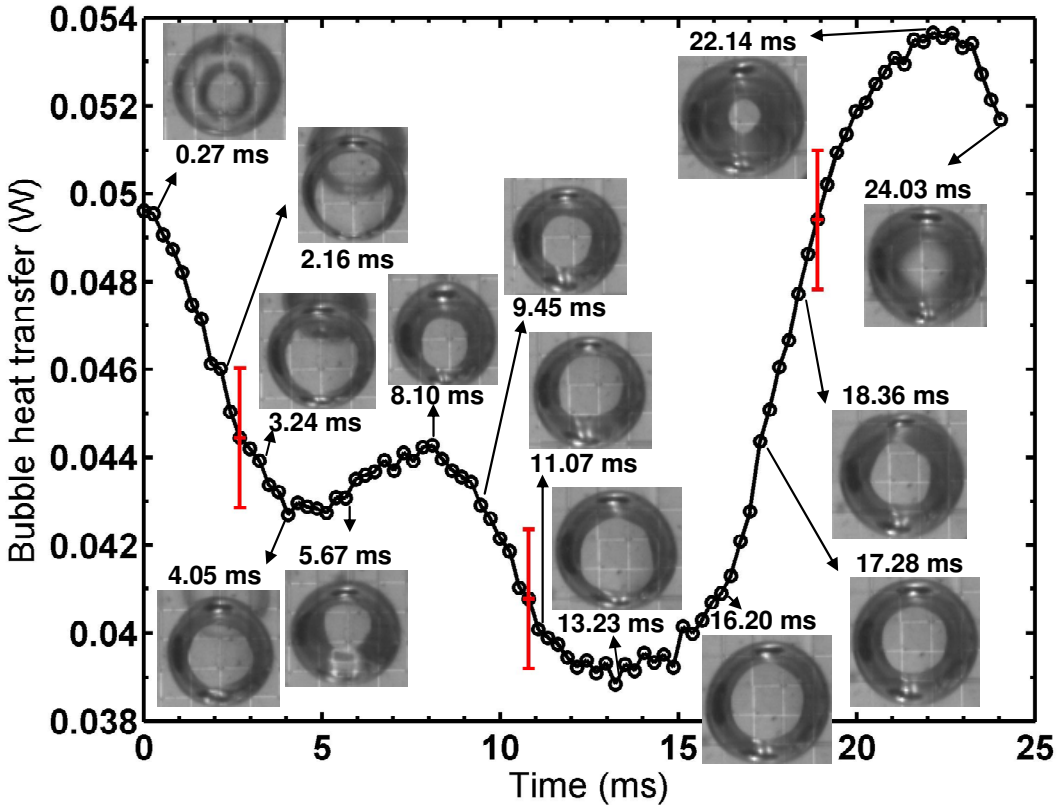

Figure 5.8. Bubble heat transfer for B8.

5.2.2. Equivalent and Physical Bubble Diameter

The wall heat transfer data can be used to compute an equivalent bubble diameter (d_{eq}) by assuming that all the heat transferred from the heaters in the selected region goes into latent heat, Eq. 5.1.

$$\rho_v \frac{\pi d_{eq}^3(t)}{6} h_{lv} = \int_0^t \dot{q}_h''(t) A_h dt \tag{5.1}$$

where time t = 0 is assumed to be the start of nucleation for a single bubble. This results in an overestimation for the value of d_{eq}. The measured (physical) volume of the bubble was calculated based on the assumption that the embryo shape is a portion of a sphere (Fig. 5.9). Inner ring diameter d_{in} and outer ring diameter d_{out} was measured from the bottom view images. The bubble volume V_v is given by Eq. 5.2.

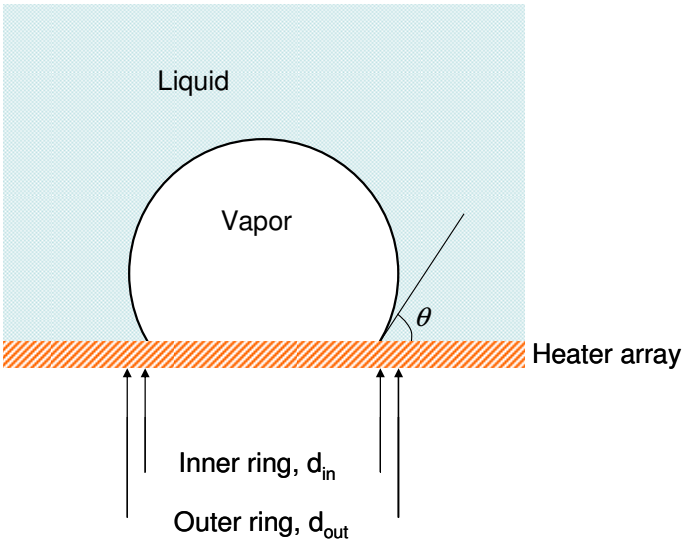

Figure 5.9. Sketch of an embryo vapor bubble formed on the heater array (side view)

$$V_v = \frac{\pi r^3}{3}(2 + 3\cos\theta - \cos^3\theta) \tag{5.2}$$

where

$$\sin\theta = \frac{d_{in}}{d_{out}}$$

$$r = \frac{d_{out}}{2}$$

The bubble volume was then used to calculate the physical diameter of a sphere of the same volume with diameter d using Eq. 5.3:

$$V_v = \frac{\pi d^3}{6} \tag{5.3}$$

The equivalent diameter is plotted along with the physical diameter in Fig. 5.10 for B5-B8 (last four bubbles). It is seen that d_{eq} is significantly smaller than the physical bubble diameter during the bubble growth time, indicating that the heat transfer from the wall cannot account for the bubble growth alone. For example, the physical diameter of B5 at 1.62 ms is 0.74 mm while the equivalent diameter is 0.54 mm at this time. The ratio of equivalent volume to physical volume is a measure of heat transferred from the wall. The wall heat transfer could have contributed at most $0.54^3/0.74^3$ or 39 % of the energy required to produce the bubble. This value is an overestimate since the equivalent volume was calculated using all the heaters in the selected region and not just within the bubble contact area. The bubble must have gained the rest of its energy from the superheated liquid layer surrounding the bubble. The superheated liquid layer thus acts as a reservoir of energy which the bubble draws upon during its growth. This conclusion is consistent with the results of the recent experimental studies discussed in the Literature Review chapter.

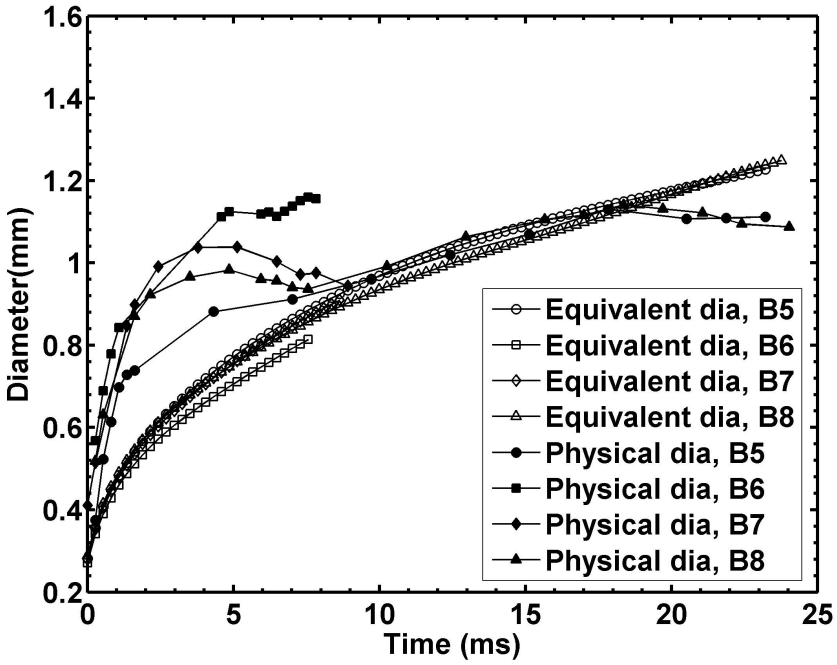

Figure 5.10. Comparison of physical and equivalent bubble diameters.

5.2.3. Heat Transfer Variation for a Single Heater

An example of the heat transfer variation with time for a single heater (heater 35) is shown in Fig. 5.11. An approximate baseline curve was obtained by applying a linear interpolation between closely spaced points that follow the general trend of the baseline heat transfer (Fig. 5.12). Bubble heat transfer was obtained by subtracting the baseline from the total heat transfer. The nominal temperature for this heater and those surrounding it is 56 °C. The uncertainty associated with heater 35 is lower than the heaters on the edge of the array (e.g. heater 31) and heaters that have different temperatures compared to their surrounding heaters (e.g. heater 33). An interesting trend that can be observed in Fig. 5.11 is that the heat transfer increase is considerably smaller when the contact area is receding than when it is advancing. This trend can be observed for other heaters as well. This indicates that microlayer evaporation is not the dominant

heat transfer mechanism since the contribution of the microlayer evaporation should be higher during the receding phase and lower in the advancing phase (see the modeling section).

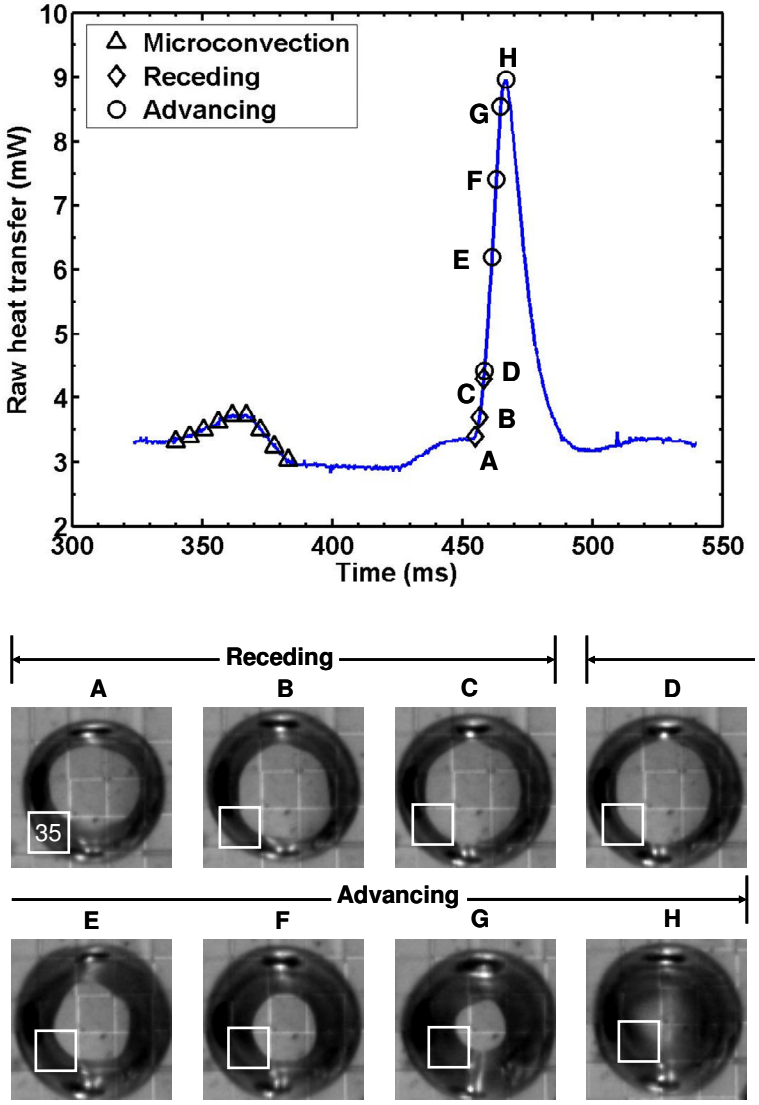

Figure 5.11. Heater 35 raw (total) heat transfer with bubble images at different times.

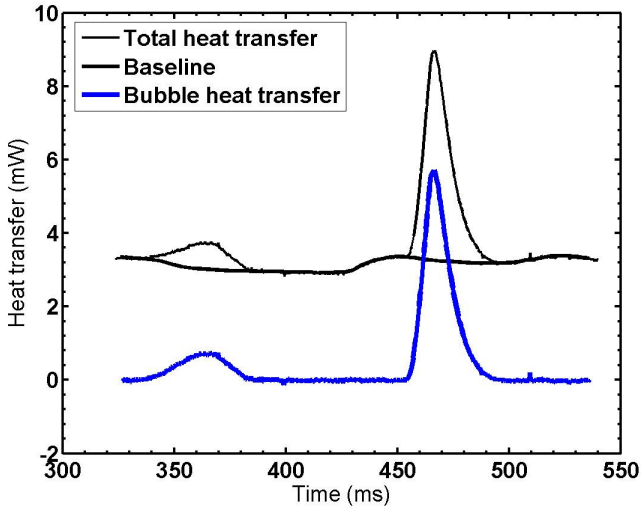

Figure 5.12. Bubble heat transfer calculation for heater 35.

5.2.4. Bubble Heat Transfer for a Line of Heaters

An example of the heat transfer variation, during growth and departure of B1, for a line of heaters (heater 43, 33, and 23) along with bubble images is shown in Fig. 5.13. Contact line movement occurs on heater 43 and 33. Heater 43's heat transfer increase from A to B is a result of microlayer evaporation and/or contact line evaporation. Heat transfer then decreases from B to D consistent with drying of the microlayer. Finally, heat transfer increases from D to F as the advancing liquid front rewets the heater. Heat transfer increases monotonically for heater 33 as the contact line recedes and advances suggesting that the microlayer is not completely drying on this heater. The contact line does not reach heater 23 and there is a minimal heat transfer increase due to microconvection. It should be noted that the negative values of heat transfer observed for heater 33 and 23 are within the experimental uncertainty and are due to variations in the baseline heat transfer.

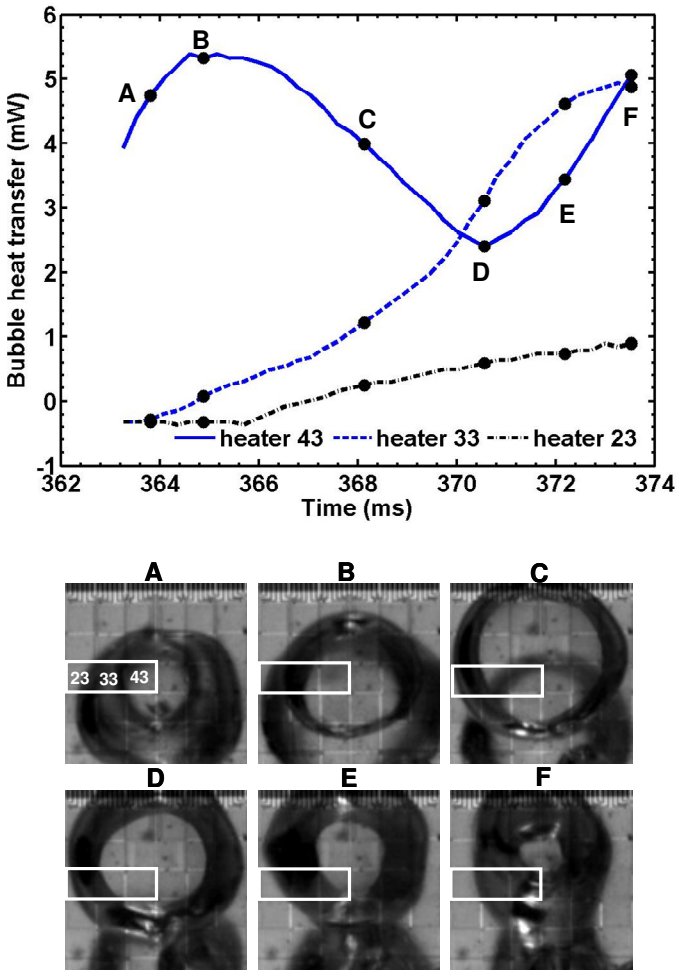

Figure 5.13. Bubble heat transfer for a line of heaters.

5.2.5. Conclusions Regarding Single Bubbles with Minimal Waiting Time

The single bubbles having growth times between 8 ms and 24 ms and maximum waiting time of 1.08 ms gained the majority of their energy from the superheated liquid layer and not from the wall, indicating that microlayer and contact line heat transfer are not the dominant heat transfer mechanisms. Experimental results for individual heaters also indicated that transient conduction and/or microconvection is the dominant heat transfer mechanism.

5.3. Sequence of Single Bubbles with Considerable Waiting Time

The objective of this experiment was to investigate the heat transfer behavior related to the sequence of single bubbles with considerable waiting time. This was achieved by changing the combination of heater temperature and chamber pressure to generate the required superheat to create single bubbles. The test conditions are provided in Table 5.3.

Table 5.3. Test conditions for sequence of bubbles with considerable waiting time.

Pressure (atm)	1.02
T_w (°C)	48
T_{sat} (°C)	36.6
T_{bulk} (°C)	32.3
Superheat (°C)	11.4
Subcooling (°C)	4.3
Jakob Number	15.2
Air jet	OFF

Note: The heater was set to higher temperatures (about 90 °C) to initiate boiling.

Nucleation and departure times for the first three bubbles are provided in Table 5.4. Nucleation was very regular for this experiment. The bubble growth and waiting time (for the first three bubbles) was 4.3 ms and 10.8 ms, respectively. Subsequent bubbles in this experiment appeared to follow the same trend. The selected region for this experiment is outlined in Fig. 5.14. This region was selected such that it completely covers the movement of the apparent contact area on the heater.

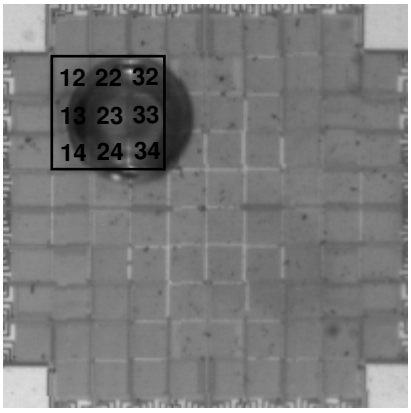

Figure 5.14. Selected region on the heater.

Table 5.4. Nucleation and departure times for the sequence of bubbles

Description	Nucleation time (ms)	Departure time (ms)	Waiting time (ms)	Growth time (ms)
Bubble 1 (B1)	1.9	6.2	10.8	4.3
Bubble 2 (B2)	17.0	21.3	10.8	4.3
Bubble 3 (B3)	32.1	36.5	10.8	4.3

5.3.1. Determination of the Baseline Heat Transfer

To quantify the amount of heat transfer associated with boiling, a secondary experimental run was performed to evaluate the baseline heat transfer. The baseline heat transfer was obtained by setting the heater to 48 °C without initiating boiling by originally setting the heater at higher temperatures. High speed images were also obtained for the baseline data to confirm that no bubble was formed on the heater. It should be mentioned that all other conditions were unchanged for the secondary (baseline) run.

The instantaneous baseline heat transfer for each heater was averaged over the data collection time (2 seconds) to calculate a time averaged baseline heat transfer. An example of the instantaneous baseline heat transfer variation along with the time

averaged value is plotted in Fig. 5.15 for heater 23. The time averaged baseline heat transfer for each heater was subtracted from the raw data to calculate the bubble heat transfer.

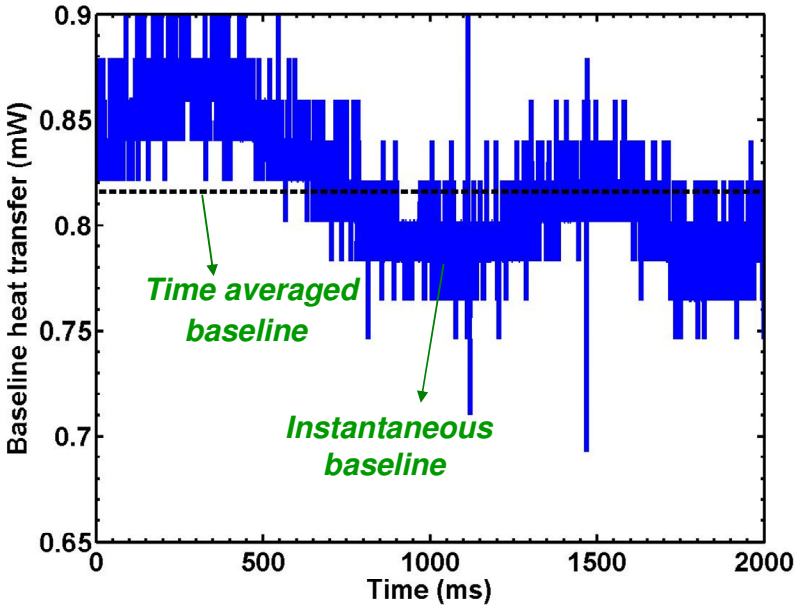

Figure 5.15. Baseline heat transfer for heater 23.

The instantaneous baseline heat transfer for the entire selected region was found by summing the instantaneous baseline from individual heaters for each time step. The resulting instantaneous baseline was then averaged over the data collection time (2 seconds) to calculate a time averaged baseline heat transfer for the selected region (Fig. 5.16). Note that the variations in the baseline heat transfer for the selected region (9 heaters) could be as large as 0.5 mW.

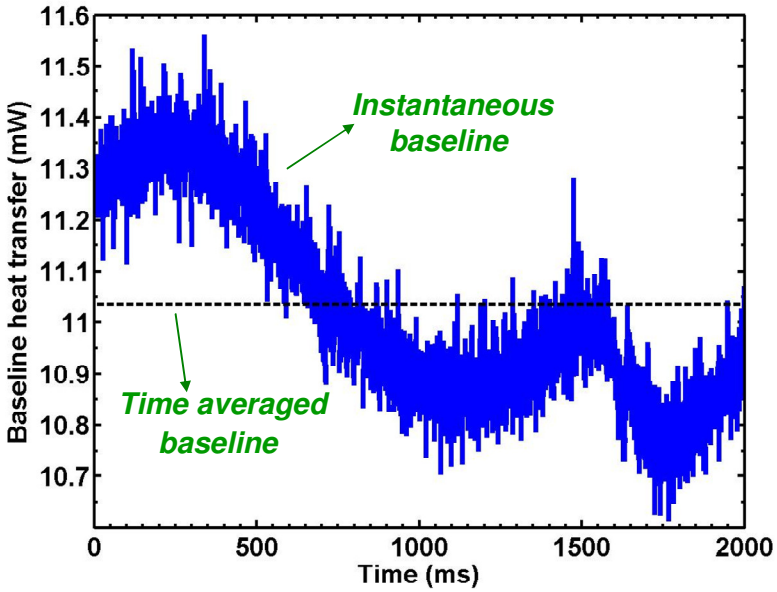

Figure 5.16. Baseline heat transfer variation for the selected region.

5.3.2. Bubble Heat Transfer from the Selected Region

Bubble heat transfer for a selected time period (about 80 ms) as well as bubble images at various times are given in Fig. 5.17. Note that the bubble images often contain blurry outlines of previously departed bubbles; B0 is the bubble that has departed prior to B1's nucleation. Heat transfer increases significantly as B1 nucleates and grows on the selected region (A-C), consistent with microlayer evaporation and contact line heat transfer. It should be noted that heat transfer increases starting at point A indicating the actual nucleation for B1 probably occurs at A and not B (inability of the camera in capturing the image). Heat transfer continues to increase as the heater is being rewetted until the departure at point E. This heat transfer increase is due to transient conduction and/or microconvection. Residual microlayer evaporation could contribute to bubble heat transfer in this period as well. Heat transfer decreases shortly after bubble departure as

the thermal boundary layer grows on the heater. This cycle is repeated for the subsequent bubbles.

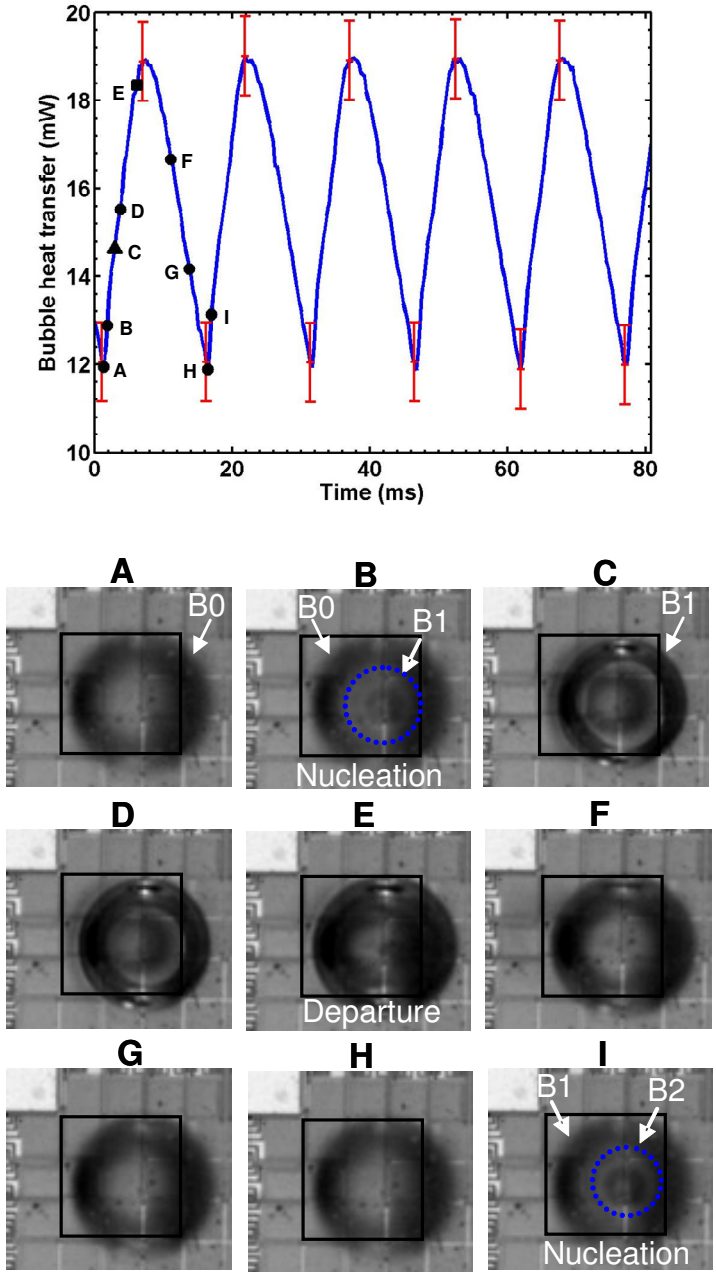

Figure 5.17. Bubble heat transfer with bubble images at different times.

5.3.3. Effect of Increasing the Size of the Selected Region

In order to investigate the contribution of microconvection, the size of the selected region was increased from 9 heaters to 16 heaters. As indicated in Fig. 5.18, the heaters outside the apparent contact area do not appear to have a considerable contribution to the total heat transfer suggesting that microconvection outside the contact area is not significant.

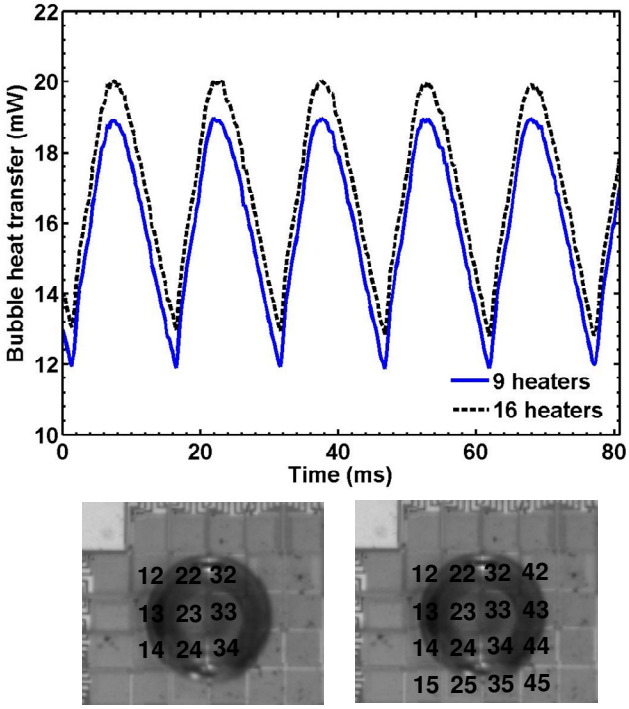

Figure 5.18. Effect of increasing the size of the selected region.

5.3.4. Heat Transfer Variation for a Sample Heater

An example of bubble heat transfer variation for the same period of time used in Section 5.3.2 along with bubble images for heater 23 is shown in Fig. 5.19. The same heat transfer trends observed for the selected region was observed for this heater as well. This trend can also be found in the other heaters (e.g. heater 22) affected by the contact area movement.

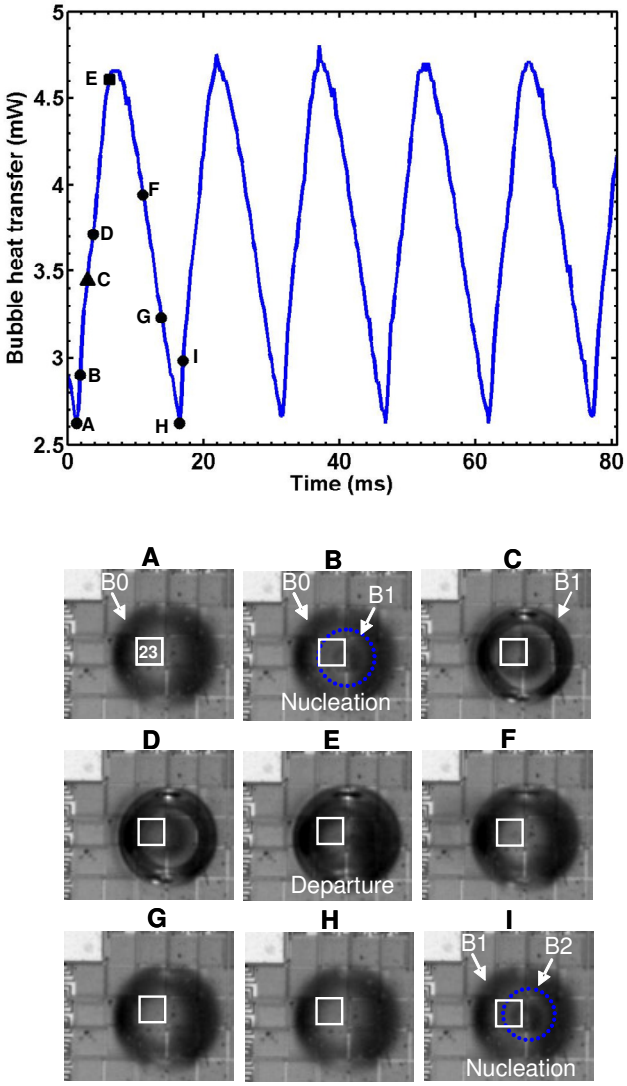

Figure 5.19. Bubble heat transfer variation for heater 23 with bubble images at different times.

5.3.5. Equivalent and Physical Bubble Diameter

The wall heat transfer data can be used to compute an equivalent bubble diameter (introduced in section 5.2.2.). In order to investigate the contribution of the various heat transfer mechanisms, the equivalent diameter for Bubble 1 (B1) is plotted along with the physical diameter in Fig. 5.20. As expected, the equivalent diameter calculated from 9 heaters is sufficiently close to the one calculated from 16 heaters.

Similar to the previous experiment (Section 5.2), the physical diameter is observed to be significantly larger than equivalent diameter indicating that the superheated liquid layer is the major source of the energy for the bubble. It should be noted that data was very repeatable for this experiment so only a representative bubble (B1) was selected for the purpose of comparison. The physical diameter of B1 at 1.35 ms is 0.90 mm while the equivalent diameter is 0.32 mm at this time. The ratio of equivalent volume to physical volume is a measure of heat transferred from the wall. The wall heat transfer could have contributed at most $0.32^3/0.90^3$ or 4.5 % of the energy required to produce the bubble.

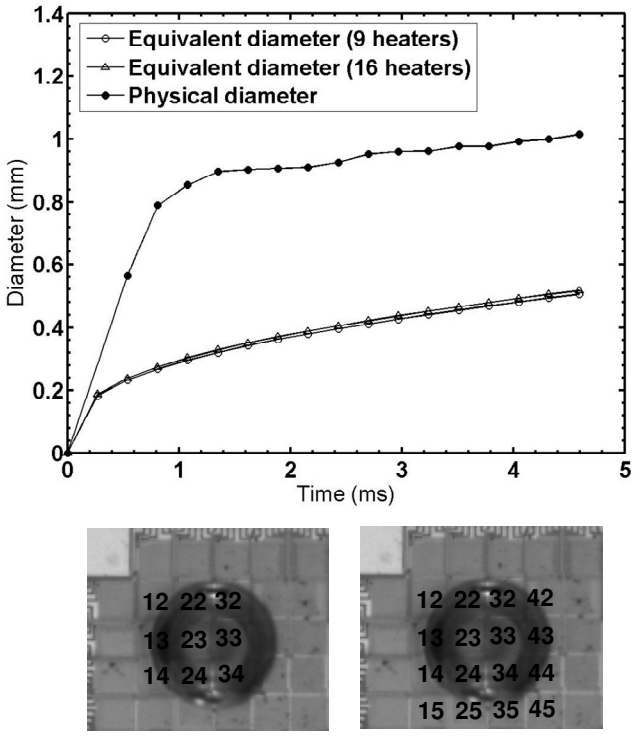

Figure 5.20. Comparison of physical and equivalent bubble diameters

5.3.6. Conclusions Regarding Single Bubbles with Considerable Waiting Time

Single bubbles with growth and waiting times of 4.3 and 10.8 ms respectively gained the majority of their energy from the superheated liquid layer and not from the wall, indicating that microlayer and contact line heat transfer are not the dominant heat transfer mechanisms.

5.4. Pressure Effects on Single Bubbles Behavior

The objective of this study was to investigate the heat transfer behavior related to the single bubbles at higher pressures. A summary of the test conditions for these experiments, denoted by run A and B, are provided in Tables 5.5. The selected region on the heater for these experiments were the same as the one outlined in Fig. 5.14. It should be noted that the bubble dynamics at higher pressures were quite different from lower pressures; generally higher growth time was observed (about 78 ms for 1.34 atm and 116 ms for 1.5 atm).

Table 5.5. Test conditions for run A and B.

Run	A	B
Pressure (atm)	1.34	1.5
T_w (°C)	54	56
T_{sat} (°C)	44.9	48.4
T_{bulk} (°C)	41.9	41.5
Superheat (°C)	9.1	7.6
Subcooling (°C)	3	6.9
Jakob Number	9.6	7.3
Air jet	ON	ON

Note: The heater was set to higher temperatures (about 90 °C) to initiate boiling.

5.4.1. Determination of the Baseline Heat Transfer

The baseline heat transfer was measured through a secondary experiment similar to the one discussed in the previous section (5.3). The instantaneous baseline heat transfer data obtained for each heater was averaged over the data collection time (2 seconds) to calculate a time averaged baseline heat transfer. The time averaged baseline for each heater was subtracted from the raw boiling data to calculate the bubble heat transfer.

The instantaneous baseline heat transfer variations along with the time averaged values are plotted for a sample heater (# 23) in Figs. 5.21 and 5.22 for Run A and Run B.

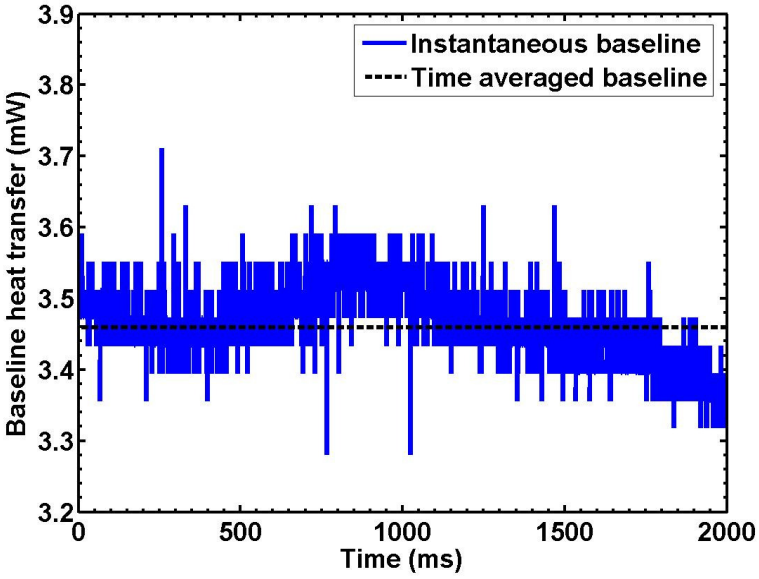

Figure 5.21. Run A baseline heat transfer for heater 23.

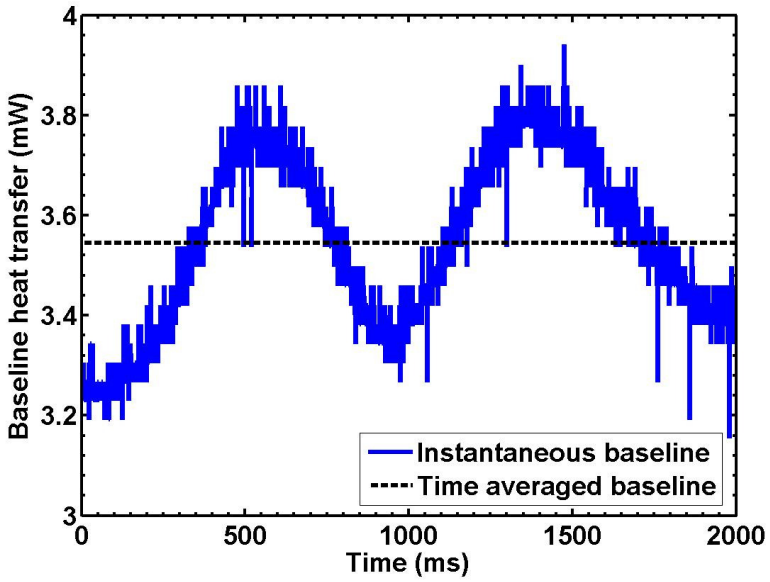

Figure 5.22. Run B baseline heat transfer for heater 23.

The same method discussed in section 5.3 was used to calculate the instantaneous and time averaged baselines for the entire selected region (Figs 5.23 and 5.24). Note that the variations in the baseline heat transfer for the selected region (9 heaters) could be as large as 1.2 mW.

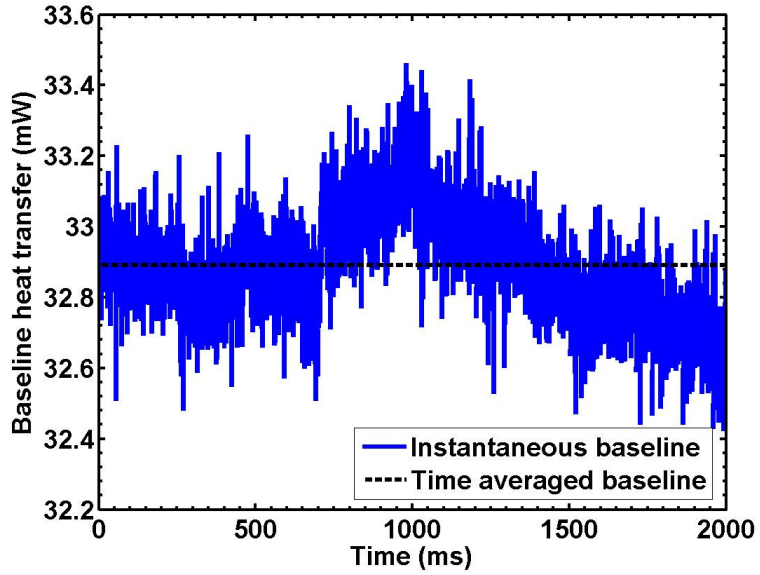

Figure 5.23. Baseline heat transfer for the selected region (Run A).

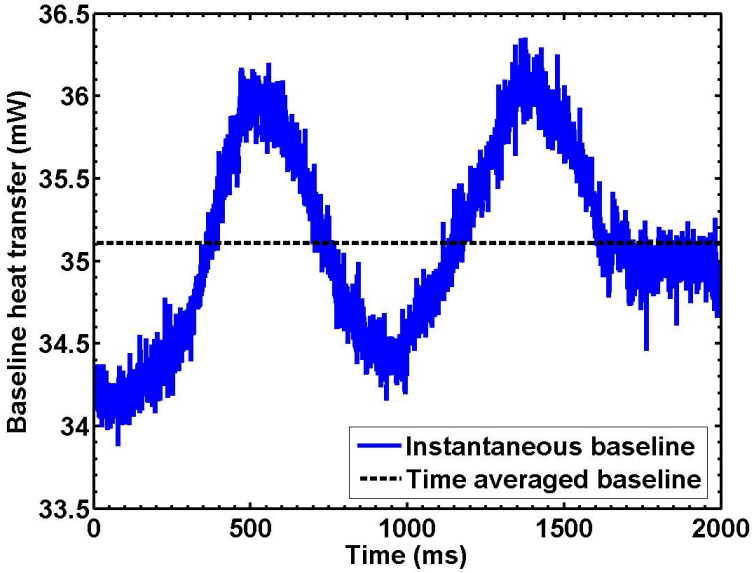

Figure 5.24. Baseline heat transfer for the selected region (Run B).

5.4.2. Heat Transfer from the Selected Region

Bubble heat transfer for the selected region was obtained by summing the bubble heat transfer from each heater in that region (9 heaters). Bubble heat transfer for a selected period of time during Run A is given in Fig. 5.25. A sample of the heat transfer variation from nucleation to departure for a selected bubble (marked in Fig. 5.25) from this experiment will be closely investigated below.

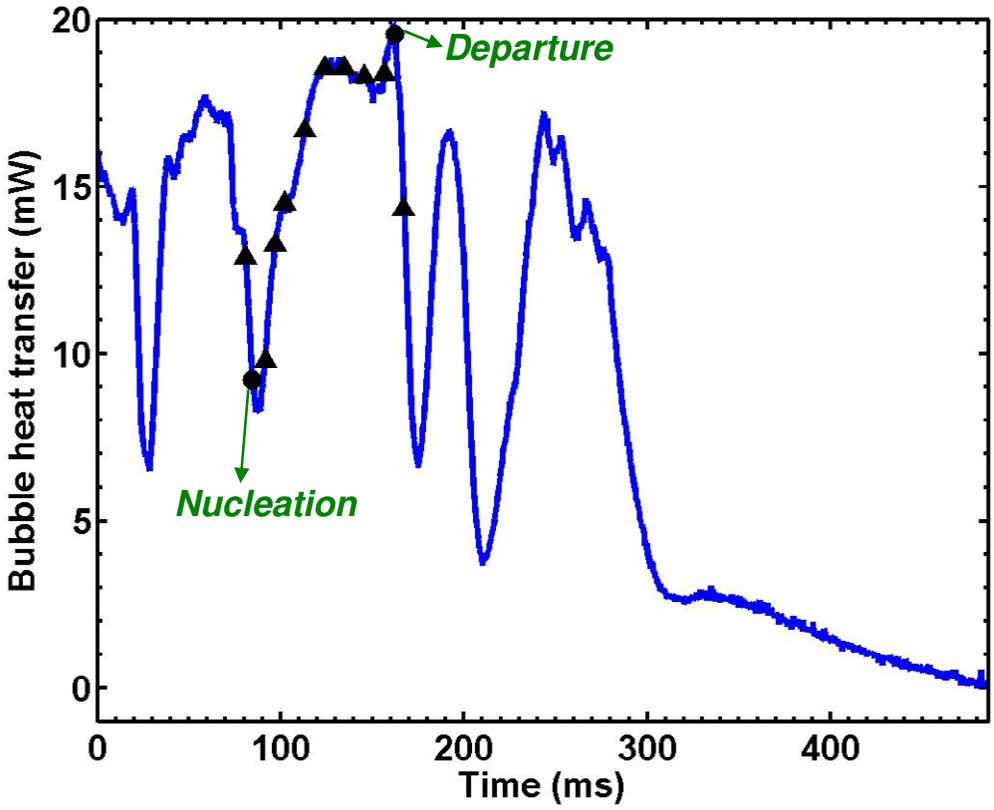

Figure 5.25. Total heat transfer for the selected region (Run A).

A close-up view of bubble heat transfer from nucleation to departure along with bubble images at various times is given in Fig. 5.26. The blue circle in the image at point B marks the bubble contact area on the heater.

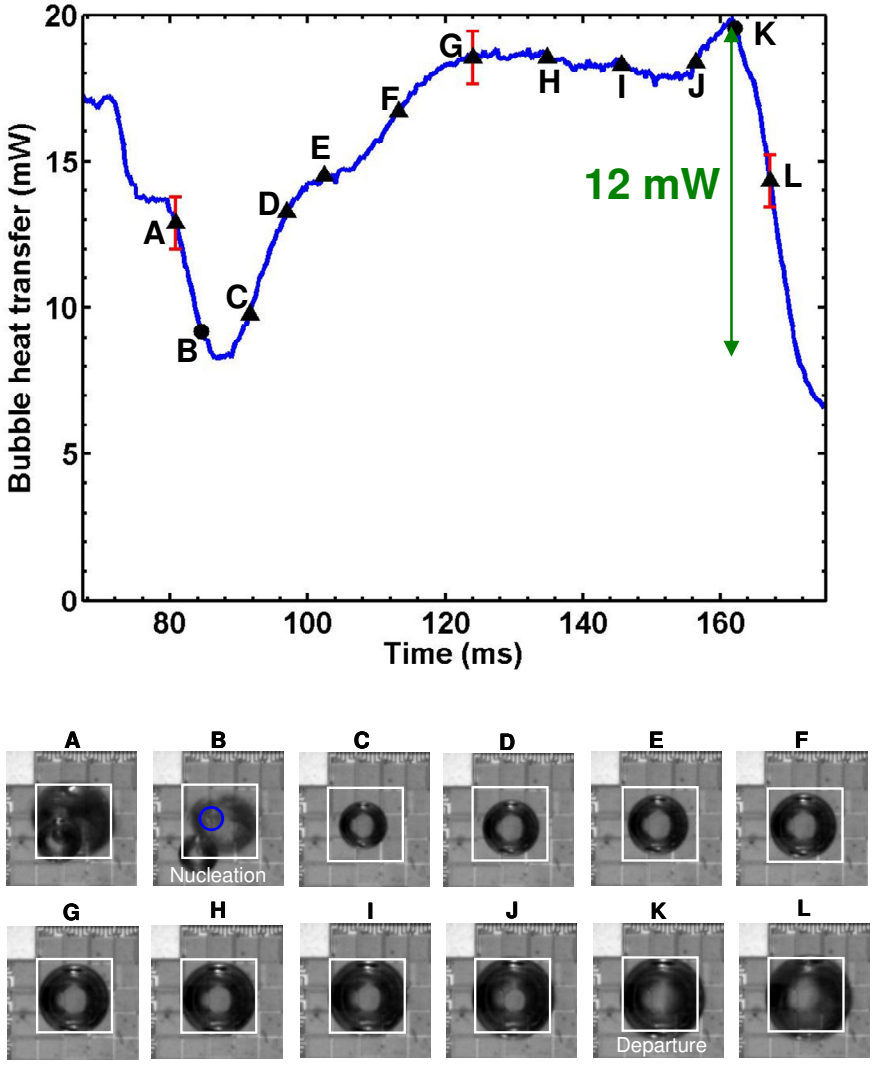

Figure 5.26. A close-up view of bubble heat transfer from the selected region along with bubble images at different times (9 heaters).

5.4.3. Heat Transfer Variation for Selected Heaters

Figure 5.27 depicts the heaters with significant heat transfer excursions above the baseline within the selected region. Heat transfer variation for these heaters will be discussed below.

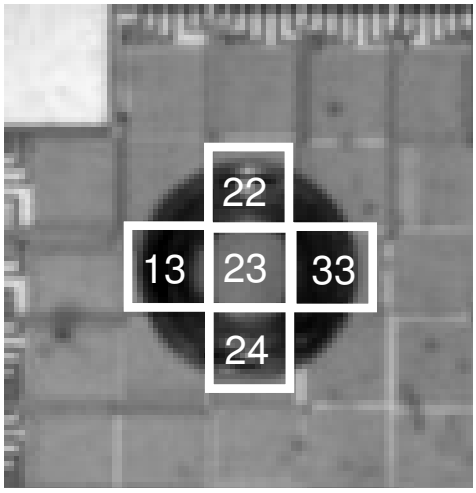

Figure 5.27. Heaters in the selected region with considerable bubble heat transfer.

Heat transfer variation for heater 13 is given in Fig. 5.28. The three-phase contact line slightly moves on the heater from B to J. The observed heat transfer trend is likely due to microlayer and/or contact line evaporation. It should be noted that the contact area movement is minimal for this heater; microconvection could be responsible for the observed heat transfer trend. Heat transfer decreases from J to K as the contact area has already moved from the heater (decrease in the transient conduction). Heat transfer then increases from K to L probably due to transient convection after the bubble departure.

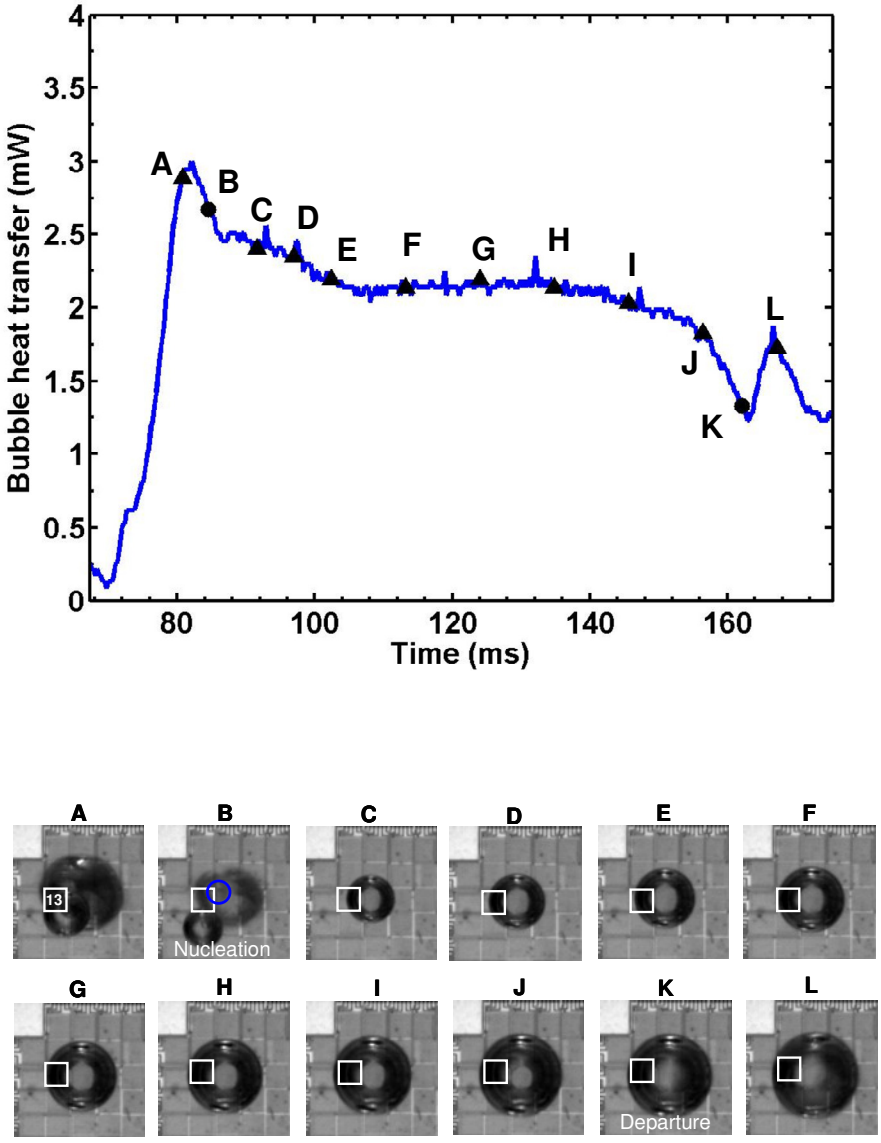

Figure 5.28. Bubble heat transfer with bubble images at different times (heater 13).

Heat transfer variation for heater 22 is given in Fig. 5.29. The area affected by the contact area movement is minimal for this heater; microconvection is probably the responsible heat transfer mechanism for the heat transfer variation B to K. Heat transfer slightly increases after the departure (K) due to transient convection.

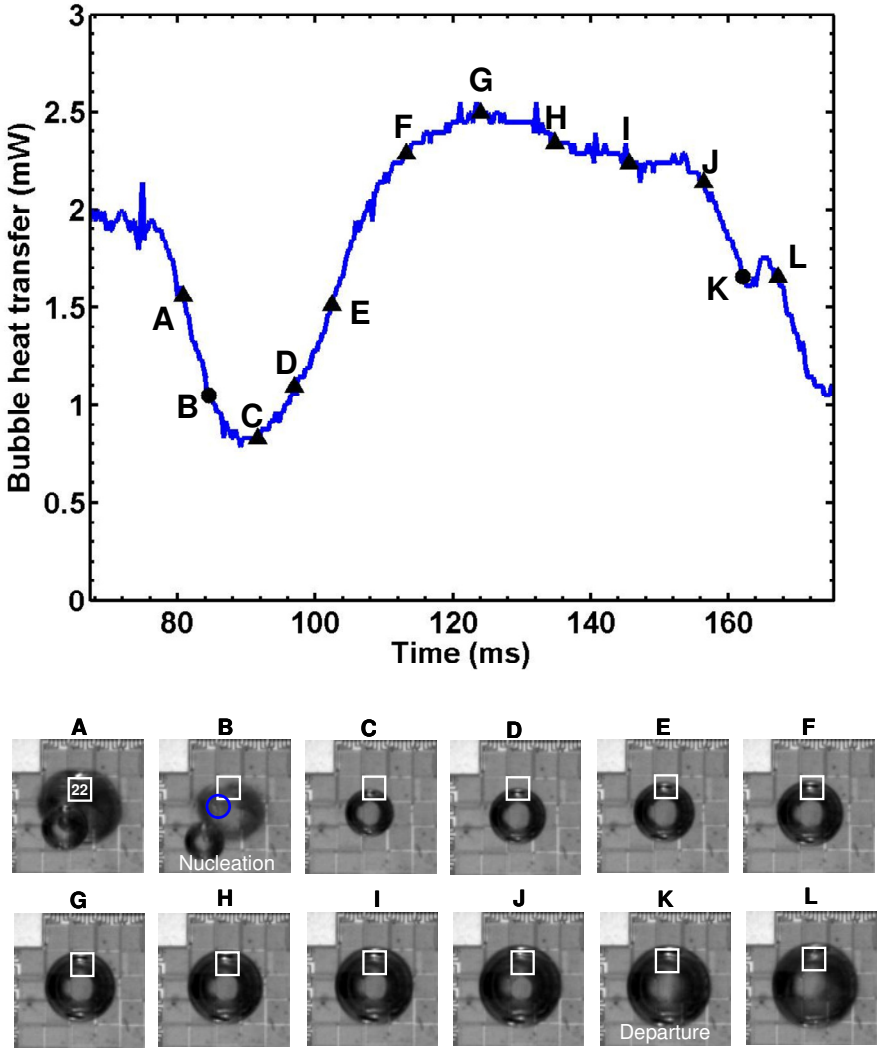

Figure 5.29. Bubble heat transfer with bubble images at different times (heater 22).

Heat transfer variation for heater 23 is given in Fig. 5.30. Heat transfer increases significantly as the contact area grows on the heater. This increase is due to microlayer and/or contact line evaporation. Heat transfer is relatively constant from E to J as the three-phase contact line stays on the heater. Microlayer and/or contact line evaporation are the contributing heat transfer mechanisms in this period. Rewetting of the heater occurs from J to K resulting in the heat transfer increase due to transient conduction into

the liquid. The heat transfer increase from B to K is about 9 mW; consequently, the contribution from heater 23 is significant.

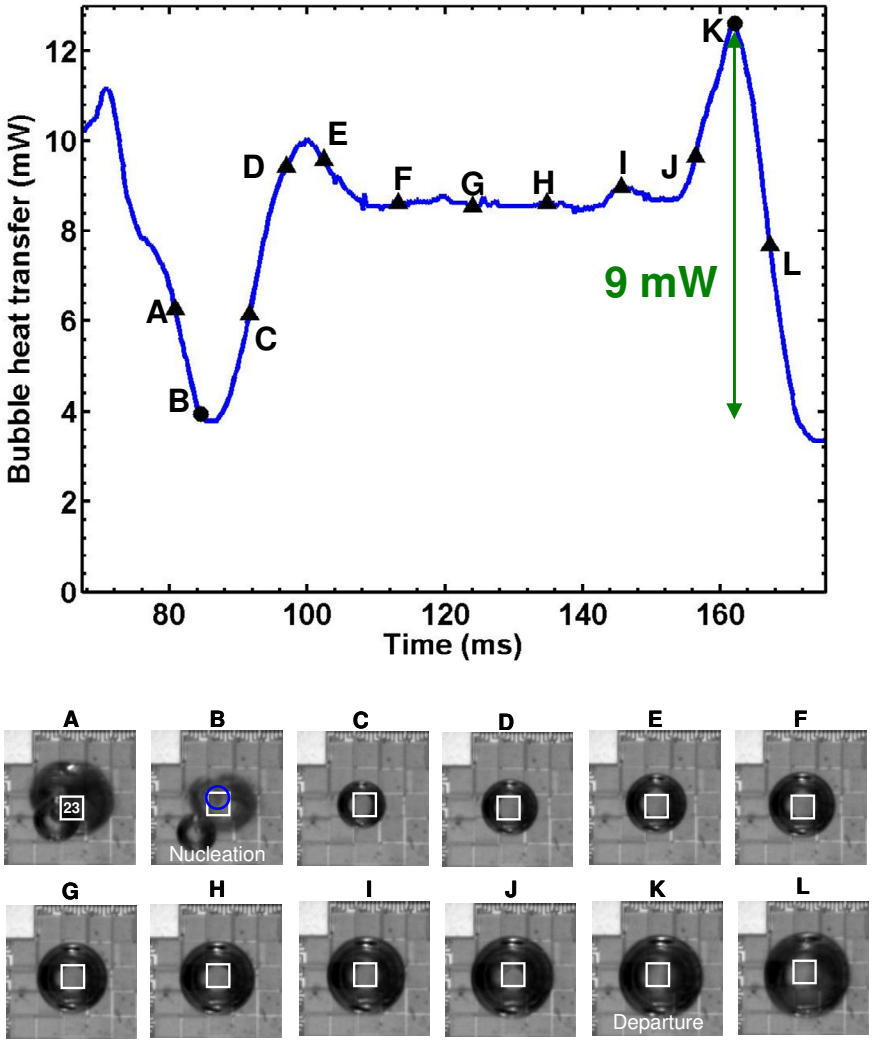

Figure 5.30. Bubble heat transfer with bubble images at different times (heater 23).

Heat transfer variation for heaters 24 and 33 are given in Figs. 5.31 and 5.32 respectively. The contact area movement is almost negligible for these heaters; microconvection is probably the responsible heat transfer mechanism for the heat transfer

variation B to K. Transient convection was not observed for these heaters; heat transfer decreases for these heaters after the bubble departure (K).

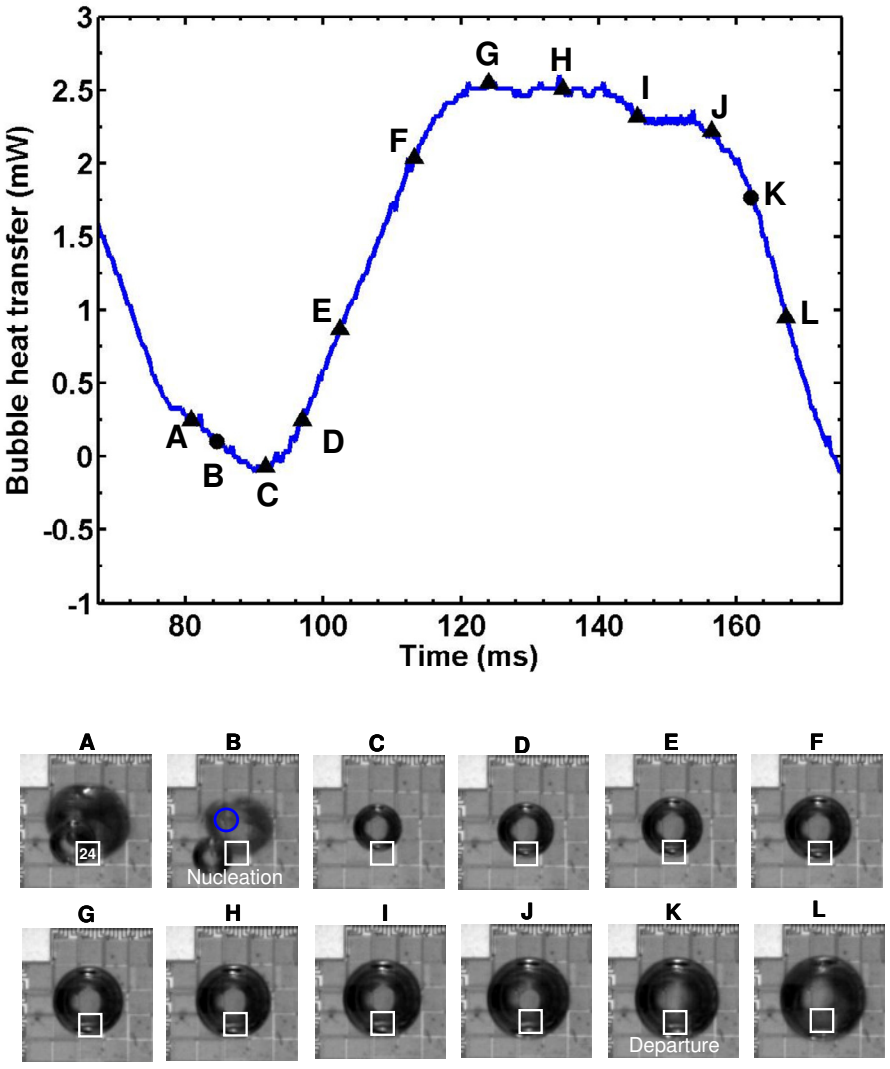

Figure 5.31. Heat transfer with bubble images at different times (heater 24).

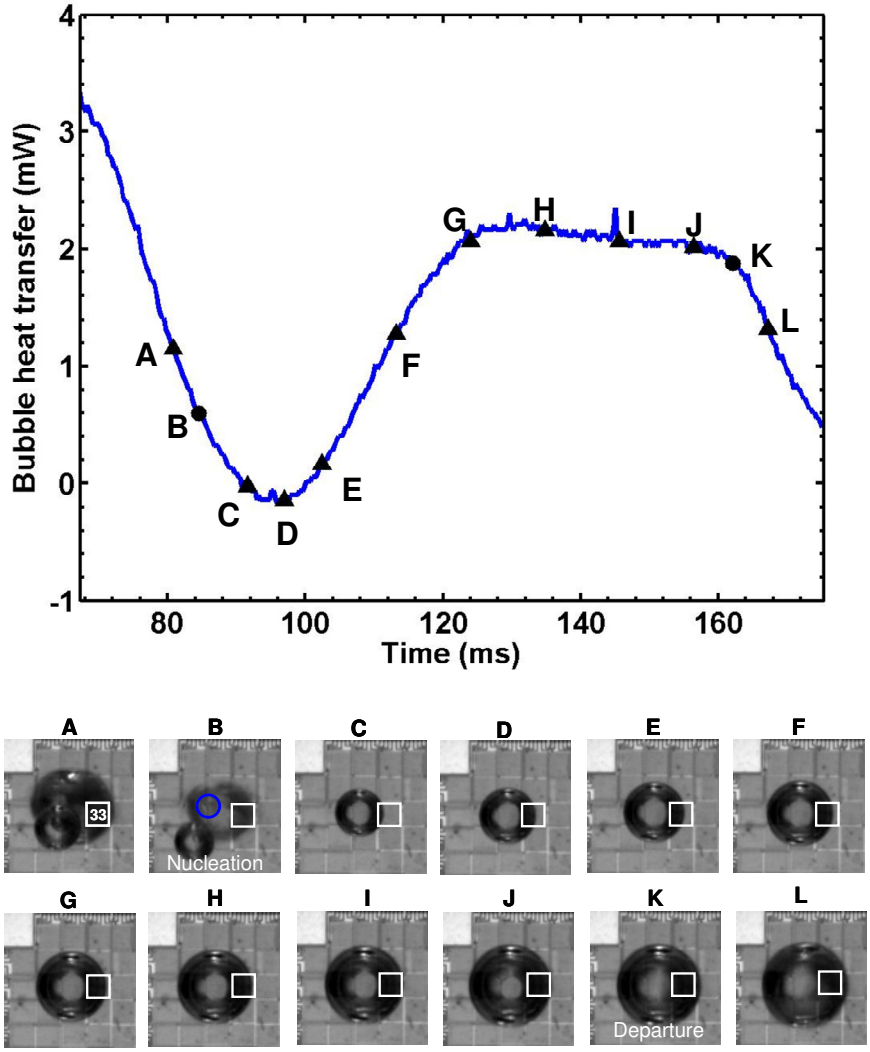

Figure 5.32. Heat transfer with bubble images at different times (heater 33).

5.4.4. Equivalent and Physical Bubble Diameter

The equivalent and physical diameters for the higher pressure cases were calculated. The equivalent diameter is plotted along with the physical diameter for two selected bubbles from Run A and Run B in Figs. 5.33 and 5.34.

Interestingly, the physical diameter is not significantly larger than the equivalent diameter for these cases; the physical diameter is actually smaller than the equivalent

diameter after the initial bubble growth (probably due to condensation at the bubble cap) in contradiction to what was observed for bubbles with lower growth time (less than 24 ms). The fact that the physical diameter is not larger than the equivalent diameter for bubbles with higher growth time indicates that microlayer and/or contact line evaporation have significant contribution to the total heat transfer. This trend will be further explored by investigating the heat transfer behaviors for various heaters affected by the contact line movement.

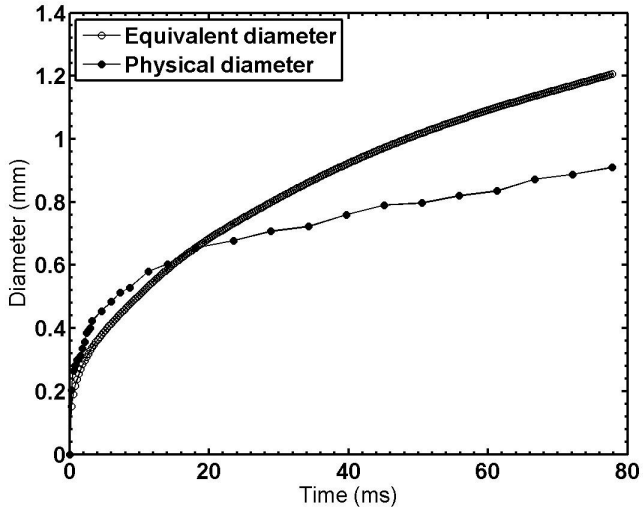

Figure 5.33. Comparison of physical and equivalent bubble diameters for a selected bubble in Run A

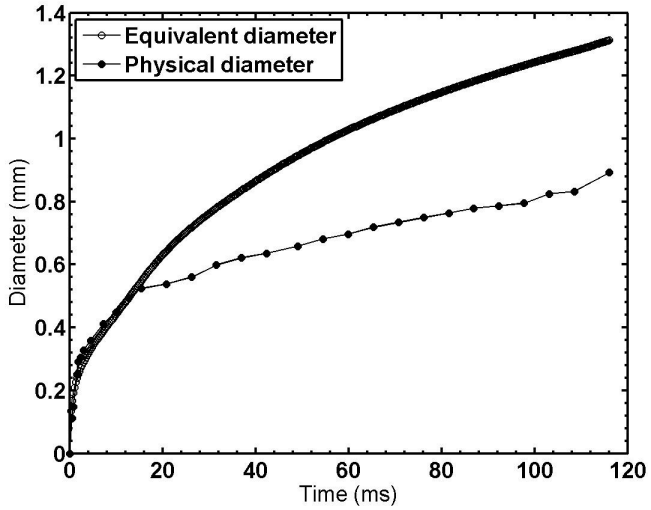

Figure 5.34. Comparison of physical and equivalent bubble diameters for a selected bubble in Run B

5.4.5. Conclusions Regarding Nucleating Bubbles at Higher Pressures

Single bubbles with growth time of 78 and 116 ms gained the majority of their energy from the instantaneous heat from the wall and not from the superheated liquid layer indicating that microlayer and contact line evaporation are the dominant heat transfer mechanisms. This conclusion is consistent with the depletion of the energy stored in the superheated liquid layer (perhaps by previously departing bubbles) resulting in lower bubble growth rates.

5.5. Physical and Equivalent Diameter Ratio at Departure

The ratio of physical diameter to equivalent diameter (the Diameter Ratio, DR) at departure could be used as a measure of the contribution of superheated liquid layer to bubble growth. Values of diameter ratio greater than one indicate significant

contributions from the superheated liquid layer, values less than or equal to one indicate significant contributions from microlayer/three phase contact line. DR was calculated for the data presented in this work (pentane) as well as other works in the literature. The results of DR vs. the time it takes for a bubble to depart after nucleating are plotted in Fig. 5.35. The value of the Jakob number for the experiments with constant temperature boundary conditions are also included in Figure 5.35; in this range, the Jakob number does not appear to be the key factor for determining the dominant heat transfer mechanisms. Note that for the case when the Jakob number is 9.6 (Run A), both rapidly and slowly growing bubbles were observed.

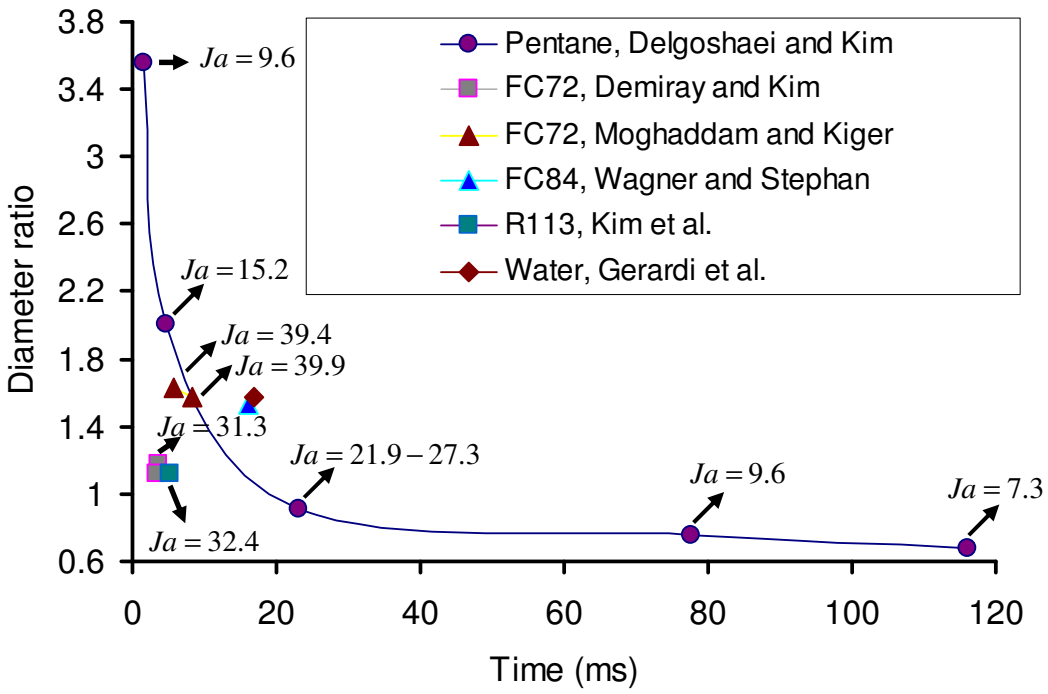

Figure 5.35. Diameter Ratio versus departure time.

Figure 5.35 indicates that the diameter ratio is inversely related (some scatter in the data) to bubble growth time. The proposed hypothesis is that when the bubble grows very rapidly due to a large amount of energy being stored in the superheated liquid layer, the majority of the required heat for bubble growth originates from the superheated liquid layer and not from instantaneous heat from the wall. For bubbles that grow more slowly, however, the diameter ratio is much closer to 1 and can even drop below 1, meaning the bubble growth is limited by the wall heat transfer; the energy stored in the superheated liquid layer has been depleted (perhaps by previously departing bubbles) leaving the wall as the only source of energy. This energy must be transferred through the microlayer or at the contact line.

5.6. Lateral Merger of Two Bubbles

The objective of this study was to investigate the heat transfer behavior related to the lateral merger of the bubbles on the heater.

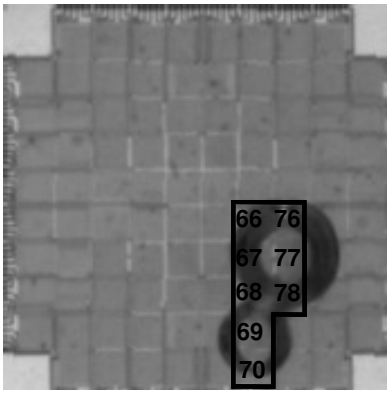

Figure 5.36. Selected region on the heater.

The merger event took place on a subset of the heater array henceforth referred to as the "selected region". The selected region (comprised of 8 heaters) is outlined in Fig. 5.36. The heater temperature for all elements in the array was 52 °C. The test conditions for this experiment are provided in Table 5.6.

Again, in order to initiate boiling the wall temperature was originally set to higher values and then reduced to the desired value. The baseline heat transfer, however, was obtained by setting the heater to the test temperature without initiating boiling by originally setting the heater at higher temperatures. High speed images were also obtained for the case of baseline data to confirm that no bubble was formed on the heater.

Table 5.6. Test conditions for lateral merger experiment.

Pressure (atm)	1.17
T_w (°C)	52
T_{sat} (°C)	40.5
T_{bulk} (°C)	36.1
Superheat (°C)	11.5
Subcooling (°C)	4.4
Air jet	ON

Note: The heater was set to higher temperatures (about 90 °C) to initiate boiling.

5.6.1. Heat Transfer for Individual Heaters

An example of raw heat transfer variation with time for a specific heater (heater 66) is given in Fig. 5.37. Note that the baseline heat transfer indicated in Fig. 5.37 was calculated by averaging the baseline heat transfer at each time step. The heat transfer due to bubble formation and departure (bubble heat transfer) was calculated by subtracting the baseline heat transfer from the raw heat transfer.

The heat transfer variation for heater 66 for a much shorter period of time as well as bubble images at various times are given in Fig. 5.38. It should be noted that with the exception of heater 77, for which baseline data was not available, bubble heat transfer is used for the purpose of investigating the heat transfer trends for various heaters.

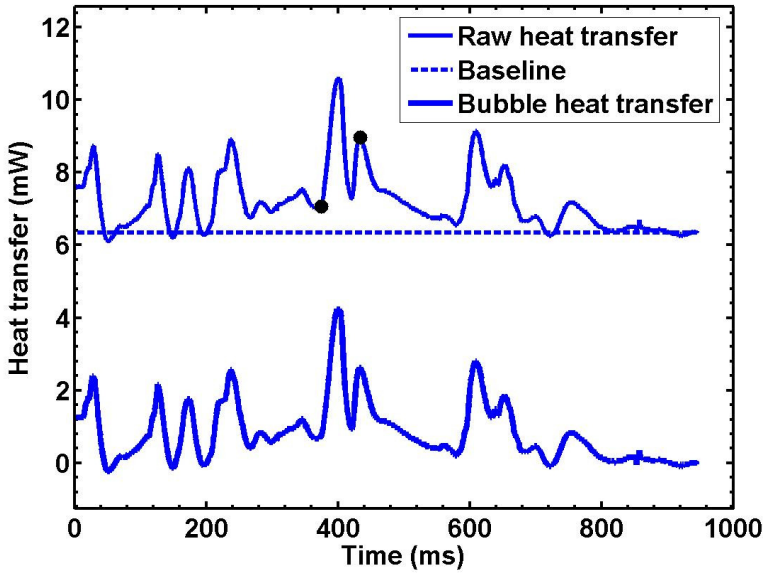

Figure 5.37. Heater 66 heat transfer (raw, baseline, and bubble).

Heat transfer increases from A to C as three-phase contact line recedes while it oscillates on the heater. This increase in heat transfer is likely due to microlayer evaporation and transient conduction from the rewetted area. It should be noted that the area affected by the contact area movement is minimal from A to C. Heat transfer decreases from D to F as lateral merger occurs since the contact area is not located on heater 66 (decrease in the transient conduction). Heat transfer then increases from G to I probably due to microconvection resulting from the bubble departure.

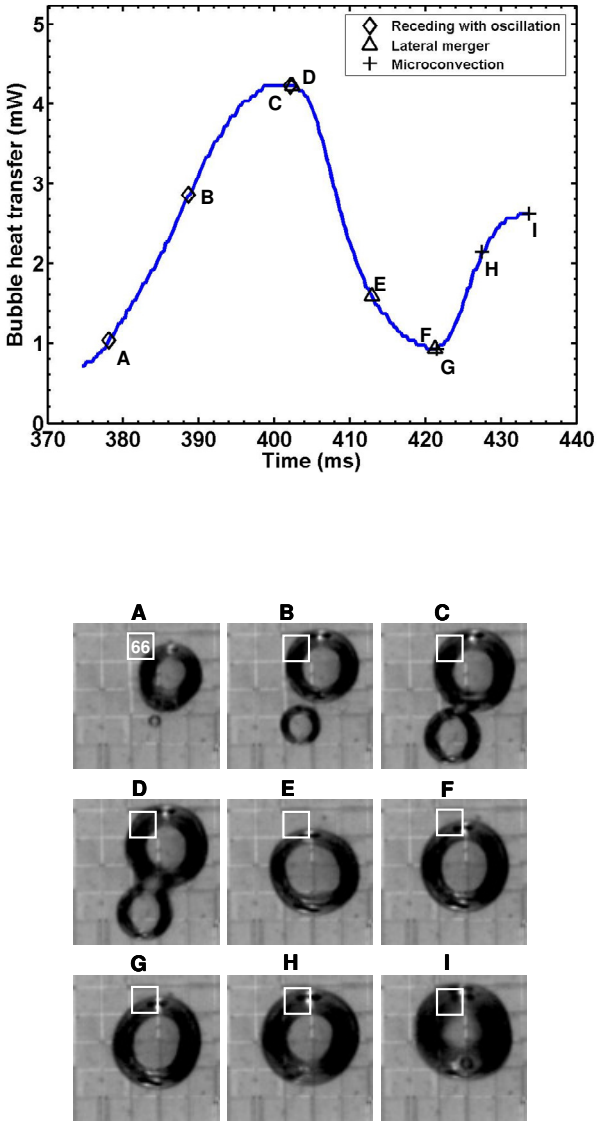

Figure 5.38. Heater 66 raw and bubble heat transfer with bubble images at different times.

The heat transfer variation for heater 67 for the same period of time along with bubble images at various points is given in Fig. 5.39.

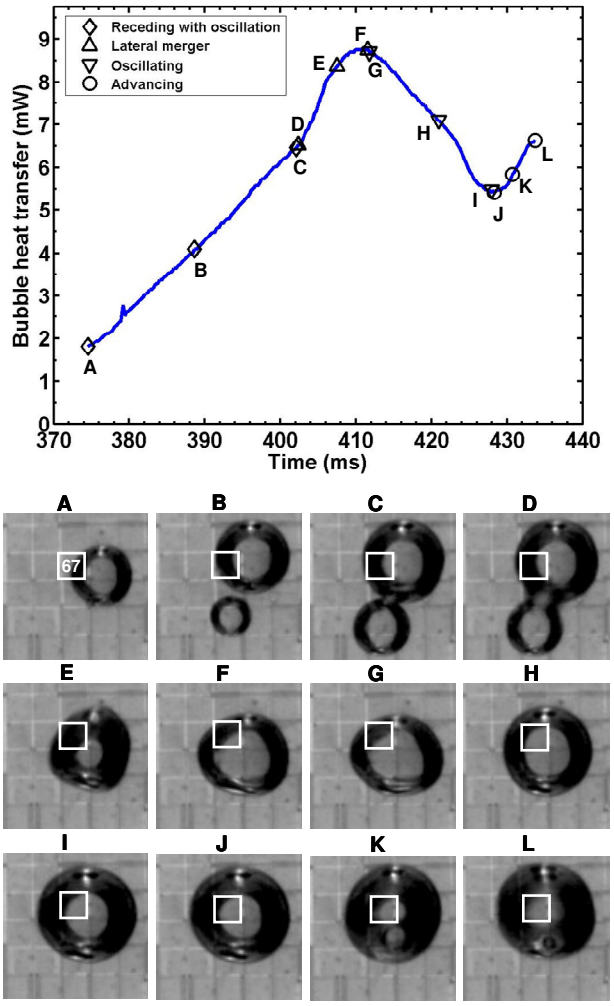

Figure 5.39. Heater 67 bubble heat transfer with bubble images at different times.

Heat transfer increases from A to C as the contact line recedes while it oscillates on the heater. Similar to what was observed on heater 66, this increase is likely due to the microlayer evaporation and transient conduction from the rewetted area. The heat transfer increases from D to F due to the rewetting of the heater as the lateral merger occurs. Note that for this specific heater, the affected area by the merger is minimal and

the heat transfer increase due to merger is also minimal (less than 3 mW). Heat transfer then decreases from G to I as the contact line recedes while it oscillates on the heater as would be expected as the microlayer dries out. Rewetting of the heater from J to L is accompanied by an increase in the heat transfer.

The heat transfer variation for heater 68 during this time along with bubble images at various points is given in Fig. 5.40.

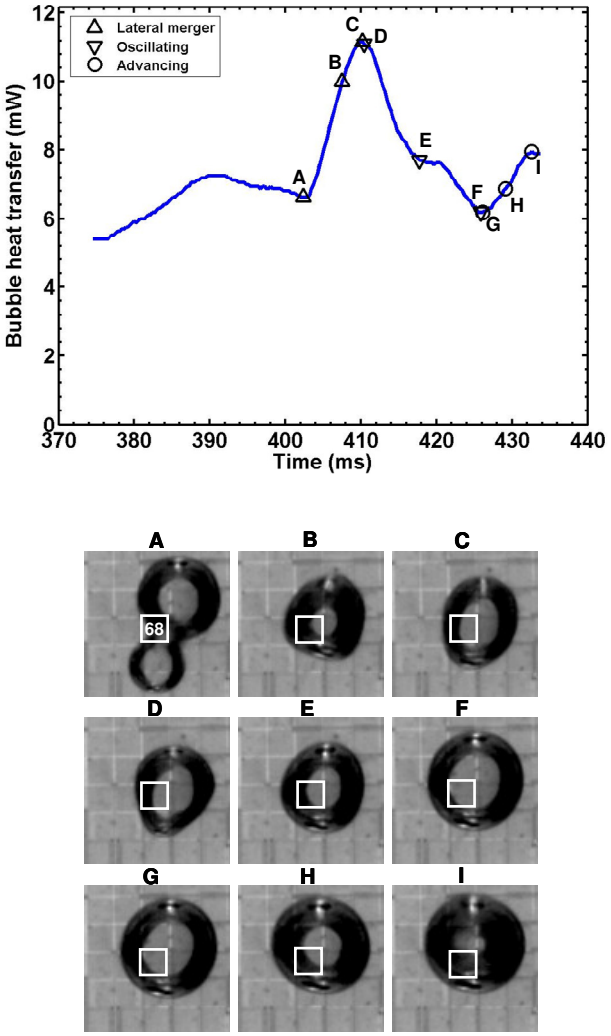

Figure 5.40. Heater 68 bubble heat transfer with bubble images at different times.

Heat transfer increases significantly (about 5 mW) for heater 68 during the lateral merger. This can again be explained by the significant movement of the contact area on the heater. Heat transfer then decreases from D to F as the contact line recedes while it oscillates on the heater, which is consistent with microlayer dryout. Rewetting of the heater occurs from G to I and is accompanied by an increase in heat transfer.

The heat transfer variation for heater 69 along with bubble images at various points is given in Fig. 5.41.

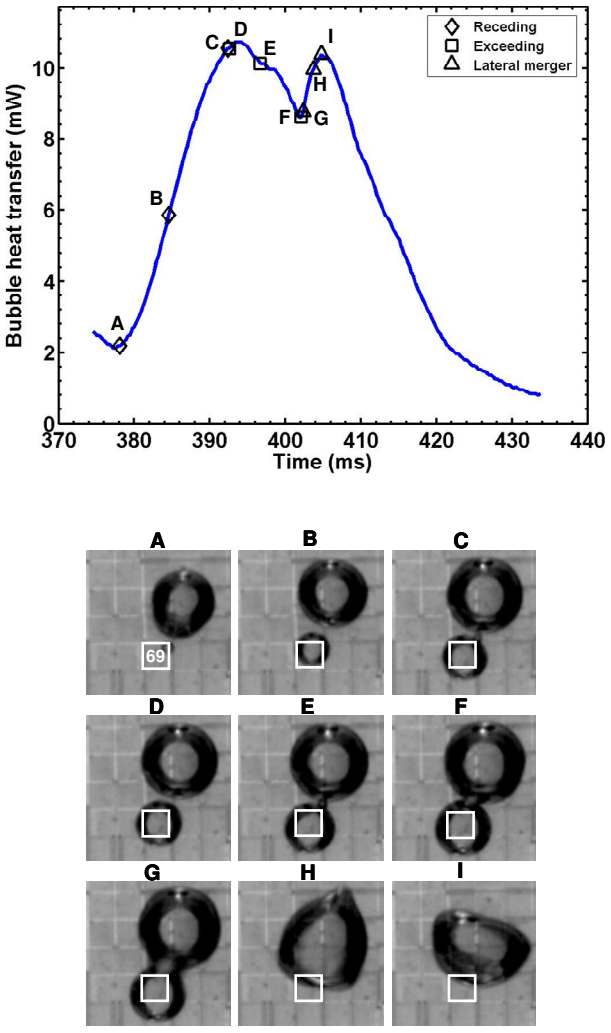

Figure 5.41. Heater 69 bubble heat transfer with bubble images at different times.

Heat transfer increases significantly (about 8 mW) as a new bubble nucleates and grows on heater 69. This increase is probably due to microlayer evaporation and/or contact line heat transfer. Heat transfer then decreases from D to F as the contact line grows beyond heater 69 which is consistent with drying of the microlayer. Lateral merger occurs from G to I accompanied by an increase in the heat transfer (about 2 mW). It should be noted that there is minimal contact area oscillation after the merger for this heater which is probably the reason for the minimal heat transfer increase.

The heat transfer variation for heater 70 along with bubble images at various points is given in Fig. 5.42.

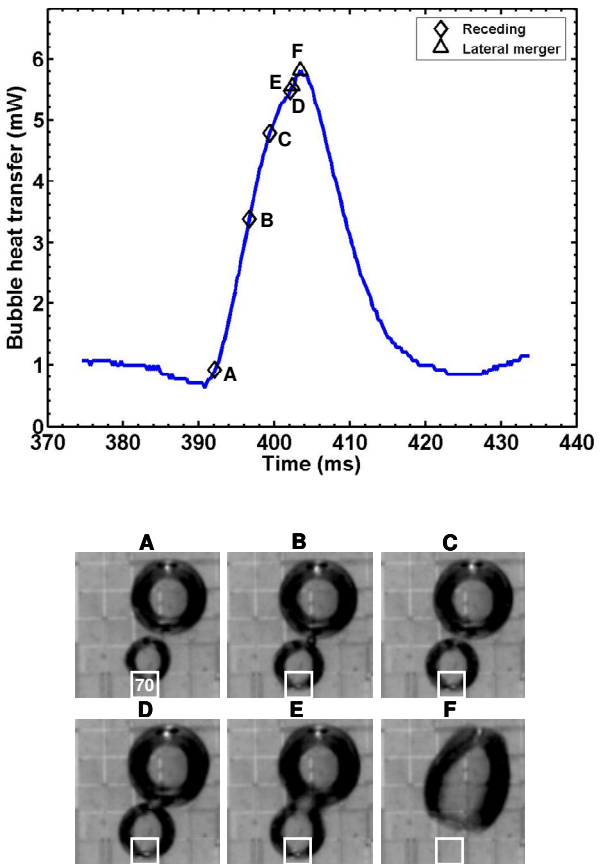

Figure 5.42. Heater 70 bubble heat transfer with bubble images at different times.

The receding of the contact line on the heater (A to C) is again accompanied by a considerable heat transfer increase probably due to the microlayer evaporation and/or contact line heat transfer. Heat transfer increase during the lateral merger (D to F) is minimal as the heater affected area is not significant.

The heat transfer variation for heater 76 along with bubble images at various points is given in Fig. 5.43.

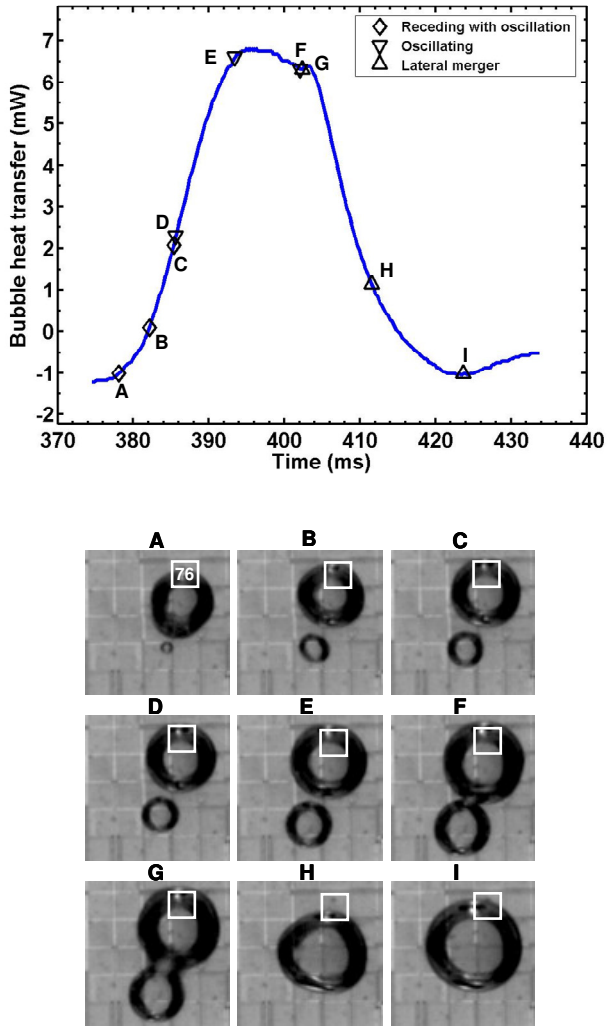

Figure 5.43. Heater 76 bubble heat transfer with bubble images at different times.

Heat transfer increases from A to C as contact line recedes while it oscillates on the heater. This increase is probably due to the microlayer evaporation and transient conduction from the rewetted area. Contact area oscillation continues from D to F and results mostly in the heat transfer increase (microlayer evaporation and transient conduction). Heat transfer actually decreases as the lateral merger occurs since the contact area is not really located on heater 76 (decrease in the transient conduction).

The heat transfer variation for heater 77 along with bubble images at various points is given in Fig. 5.44. Heat transfer increases as the contact line oscillates on the heater from A to C. This increase is probably due to the microlayer evaporation and transient conduction during the rewetting process. Heat transfer decreases from D to F as the contact area exceeds the heater due to drying of the microlayer. Heat transfer increases significantly as lateral merger occurs. This increase is in agreement with the large affected area on the heater. Heat transfer again decreases from K to M as the contact area is oscillating. This decrease is likely due to the drying of the microlayer. Rewetting of the heater occurs from N to P accompanied by an increase in the heat transfer.

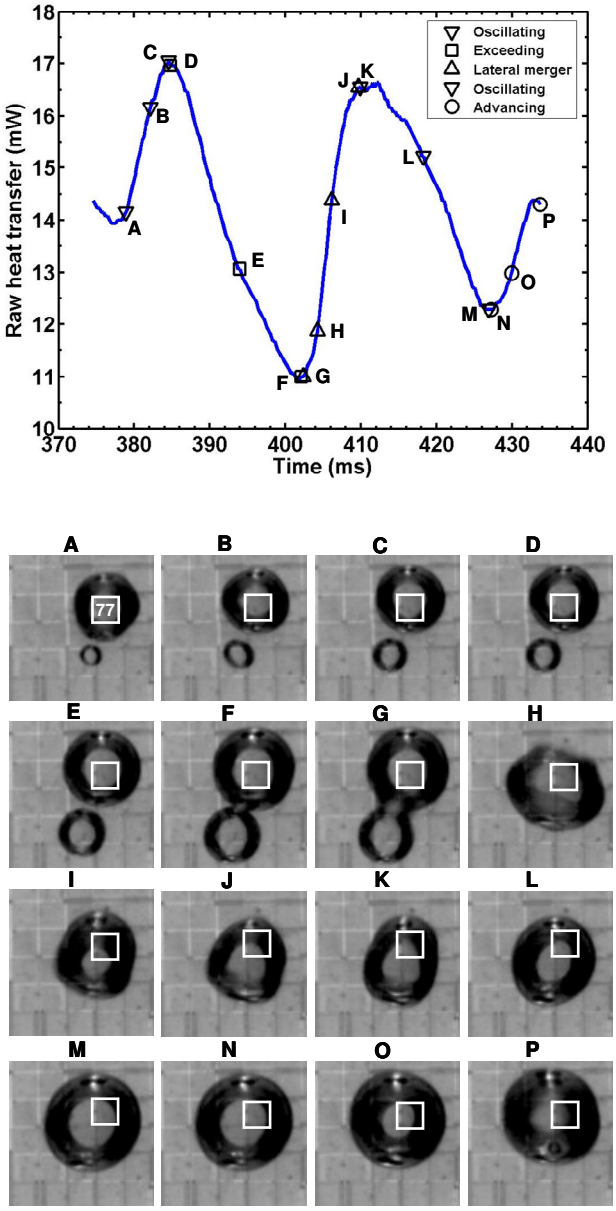

Figure 5.44. Heater 77 raw heat transfer with bubble images at different times.

The heat transfer variation for heater 78 along with bubble images at various points is given in Fig. 5.45. Note that the initial drop in the heat transfer before point A is related to a previously departed bubble (decrease in the heat transfer associated with transient conduction). Heat transfer increase from A to C is probably due to

microconvection. It should be noted that microlayer evaporation is also a possible heat transfer mechanism as the contact line could be slightly on the heater. Heat transfer continues to increase as the lateral merger occurs. The magnitude of increase is in agreement with the large affected area on the heater. Heat transfer mostly decreases from G to J as the contact area is oscillating. This decrease is probably due to the drying of the microlayer. Rewetting of the heater occurs from K to L accompanied by an increase in the heat transfer.

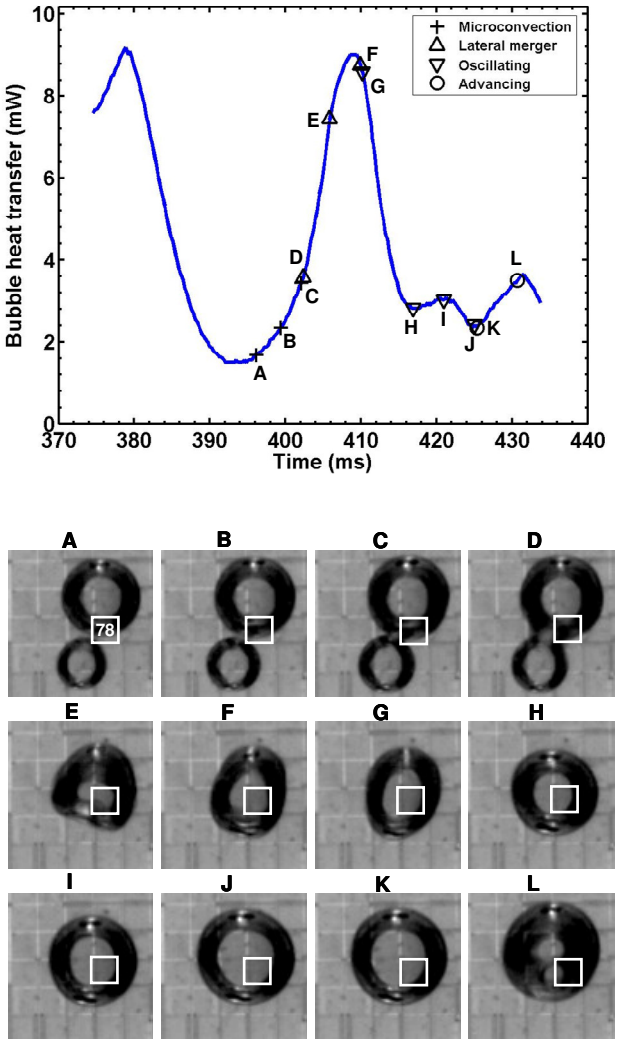

Figure 5.45. Heater 78 bubble heat transfer with bubble images at different times.

5.6.2. Total Heat Transfer from the Selected Region

Total heat transfer for the selected region was obtained by summing the heat transfer from each heater in that region. Total heat transfer variation with time is given in Fig. 5.46. It should be noted that bubble heat transfer could not be calculated since the baseline was not available for heater 77.

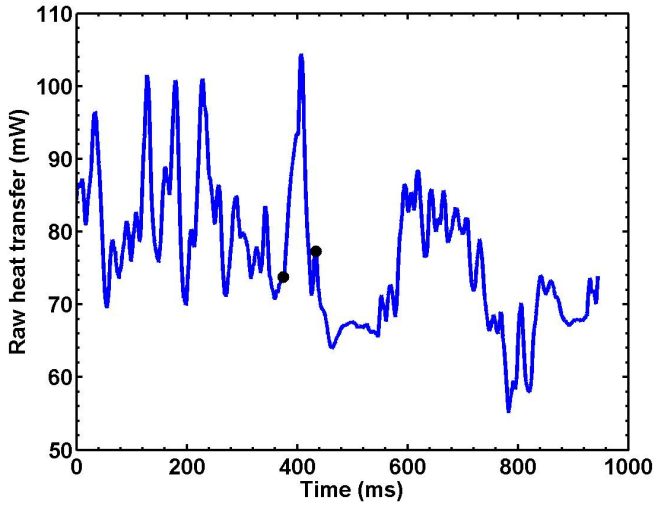

Figure 5.46. Total heat transfer from the selected region.

Total heat transfer variation for a much smaller time period (the same period discussed above for the individual heaters) along with bubble images at various times are given in Fig. 5.47.

Heat transfer variation from the selected region can be divided into four parts. The first part (A-D) is where heat transfer increases gradually. Microlayer evaporation and transient conduction (contact line oscillations) are both present in this period. The second part (D-F) is where the lateral merger occurs between the bubbles and heat transfer increases more rapidly. Transient conduction (rewetting of the heater) and turbulent

mixing are likely responsible for this sudden increase. The decrease in the heat transfer in the third part (F-J) is consistent with the decrease in the transient conduction and drying of the microlayer. Finally, heat transfer again increases (J-L) as the rewetting occurs on the region.

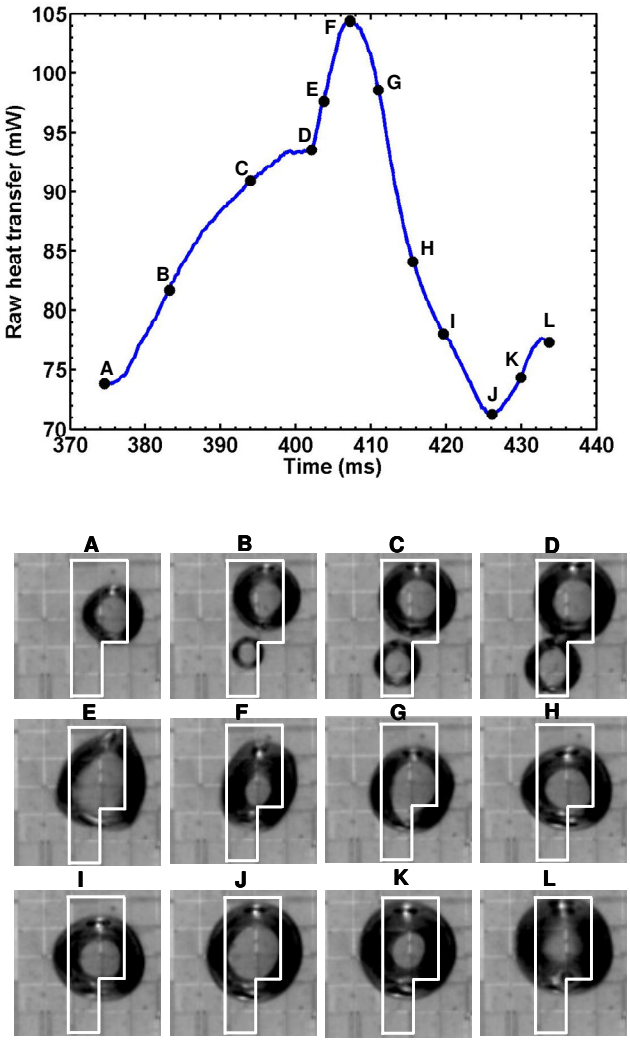

Figure 5.47. Total heat transfer with bubble images at different times.

5.6.3. Conclusions Regarding Lateral Merger of Two Bubbles

Local heat transfer associated with the lateral merger was found to be proportional with the contact area movement resulting from the merger. Transient conduction and turbulent mixing effects were mostly responsible for the observed heat transfer enhancement associated with the lateral merger.

CHAPTER 6: VALIDATION OF POOL BOILING MODELS

The objective of this chapter is to apply some of the available boiling models and compare it against the experimental data. Experimental results for the sequence of bubbles with minimal waiting time (Section 5.2) were compared with the results obtained from the models.

As it will be discussed shortly, the heat transfer mechanisms are highly affected by the contact area movement. An approximate apparent contact line (marked by the solid line in Fig. 6.1) was obtained by applying a linear fit between closely spaced points that follow the general trend of the contact line. The region within the contact line was considered to be the contact area. This procedure was performed for every frame (0.27 ms apart) to record the movement of contact area with time. It should be noted that each "." in Fig. 6.1 represents a pixel in the image.

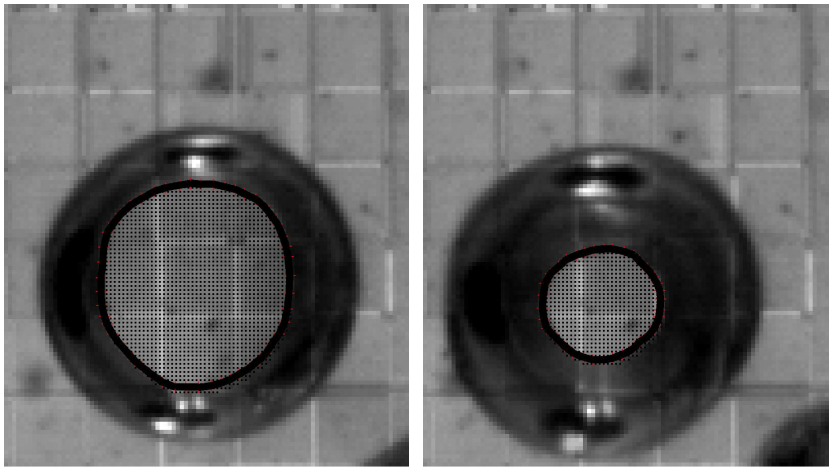

(a) (b)

Figure 6.1. Apparent contact line and contact area for a sample bubble (a) t =458.8 ms (b) t =464.2 ms.

6.1. Microlayer Evaporation Model

The heat transfer due to the evaporation of the microlayer was modeled based on the work of Cooper & Lloyd (1969). They postulated that the initial thickness of the microlayer is given by

$$\delta_0 = C_2\sqrt{\nu t_g} \tag{6.1}$$

where t_g is the time taken for the bubble to grow to a particular location on the heater. Cooper and Lloyd suggested C_2 is a constant of order 0.8. Assuming the thermal capacity of the microlayer is negligible (i.e. $\rho_l c_p \delta\left(\frac{\partial T}{\partial t}\right) << k_l(\frac{\partial T}{\partial z})$ in the microlayer) and the temperature at the liquid vapor interface is assumed to be T_{sat} (Cooper & Lloyd, 1969). The energy balance for the microlayer reduces to

$$-\rho_l h_{lv}\frac{d\delta}{dt} = k_l\frac{T_w - T_{sat}}{\delta} \tag{6.2}$$

Separating variables and performing integration from t_g to an arbitrary time t yields

$$\delta(t) = [\delta_0^2 - \frac{2k_l}{\rho_l h_{lv}}(T_w - T_{sat})(t - t_g)]^{1/2} \tag{6.3}$$

The heat flux at any position covered by the microlayer is given by

$$\dot{q}''_{me} = \frac{k_l (T_w - T_{sat})}{\delta} \tag{6.4}$$

$\dot{q}''_{me}$ was obtained for every pixel assuming microlayer evaporation is active for the entire contact area unless where δ was calculated to be zero from Eq. 6.3. The heat transfer due to microlayer evaporation (based on the above model) for a given heater is given by

$$\dot{q}_{me,h} = \sum_{A_{contact,h}} \dot{q}''_{me,pixel} A_{pixel} \tag{6.5}$$

The uncertainty in position for the pixels at the boundary of the contact area is relatively high, due to limited resolution of the bubble images. However, $\dot{q}_{me,h}$ is not affected by much since the pixels at the boundary are a small fraction of all the pixels being summed in Eq. 6.5.

It should be noted that the value of $\dot{q}_{me,h}$ is a function of C_2 due to the dependence of $\dot{q}''_{me}$ on C_2 through Eq. 6.3 and Eq. 6.1. Further details of obtaining C_2 for different bubble events on different heaters are provided in Section 6.3.

6.2. Transient Conduction Model

Consider the case of a two-dimensional liquid front rewetting a heater that is at constant temperature T_w as shown in Fig. 6.2.

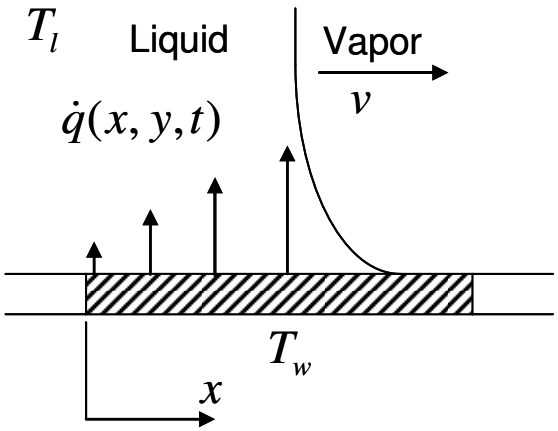

Figure 6.2. Transient conduction model.

A transient conduction model for advancing contact line heat transfer was developed in order to further understand its contribution to the overall heat transfer. Assuming 1-D conduction into the liquid, the heat flux at any position covered by liquid is obtained from the solution for transient conduction into a semi-infinite body:

$$\dot{q}''_{tc} = \frac{k_l (T_w - T_l)}{\sqrt{\pi \alpha_l t}} \tag{6.6}$$

where t is the length of time the liquid has been covering a particular location on the heater. $\dot{q}''_{tc}$ was obtained for every pixel rewetted by the liquid. The heat transfer due to transient conduction (based on the above model) is given by

$$\dot{q}_{tc} = \sum_{A_{rewet}} \dot{q}''_{tc,pixel} A_{pixel} \tag{6.7}$$

The uncertainty in position for the pixels at the boundary of the contact area is relatively high, due to limited resolution of the bubble images. However, $\dot{q}_{tc}$ is not

affected by much since the pixels at the boundary are a small fraction of all the pixels being summed in Eq. 6.7.

It is possible that the liquid rewetting the wall is not from the bulk but from the superheated layer surrounding the bubble. This means T_l in the transient conduction model could be higher than T_{bulk} for the experiment. Further details of obtaining T_l for the model are provided in the following section.

6.3. Implementing Microlayer Evaporation and Transient Conduction Models

A MATLAB code was developed for implementing the microlayer evaporation and transient conduction models introduced above. Details of obtaining the inputs for the models (C_2 and T_l) are provided in this section.

6.3.1. Implementing the Microlayer Evaporation Model

An example of finding the value of C_2 for heater 35 is shown in Fig. 6.3. Starting from the baseline (point A) where the value of bubble heat transfer is zero both for the data and model, C_2 was varied until the heat transfer prediction by the model at the end of receding phase (point C) was sufficiently close to the data. Note that the contribution of the transient conduction model is mostly zero during the receding phase and the model over-predicts the heat transfer for this heater. The value of C_2 was found to be 1.55 which is higher than the suggested value of 0.8 by Cooper and Lloyd. A higher values of C_2 corresponds to a thicker microlayer, which results in a lower microlayer evaporation heat transfer.

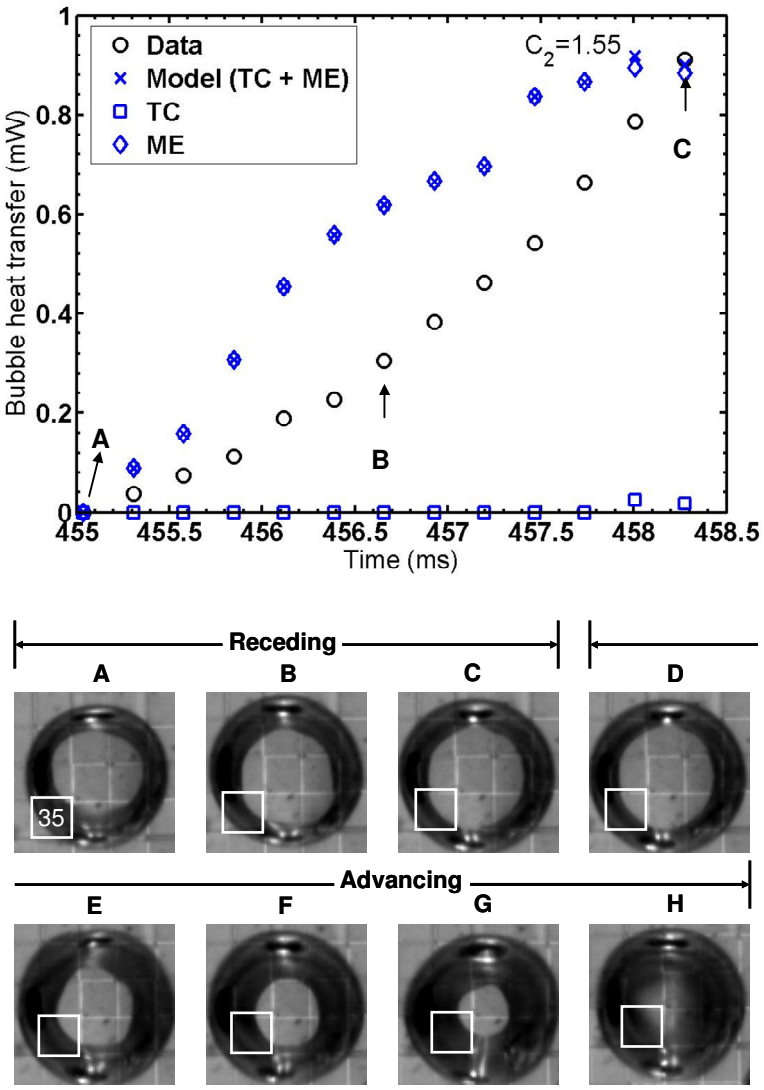

Figure 6.3. Calculation of C_2 for heater 35.

The obtained value of C_2 was then used to predict the contribution of microlayer evaporation for heater 35. The result from the model is compared with the data in Fig. 6.4. The contribution of microlayer evaporation quickly drops after the end of the receding phase and transient conduction / microconvection becomes the dominant heat transfer mechanism.

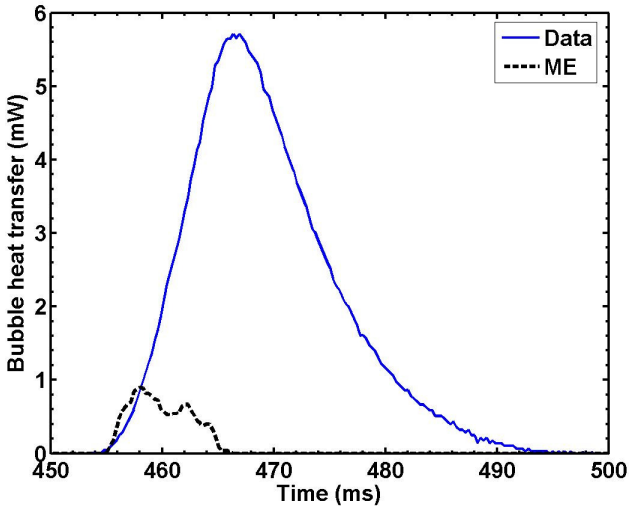

Figure 6.4. Comparison of the data and microlayer evaporation model.

6.3.2. Implementing the Transient Conduction Model

The prediction of the transient conduction model strongly depends on the temperature of the liquid rewetting the heater (T_l). The value of T_l was varied until the amplitude of variation in the heat transfer for the model and data were approximately close to each other. The results for T_l = 31.6 °C (which is the same as T_{bulk} for the experiment), T_l =45 °C, and T_l=49 °C are given in Figures 6.5 through 6.7. Note that the heat transfer predicted by the transient conduction model exceeds the data for T_l=T_{bulk} suggesting that the liquid rewetting the wall is not from the bulk but partially comes from the superheated layer surrounding the bubble. T_l =49 °C was selected as the input for the transient conduction model since it had the highest overall agreement between the data and model.

It can be observed from Figures 6.5 through 6.7 that the agreement between the amplitude of variation in the heat transfer for the model and data could vary considerably

among different bubbles (local maxima in the plot). This suggests that the temperature of the fluid rewetting the heater (T_l) may change for different bubbles. The difference between the data and transient conduction model is due mostly to microconvection.

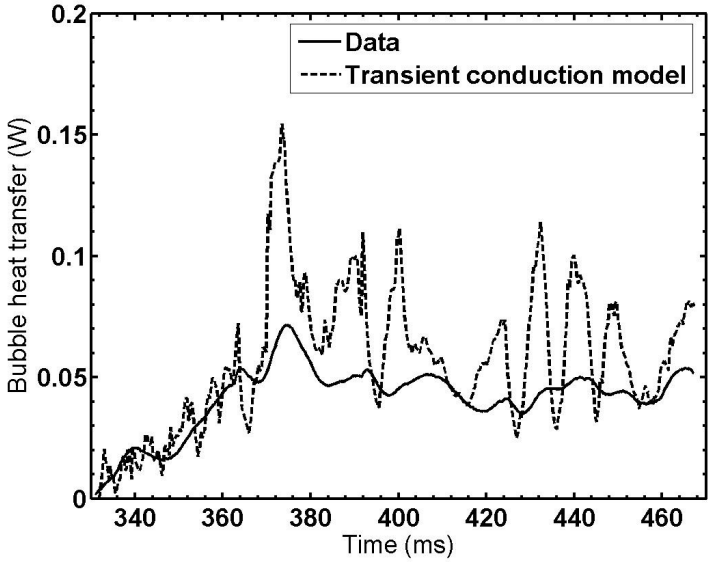

Figure 6.5. Comparison of the transient conduction model and data (T_l=T_{bulk}=31.6 ° C).

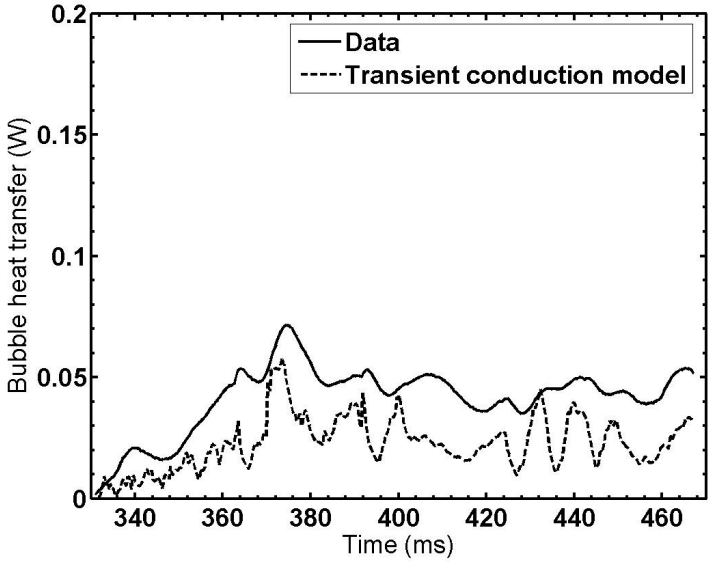

Figure 6.6. Comparison of the transient conduction model and data (T_l=45 ° C).

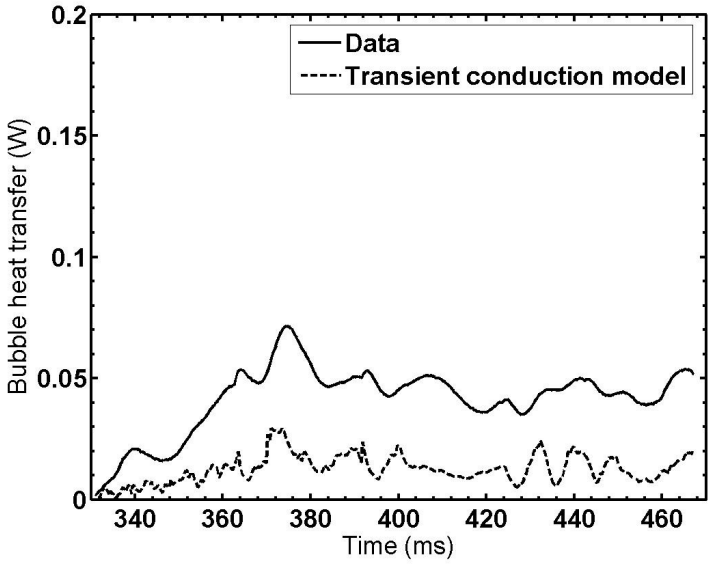

Figure 6.7. Comparison of the transient conduction model and data (T_l=49 ° C).

Chapter 7: Contributions and Conclusions

This thesis was designed to shed light on some of the underlying heat transfer mechanisms in pool boiling. Heat transfer associated with single bubbles and lateral merger were experimentally investigated. Two heat transfer models were implemented in this study: (1) microlayer evaporation model, and (2) transient conduction model. Single bubble experimental results were compared against the prediction from the implemented models. The conclusions, contributions, and suggestions for future work are as follows.

7.1. Conclusions

The bubble growth time was found to be a key parameter in the determination of the dominant heat transfer mechanisms. Single phase heat transfer mechanisms (transient conduction and/or microconvection) were dominant for the bubbles with growth times up to 24 ms. However, two phase heat transfer mechanisms (microlayer and/or contact line evaporation) were dominant for the bubbles with longer growth times (78 and 116 ms).

It was argued that the contribution of different heat transfer mechanisms were dependent on the available energy in the superheated liquid layer. Higher levels of stored energy in this layer resulted in faster bubble growth (shorter bubble growth time); the superheated liquid layer was the main source of energy for these bubbles. The stored energy in the superheated liquid layer was depleted for the bubbles with longer growth times, so these bubbles gained most of their energy from the instantaneous heat from the wall.

The ratio of the bubble's physical diameter to the equivalent diameter (based on the instantaneous wall heat transfer) at the departure was used as a measure of quantifying the contribution of different heat transfer mechanisms. This ratio was higher than one for bubbles with lower growth times (superheated liquid layer being the main source of energy) and less than one for bubbles with higher growth times (instantaneous heat from the wall being the main source of energy). The results from other investigators mostly followed this trend as well.

Finally, the heat transfer variation for the lateral merger of two bubbles was investigated. The total heat transfer from the wall was enhanced as a result of the merger. The enhancement was directly proportional to the contact area movement. It was argued that transient conduction and turbulent mixing effects were mostly responsible for the observed heat transfer enhancement associated with the merger.

7.2. Contributions to the State of the Art

The dominant heat transfer mechanisms in the nucleate boiling regime have been widely argued in the literature. This dissertation is based on the design of multiple experiments that provide a better understanding of the dominant heat transfer mechanisms for different bubble dynamics. The specific contributions of this study to the state of the art are listed below:

- The contribution of different heat transfer mechanisms was found to be dependent on the bubble growth time.
- Single phase heat transfer mechanisms (transient conduction and/or microconvection) were dominant for single bubbles with shorter growth time.

- Two phase heat transfer mechanisms (microlayer evaporation and/ or contact line heat transfer) were dominant for bubbles with longer growth time.
- Heat transfer enhancement due to the lateral merger was found to be clearly related to the contact area movement on the heater.

7.3. Suggestions for Future Work

The main objective of this work was to investigate the dominant heat transfer mechanisms by which heat is removed from a heated wall during nucleate boiling. Some recommendations for future work are as follows.

It would be desirable to have a higher spatial and temporal resolution for the heat transfer measurements. The relative contribution of microlayer and contact line evaporation could be identified by employing a higher spatial resolution for the heat flux measurements. Similarly, the relative contribution of transient conduction and microconvection could be better investigated by improving the spatial resolution of the heat flux measurements.

It is recommended to create an artificial nucleation site on the heater. This would allow the heat flux measurements to be made at critical locations rather than unnecessary ones. The artificial nucleation site also facilitates the formation of single bubbles on the heater.

It would also be desirable to obtain data for different working fluids, preferably with significantly different Jakob numbers. Improving the experimental setup to facilitate the measurements to be made at significantly higher pressures would also be advantageous.

Numerical modeling could be used to better understand the underlying physics of the boiling phenomena. The comparison of the modeling results with the experimental results could shed light on many observations in this study including the effect of bubble growth time on the dominant heat transfer mechanisms.

Finally, it would be advantageous to deduce the velocity field for the case of the lateral merger to better quantify the observed heat transfer enhancement. This can be done by tracking the apparent contact line through the use of the same algorithms used in the transient conduction model.

REFERENCES

Bae, S., Kim, J., Kim, M.H., 1999, "Improved Technique to Measure Time and Space Resolved Heat Transfer under Single Bubbles during Saturated Pool Boiling of FC-72," Experimental Heat Transfer, **12 (3)**, pp. 265-278.

Bonjour, J.M., Clausse M., and Lallemand, M., 2000, "Experimental Study of the Coalescence Phenomenon during Nucleate Pool Boiling," Experimental Thermal and Fluid Science, **20**, pp. 180–187.

Carey, V. P., 2008, "Liquid-Vapor Phase-Change Phenomena," Second Edition, Tylor & Francis Group.

Chen, T. and Chung, J.N., 2002, "Coalescence of bubbles in nucleate boiling on microheaters," International Journal of Heat and Mass Transfer, **45**, pp. 2329–2341.

Chen T. and Chung, J.N., 2003, "Heat-Transfer Effects of Coalescence of Bubbles from Various Site Distributions, Proceedings of the Royal Society A, **459**, pp. 2497-2527.

Cooper, M.G. and Lloyd, A.J.P., 1969, "The Microlayer in Nucleate Boiling," International Journal of Heat and Mass Transfer, **12**, pp. 895-913.

Demiray, F. and Kim, J., 2004, "Microscale Heat Transfer Measurements During Pool Boiling of FC-72: Effect of Subcooling," International Journal of Heat and Mass Transfer, **47**, pp. 3257-3268.

Forster, H.K. and Grief, R., 1959, "Heat Transfer to a Boiling Liquid–Mechanisms and Correlations," Journal of Heat Transfer, **81**, pp. 45.

Fuchs, T., Kern, Jurgen, and Stephan, P., 2006, "A Transient Nucleate Boiling Model Including Microscale Effects and Wall Heat Transfer," Journal of Heat Transfer, **128**, pp. 1257-1265.

Gerardi, C., Buongiorno, J., Hu, L. W., and McKrell, T., 2009, "Measurement of Nucleation Site Density, Bubble Departure Diameter and Frequency in Pool Boiling of Water using High-Speed Infrared and Optical Cameras," Proceedings of 7th ECI International Conference on Boiling Heat Transfer, Florianópolis, Brazil, May 3-7.

Haider, S.I. and Webb, R.L., 1997, "A Transient Micro-Convection Model of Nucleate Pool Boiling," International Journal of Heat and Mass Transfer, **40**, pp. 3675-3688.

Hsu, Y.Y., 1962, "On the Size Range of Active Nucleation Cavities on a Heating Surface," Journal of Heat Transfer, **84**, pp. 207-213.

Judd, R.L. and Hwang, K.S., 1976 "A Comprehensive Model for Nucleate Pool Boiling Heat Transfer Including Microlayer Evaporation", Journal of Heat Transfer, **98**, pp. 623-629.

Kim, J., Oh, B.D., and Kim, M.H., 2006, "Experimental Study of Pool Temperature Effects on Nucleate Pool Boiling," International Journal of Multiphase Flow, **32**, pp. 208-231.

Lee, H.C., Oh, B.D., Bae, S.W., Kim, M.H., Lee, J.Y., and Song, I. S., 2003a, "Partial Nucleate Boiling on the Microscale Heater Maintaining Constant Wall Temperature," Journal of Nuclear Science and Technology, **40 (10)**, p. 768-774.

Lee, H.C., Oh, B.D., Bae, S.W., and Kim, M.H., 2003b, "Single Bubble Growth in Saturated Pool Boiling on a Constant Wall Temperature Surface," International Journal of Multiphase Flow, **29**, pp. 1857-1874.

Mikic, B.B. and Rohsenhow, W.M., 1969, "A New Correlation of Pool Boiling Data Including the Effect of Heating Surface Characteristics," Journal of Heat Transfer, **9**, pp. 245-250.

Moghaddam, S. and Kiger, K., 2008, "Physical Mechanisms of Heat Transfer during Single Bubble Nucleate Boiling of FC-72 under Saturated Conditions – I. Experimental Investigation," International Journal of Heat and Mass Transfer, **52 (5-6)**, pp. 1284-1294.

Mukherjee, A., Dhir, V.K., 2004, "Study of Lateral Merger of Vapor Bubbles during Nucleate Pool Boiling," Journal of Heat Transfer, **126**, pp. 1023-1039.

Myers, J.G., Yerramilli, V.K., Hussey, S.W., Yee, G.F., and Kim, J., 2005, "Time and Space Resolved Wall Temperature and Heat Flux Measurements During Nucleate Boiling with Constant Heat Flux Boundary Conditions," International Journal of Heat and Mass Transfer, **48 (12)**, pp. 2429-2442.

Rohsenow, W.M., 1951, "A Method of Correlating Heat Transfer Data for Surface Boiling of Liquids," Journal of Heat Transfer, **74**, pp. 969–976.

Rosenhow, W.M., 1952, "A Method of Correlating Heat Transfer Data for Surface Boiling of Liquids", Transactions of the ASME, **4**, pp. 969-975.

Rule, T.D., Kim, J., 1999, "Heat Transfer Behavior on Small Horizontal Heaters during Pool Boiling of FC-72," Journal of Heat Transfer, **121 (2)**, pp. 386–393.

Son, G., Dhir, V.K., and Ramanujapu, N.,1999, “Dynamics and Heat Transfer Associated with a Single Bubble during Nucleate Boiling on a Horizontal Surface”, Journal of Heat Transfer, **121**, pp. 623-631.

Son, G., Ramanujapu, N., and Dhir, V.K., 2002, “Numerical Simulation of Bubble Merger Process on a Single Nucleation Site during Pool Nucleate Boiling”, Journal of Heat Transfer, **124**, pp. 51-62.

Tien, C.L., 1962, “A Hydrodynamic Model for Nucleate Pool Boiling”, International Journal of Heat and Mass Transfer, **5**, pp. 553-540.

Wagner, E. and Stephan, P., 2009, “High Resolution Measurements at Nucleate Boiling of Pure FC-84 and FC- 3284 and its Binary Mixtures,” Journal of Heat Transfer, in press.

Williamson, C.R. and M.S. El-Genk, 1991, “High-Speed Photographic Analysis of Saturated Nucleate Pool Boiling at Low Heat Flux,” ASME Winter Meeting, Atlanta, GA, December 2-5.

Yaddanapuddi, N. and Kim, J., 2001, “Single Bubble Heat Transfer in Saturated Pool Boiling of FC-72,” Multiphase Science and Technology, **12 (3-4)**, pp. 47-63.